Technical University Delft

ME55010: Literature Survey & ME55035: Thesis

Power-to-gas efficiency of a hydrogen back-up system governed by interruptible sources and services

TU Delft supervisor:
Prof. dr. ir. S.A. Klein

Author:
Nick Kimman, 4507371

TU Delft assisting supervisor:
Prof. dr. ir. P.M. Herder

June 4, 2020

Acknowledgements

I would sincerely like to thank Prof. dr. ir. S. Klein en Prof. dr. ir. P.M. Herder for supervising my master thesis. They took time for the many meetings and gave excellent feedback on my work. They learned me new ways of approaching complex problems and documenting these in a concrete manner. Furthermore, I would like to thank my friends, parents and brothers for the support they gave me during the graduation period. They always showed interest in my work which was a great motivation. Lastly, I would like to give my special thanks to Nathalie for standing by me and believing in me. She was able to let me see things differently and to provide perspective which was of great help.

Abstract

Fossil fuel based energy systems are the main contributor to global warming. As new regulations come into place, a transition towards a more sustainable energy system must be realised. Hydrogen is regarded as the key enabler of such systems for it can balance the power grid by storing and utilizing the energy coming from intermittent renewable energy sources. In addition, hydrogen integration into multi-generation energy systems can offer many other valuable services, like feedstock, heating and transportation fuel resulting in minimal losses.

The heart of these hydrogen-based energy systems (HESs) is the hydrogen back-up system (HBS) which is responsible for the production, transport and storage of hydrogen. The literature survey defined that the large-scale, geographically spread HBS for this study will consist of a PEM electrolyzer (PEME), pipeline transport and salt cavern storage. This configuration results in scalable and highly pure hydrogen production with a quick response to the intermittent nature of the sources. Moreover, the hydrogen can be stored in sufficiently large quantities with an almost instantaneous delivery response to the demand of the services at distant locations. This study investigated how the power-to-gas efficiency of a HBS is governed by various sources and services. This efficiency incorporates all losses between the source output and the service input.

Two services are defined for the HES; Service 1: Constant hydrogen supply for the chemical industry. The chemical industry is a sector with a rapidly growing hydrogen demand as hydrogen is feedstock for many valuable chemical products. Service 2: Interruptible hydrogen supply as a fuel for power back-up. The power grid is more likely to get congested due to the rapidly increasing interruptible renewable power supply. A power back-up provide the means to balance the supply and demand of power. Both services can either use a wind farm or the power grid as the source where the source power output is determined by the wind speed or the spot price for power, respectively. So, a total of four different cases are defined.

A fully transient mathematical model of the system, built in Matlab® Simulink, was made for this study. This model uses a rectifier and a PEME to convert the source power into hydrogen. A transport system, consisting of a pressure control station (PCS) and a 50 kilometre transmission pipeline, delivers the hydrogen to the salt cavern. Here, the hydrogen is injected into a 1000 metre deep cavern by a PCS and an injection pipeline with nozzle. After a discharge pipeline, a third PCS is installed to adapt the hydrogen temperature and pressure for another 50 kilometre long transmission pipeline. A final PCS adapts the flow properties to the desired service values. All components are able to fully capture the intermittent nature of the cases.

Historical data of the spot prices for power and wind speeds of 2017 are used for the sources and services. The resulting production and consumption profiles for 2017 were used to size the HBS for each case, ensuring full use of the cavern capacity without over- or underproduction.

Simulations of the defined cases, using the same historical data, showed that the caverns only completed one full charge-discharge cycle during 2017, showing that all cases demand seasonal storage. The power-to-gas efficiency of both the grid-powered cases is 58%. The wind-powered cases show efficiencies of 44% and 41% for the chemical industry and the power back-up cases, respectively. The main conclusions as to why these difference are present and how the efficiencies are governed by the sources and services are listed below.

- Wind-powered HBSs lead to roughly 24 - 28% more power losses due to a mismatch between the wind farm power output and the PEME operational power input limits. The most significant losses occur during low wind speeds when the wind farm output is between zero and the minimum PEME operating power. This loss is the main contributor to the differences in the power-to-gas efficiencies for all cases.
- The PEME efficiencies are in the range of 67.5 - 70.1%, making it the largest contributor to the total HBS losses.
- The transport and storage systems for all cases have an efficiency of roughly 95.0 - 95.5%.
- The efficiency of wind-powered PEMEs is 2.3 - 2.6 percentage points higher compared to grid-powered PEMEs as these have less voltage losses due to operation below the rated power.
- The service has no significant effect on the efficiency as the service pressure for all cases is for large part of the year lower than the transport and storage pressure, resulting in negligible power requirements for the transport system.

Furthermore, many cold start-up cycles of the PEME, inherent to intermittent sources, only lead to an insignificant yearly efficiency drop of around 0.1% as more losses occur at low operating temperatures. The PCS directly after the PEME always operates as a compressor and consumes the most power of all the PCSs due to the relatively high pressure ratio (PR) throughout the year. Therefore, this PCS is mainly responsible for the transport and storage efficiency. The case where the source and service are both governed by the spot price simulated a non-renewable power back-up system. The results revealed that this system can be feasible when solely considering the buy and sell price of power. However, this is at the expense of the production and consumption capacity factors, which are only 8% and 4.6%, respectively. Furthermore, only a small profit margin of about 6% was realised. The wind-powered HBS for power back-up simulated a renewable system which delivers a constant 100 MW base load. Around 63% of the base load is directly supplied by the wind farm. The rest is supplied via the indirect route To meet demand at all times, the wind farm and the PEME rated power must be more than 14 and 9 times the base load, respectively, together with a storage capacity of almost 800,000 m^3.

This study concluded that the power-to-gas efficiency of a wind-powered HBS is 14-17 percentage points lower compared to a grid-powered HBS due to the operational limits of a PEME despite the fact that the PEME efficiency itself is around 2.5 percentage points higher when using wind as the power source. In addition, the transport and storage system only accounts for 2-3% of the HBS power consumption of the HBS and the service does not have an influence at all.

Recommendations are to model the PEME as multiple units in order to minimize the PEME power limit losses. Sensitivity analysis pointed out that using different operating parameters could improve the overall system efficiency. Moreover, all operational and investment costs should be taken into account for determining the HES feasibility. Especially, investment costs greatly impact the hydrogen cost price. Furthermore, a combination of multiple renewable energy sources together with battery storage should be investigated. This can potentially increase the PEME capacity factor thus lowering the necessary installed capacity.

This study defined sizes and operational conditions of HESs for several real-world cases based on historical data. It identified the bottlenecks of HESs and gives possible improvements. Research like this can boost the transition towards a more sustainable energy system due to growing confidence. This may pave the way for large investments in HESs from big corporations situated in the fossil-based energy sector.

e

Nomenclature

3S	Source, system, service
AC	After cavern transport / Alternating current
AE	Alkaline electrolyzer
AFC	Alkaline fuel cell
APX	Amsterdam Power Exchange
BC	Before cavern transport
BoP	Balance of Plant
CCGT	Combined cycle gas turbine
CFL	Courant-Friedrichs-Lewy condition
CF	Capacity factor
Capex	Capital expenditure
WT	Chemical industry
DC	Direct current
DP	Discharge pipeline
GD	Power grid
GHG	Greenhouse gas
H_2O	Water
H_2	Hydrogen
HBS	Hydrogen back-up system
HER	Hydrogen evolution reaction
HES	Hydrogen-based energy system
HRES	Hydrogen-based renewable energy system
IP	Injection pipeline
MEA	Membrane electrode assembly

MPPT Maximum power point tracking

NTP Normal Temperature (293.15 K) and Pressure (1 atm)

O_2 Oxygen

OCV Open-circuit voltage

OER Oxygen evolution reaction

Opex Operational expenditure

PCS Pressure control station

PEME Proton exchange membrane electrolyzer

PV Photovoltaic

PWR Wind farm

RC Reference case

SATP Standard ambient temperature (298.15 K) and Pressure (1 atm)

SOE Solid oxide electrolyzer

TP Transmission pipeline

WT Power grid

WECS Wind energy conversion system

e^- Electron

A Area [m^2]

C_{th} Thermal heat capacity [$J{\cdot}K^{-1}$]

C_{tur} Maximum power coefficient of the turbine [-]

D Diameter [m]

ΔG°_R Standard Gibbs free energy change of reaction [$kJ{\cdot}mol^{-1}$]

ΔG°_f Standard Gibbs free energy change of formation [$kJ{\cdot}mol^{-1}$]

ΔH°_f Standard enthalpy change of formation [$kJ{\cdot}mol^{-1}$]

ΔS°_R Standard entropy change of reaction [$kJ{\cdot}(K{\cdot}mol)^{-1}$]

ΔS°_f Standard entropy change of formation [$kJ{\cdot}(K{\cdot}mol)^{-1}$]

E Energy [J]

E_{exc} Activation energy required for the electron transport in the anode electrode [$J{\cdot}mol^{-1}$]

E_{pro} Activation energy required for the proton transport in the membrane [$J{\cdot}mol^{-1}$]

Ex Exergy [J]

$\dot{E}x$	Exergy rate [W]
F	Faraday's constant [96485.332 C·mol^{-1}]
F_s	Safety factor
H	Head / Height [m]
I	Electrical current [A]
K	Pipe flow coefficient [m^{-2}s^{-1}]
L	Length [m]
$\dot{m}$	Mass flow [kg·s^{-1}]
N	Number/Amount [-]
P	Power [W]
P_mem	Membrane permeability [-]
$\dot{Q}$	Heat flow [W]
$\bar{R}$	Specific gas constant [J·(kg·K)$^{-1}$]
Re	Reynolds number [-]
R_mem	Membrane protonic resistance [Ω·cm^2]
R_th	Thermal resistance [K·W^{-1}]
R_u	Universal gas constant [8.3145 kJ·(kmol·K)$^{-1}$]
T	Temperature [K]
$\bar{T}$	Average temperature [K]
ΔT_p	Pinch temperature [K]
UA	Overall heat transfer coefficient [kW·K^{-1}]
U	Voltage [V] / Internal energy [J]
V	Volume [m^3]
$\dot{W}$	Work rate [W]
Y	Flow parameter [-]
Z	Compresibility factor [-]
c	Speed of sound [m·s^{-1}]
c_p	Specific heat capacity [J·kgK^{-1}]
$\bar{c}_p$	Specific average heat capacity [J·kgK^{-1}]
$\dot{ex}$	Specific exergy [J·kg^{-1}]

f	Friction factor [-]
g	Gravitational constant [9.81 $\mathrm{m{\cdot}s^{-2}}$]
h	Specific enthalpy [$\mathrm{J{\cdot}kg^{-1}}$]
h_c	Heat transfer coefficient [$\mathrm{W{\cdot}(m^2K)^{-1}}$]
i_0	Electrode exchange current density [$\mathrm{A{\cdot}cm^{-2}}$]
i	Current density [$\mathrm{A{\cdot}cm^{-2}}$]
k	Thermal conductivity coefficient [$\mathrm{W{\cdot}(m{\cdot}K)^{-1}}$]
m	Mass [kg]
$\dot{n}$	Molar flow rate [$\mathrm{kmol{\cdot}s^{-1}}$]
p	Pressure [Pa]
ρ	Density [$\mathrm{kg{\cdot}m^{-3}}$]
r	Radius [m]
$r_{1,2}$	Empirical parameter related to ohmic resistance of electrolyte [$\mathrm{\Omega{\cdot}m^{-2}}$],[$\mathrm{\Omega{\cdot}(Km^2)^{-1}}$]
s	Specific entropy [$\mathrm{J{\cdot}(kgK)^{-1}}$]
t	Time [s]
u	Specific internal energy [$\mathrm{J{\cdot}kg^{-1}}$]
v	Velocity [$\mathrm{m{\cdot}s^{-1}}$]
x	Distance [m]
y	Molar fraction [-]
z	Number of electrons involved [-]
α	charge transfer coefficient [-]
δ_mem	Membrane thickness [cm]
ϵ	Pipe roughness [m]
η	Efficiency [-]
η_F	Faraday efficiency [-]
γ	Heat capacity ratio [-]
μ	Dynamic viscosity [Pa$\cdot$ s]
σ_mem	Membrane protonic conductivity [$\mathrm{S{\cdot}cm^{-1}}$] = [$\mathrm{(\Omega cm)^{-1}}$]
θ	Angle [°]
υ	Specific volume [$\mathrm{m^3{\cdot}kg^{-1}}$]

List of Subscripts

I Section between grid point n and n+1.

0 Initial.

act activation.

AGS anode gas separator.

amb Ambient.

an anode.

back back flow.

BoP balance of plant.

c cell.

cat cathode.

cav cavern.

CGS cathode gas separator.

ch channel.

ch-ind chemical industry.

chem chemical.

ci cut-in.

co cut-out.

comp compressor.

conc concentration.

cond Conduction.

cons consumption.

conv Convection.

cool Cooling.

ct condensate trap.

cw Cooling water.

d destruction.

e energy.

el electrical.

exp Turbo-expander.

ext exterior.

F Faraday.

f flow.

gb gearbox.

gen generator / generation.

hex Heat exchanger.

hydro hydraulic.

i instant.

in Inlet.

int interior.

is isentropic.

kin kinetic.

LHV lower heating value.

loss Losses.

m maximum.

mech mechanical.

mem membrane.

n node.

ocv open-circuit voltage.

ohm ohmic.

out Outlet.

pot potential.

prod production.

refrig refrigerant.

rev Reversible.

SATP Standard ambient temperature (298.15 K) and Pressure (1 atm).

shell salt cavern shell.

st Stack.

th thermal.

th-n thermal-neutral.

tot total.

tur turbine.

w water.

WECS wind energy conversion system.

Contents

Part I

Chapter 1

Introduction

As worldwide populations grow and more people have access to energy driven technologies, the global energy demand is rising rapidly, shown in Fig. 1.1[1]. Currently, the lion's share of this energy originates from fossil fuels which are huge contributors to the total amount of greenhouse gasses (GHGs) emitted into the atmosphere, causing global warming. In addition, the supplies are geographically restricted and limited, which may lead to a mismatch between supply and demand (Dincer & Acar, 2017). Therefore, worldwide efforts are done on investments in renewable energy sources (Valverde-Isorna et al., 2016).

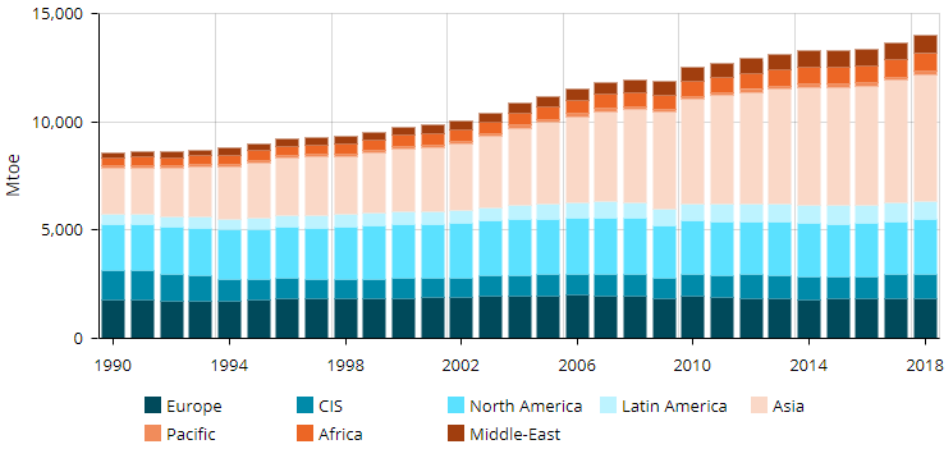

Figure 1.1: Total energy consumption per continent.

Renewable energy sources like wind, solar and hydropower slowly find their way into the energy market (Acar & Dincer, 2019). The main disadvantage is that these are intermittent energy sources depending on the weather conditions. In case of overproduction, energy is lost because the electrical grid provides no storage capacity. Contrary, in case of underproduction, the energy sources fail to meet energy demands. During these periods, fossil fuel based power plants are often needed to compensate for these energy shortages (Carmo & Stolten, 2019).

Intermediate energy storage provides a solution to this inevitable supply and demand mismatch. Some common large-scale energy storage technologies include batteries, compressed air storage and hydropower (Valverde-Isorna et al., 2016). However, hydrogen energy storage is gaining significant

[1] `https://yearbook.enerdata.net/total-energy/world-consumption-statistics.html`

traction by being a promising candidate to solve the energy crisis as it is able to absorb renewable energy and release it at a later instant, making it an energy carrier (Fang & Liang, 2019; Nicoletti et al., 2015). This storage type has the potential to integrate into the existing energy infrastructure as it is accessible, reliable, clean and affordable to all sectors and religions and it is highly resilient. Moreover, integration into multi-purpose systems can offer many valuable products with minimal losses. The transport sector will become cleaner when fuel cells and hydrogen-fueled internal combustion engines are used. Hydrogen could be a feasible replacement for fossil fuels in power plants and a key ingredient for full-scale implementation of sustainable energy into the energy market (Kalinci et al., 2015; Singh et al., 2015). It can bring cleaner energy to industry, residential applications and buildings where it can be used for cooling, heating, drying, feedstock and power (Acar & Dincer, 2019), resulting in a circular economy. Figure 1.2 illustrates a road map up until 2050 which clearly depicts the rapid increase in hydrogen demand for almost all sectors in the ambitious case.

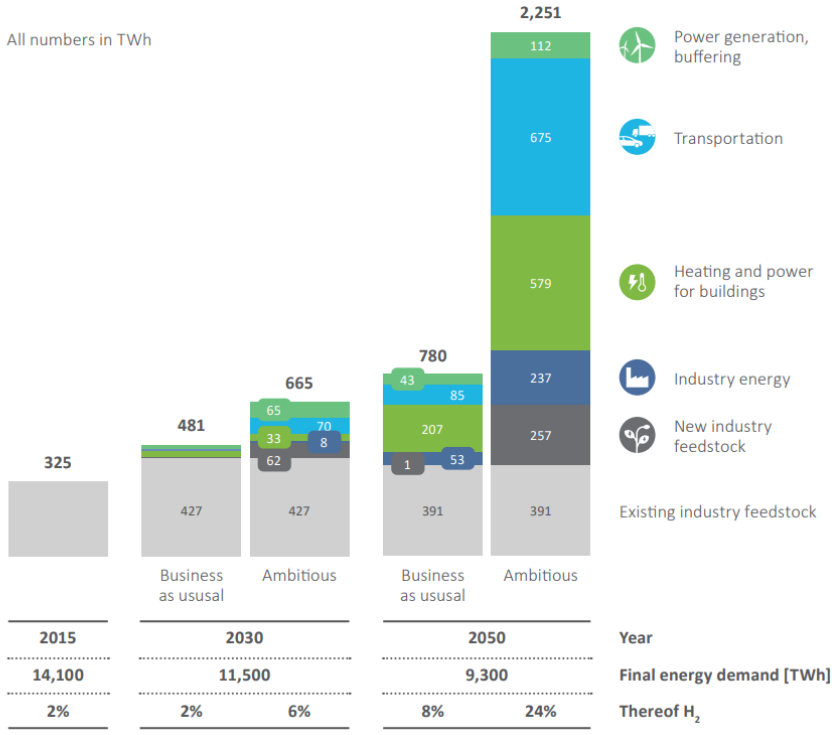

Figure 1.2: Hydrogen road map for Europe (van Wijk & Chatzimarkakis, 2020).

Hydrogen (H) is the lightest element in the periodic table, the most abundant element in the universe and it has the highest energy content of all the known elements (Abe et al., 2019). At NTP, it is an odorless, colourless, tasteless, non-toxic, non-corrosive and non-metallic diatomic gas which is essentially not dangerous (Ripepi, 2018). It is not a naturally occurring molecule and must therefore be produced using natural occurring components like fossil fuels, biomass or water and energy. One kilogram of hydrogen contains about two-and-a-half times the energy of natural gas. However, the mass per volume of hydrogen is significantly lower than any of the other conventional fuels. Methane gas, for example, is almost eight times as dense as hydrogen gas at NTP. Therefore, in order to store the same amount of energy, the storage capacity for hydrogen must be almost three-and-a-half times larger. So, for practical purposes, it must either be compressed or liquefied which both consume additional energy. A brief comparison between hydrogen and more conventional energy carriers like methane and gasoline can be found in Apx. B.

1.1 Hydrogen-based renewable energy system (HRES)

A hydrogen-based renewable energy system (HRES) makes use of a hydrogen back-up system (HBS) which is driven by an intermittent renewable energy source like wind or solar power. The output of the HBS is governed by a service system like hydrogen consumption in a power plant or hydrogen delivery to the chemical industry. The supply and demand is balanced using this HBS which consists of hydrogen production, transport and storage systems. A hydrogen-based energy system (HES), on the other hand, can also make use of a non-renewable source, like the power grid.

1.1.1 HRES studies

In the following section, recent studies which partly align with this study are briefly described and summarized in Tab 1.1. Genc et al. (2012) build a techno-economical model of a wind powered hydrogen energy system. Ishaq et al. (2018) analyzed a wind turbine energy system integrated with a PEME and a hydrogen fuel cell providing electricity and heat for a small-scale community. Olateju et al. (2016) proposed a techno-economic model of a 563 MW hydrogen energy system with hydrogen storage powered by wind turbines using real-time wind data. Furthermore, dynamic prices from a liberalized energy market are incorporated. The aim is to ascertain the optimal electrolyzer size, number of electrolyzers and battery storage capacity which results in the lowest hydrogen production cost. Witkowski et al. (2017) analyzed hydrogen compression and transportation via pipelines for different mass flows, pipe diameters and ambient temperatures.

Table 1.1: Complexity of HRES models found in reviewed literature.

Reference	Source	Production	Storage	Transport	Service	Transient behavior
(Genç et al., 2012)	Wind	PEME (0.040 MW)	Compr. tank	No	Power	Unknown
(Ishaq et al., 2018)	Wind	PEME	Comp. tank	No	Power, Heat	No
(Olateju et al., 2016)	Wind	AE (3.5 MW)	Battery (360 MWh)	Yes	Feedstock	No
(Witkowski et al., 2017)	No	No	No	Yes	No	Transport
(Özgirgin et al., 2015)	Solar	PEME (0.0047 MW)	Compr. tank, Battery	No	Power, Heat	No
(Jafari et al., 2019)	Solar	PEME (0.009 MW)	Compr. tank, Battery	No	Power, Heat	Production, storage
(Devrim & Bilir, 2016)	Wind, solar	PEME (0.0034 MW)	Compr. tank	No	Power	No
(Ali et al., 2016)	Wind, solar	AE (0.030 MW)	Compr. tank	No	Feedstock	Production, storage
(Papadopoulos et al., 2018)	Wind, solar	PEME (1.0 MW)	Battery	Yes	Feedstock	No
(Ripepi, 2018)	No	PEME	Salt cavern	No	Feedstock, Power	Storage
This study	Yes	Yes	Yes	Yes	Yes	Production, storage and transport

Özgirgin (2015) studied a PV-fuel cell hybrid system for household micro co-generation applications. Jafari et al. (2019) presented a thermodynamic analysis of a solar-based hydrogen energy system for a standalone operation. The energy source is determined by real climate data and the demand is based on a residential area. An overall energy efficiency, not taking source losses into account, of the system was found to be 41.8%. Devrim & Bilir (2016) investigated a wind-solar hybrid energy system used for an average house. Ali et al. (2016) developed a thermally compensated electrolyzer model driven by renewable energy sources. The model is thoroughly validated by real world experimental data and has proven to be of use in detecting operational errors of hydrogen storage systems. Papadopoulos et al. (2018) studied four scenarios, varying in configuration and size of the energy sources. The emphasis of the work is laid on the capacity factor of the electrolyzer which uses renewable energy coming directly from the sun or wind or indirectly from the battery. Ripepi (2018) studied an ideal hydrogen storage system with the focus on the injection, static storage and the withdrawal process. Furthermore, a scenario where the withdrawn hydrogen gas from the rock lined salt cavern is expanded in a turbo-expander is studied. None of the studies incorporates all components of a HRES including the transient behaviour, making this study relevant in the field of research.

1.2 Assignment

In this section, the objective and method of the thesis will be elaborated.

1.2.1 Problem statement

Hydrogen-based renewable energy systems (HRESs) are able to provide all the same services a fossil-based system can, while using inexhaustible renewable energy sources making it nearly pollution-free. Such systems make use of a hydrogen back-up system (HBS) which is responsible for matching the hydrogen supply and demand. The HBS consists of a hydrogen production, transport and storage system and is driven by a source and a service. The literature survey revealed that none of the studied literature developed and analyzed a fully transient mathematical model incorporating all components of a HBS using intermittent sources and services. Incomplete models may give an incorrect estimate of system efficiencies, sizes and performance.

1.2.2 Research questions

The research question gives the fundamental core of the project.

⇒ How do the sources and services influence the power-to-gas efficiency of a large-scale hydrogen back-up system consisting of hydrogen production, transport and storage?

Several sub-questions are formulated which will contribute to the main research question:

- Which hydrogen back-up system configuration is best suited for a large-scale hydrogen-based energy system?
- In what way do the source and service influence the individual component sizes of the hydrogen back-up system?
- How do the operating conditions influence the efficiency of the individual components of the hydrogen back-up system?

1.2.3 Objective

The objective of this study is to estimate the power-to-gas efficiency of a HBS using various sources and services. Moreover, the main factors driving this efficiency are analyzed and possible improvements to the system are determined. The numerical data for the analysis is produced by a fully transient mathematical model made for this study.

The analysis of the HBS is executed using four different cases varying in sources and services. The sources are defined below:

1. Hydrogen production coupled to the power grid (GD): The hydrogen production is determined by a maximum spot price for power. This spot price originates from historical data of the APX market for 2017.
2. Hydrogen production coupled to a wind farm (WT): The hydrogen production is determined by the wind speed. The additional power for the HBS originates from the power grid.

The two services are defined as follows:

1. Hydrogen for the chemical industry (CHEM): Hydrogen itself is delivered at a constant flow rate to the chemical industry.
2. Hydrogen as a power back-up (PWR): The consumption system is a hydrogen-fueled, combined cycle gas turbine (CCGT) for power generation that operates when there is a shortage of renewable energy or during premium spot prices for power.

The four cases are illustrated in Fig. 1.3.

- Case GD-CHEM. The HBS is driven by a maximum spot price for power and the service will be a constant hydrogen delivery flow rate to the chemical industry.
- Case WT-CHEM: The wind speed will be driving the power generation using a wind farm connected to the hydrogen production system. The HBS delivers a constant hydrogen flow rate to the chemical industry.
- Case GD-PWR: The power for hydrogen production is determined by a maximum spot price for power. Hydrogen consumption by a CCGT is governed by a minimum premium spot price for power. The generated power is sold back to the power grid.
- Case WT-PWR: A certain constant base load is met either directly by the wind farm or indirectly by the CCGT via the HBS route.

It must be noted that non of the cases are HRESs as power from the grid originates from non-renewable energy sources. The power grid is used for the GD cases, but also for the WT cases as the power grid is used for all power consumption except for the hydrogen production system. Therefore, the cases will be referred to as hydrogen-based energy systems (HESs). The key focuses of this analysis lays on the system operability, transient behaviour, sizing and energy and exergy efficiencies.

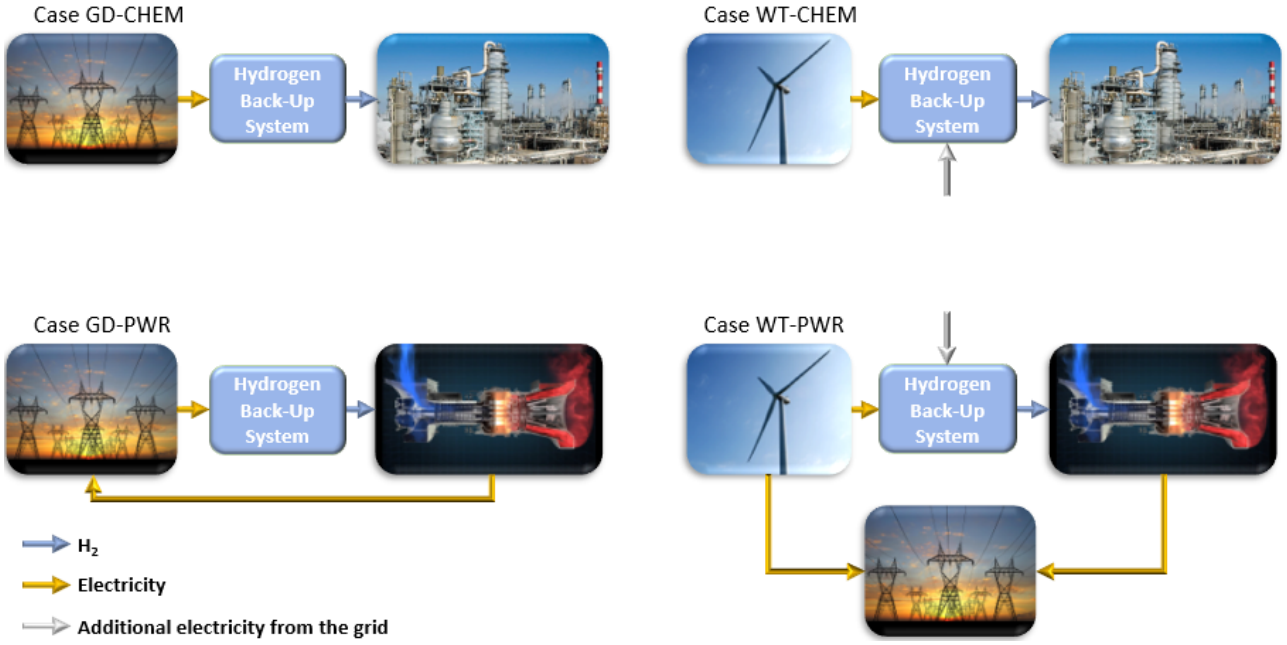

Figure 1.3: Simplified illustration of the four cases used for the HES.

1.2.4 Method

First, a thorough literature survey has been done aimed at HRES studies. These are compared in terms of extensiveness. The relevancy of the present study is evaluated and focus points are determined.

A source, system, service (3S) approach is used, bringing structure to the survey, to describe the various components of a HRES. For each component of the system one technology is selected which is best applicable for this study based on existing literature.

Thereafter, numerical modeling approaches from literature are investigated and selected based on the capability of capturing the transient and dynamical behaviour of the specific components. The chosen approaches are thoroughly described and then implemented in the used mathematical environment, Matlab® Simulink[2] (Falcão & Pinto, 2020).

The hydrogen production and transport models are validated with experimental data found in literature. Furthermore, a grid-dependency study is done on the transport model and an algorithm is written to make the transport model suitable for this study.

Once the model was set and validated, the HES was sized for each case. After sizing, a year of operation was simulated using the model. Thereafter, an analysis was done to get a thorough understanding of the system dynamics, performance, scale, losses and efficiencies.

A conclusion is written, based on the analysis, which answers the research questions. Finally, recommendations are presented giving insight on model and operational improvements.

1.2.5 Structure

Part I introduced the subject and the relevancy of this study and the assignment has been clarified by means of a problem statement, research questions, an objective. Furthermore, it summarizes the findings of the literature survey which determined the configuration of the HES, followed by a more thorough description of these components.

Part II gives a thorough description of the modeling approach and the validation of important HBS components.

Part III describes the sizing of the system for the different cases. Furthermore, the results of the simulation runs of the four cases are presented, analyzed and compared.

Part IV concludes the analysis and gives recommendations to improve the power-to-gas efficiency of a HBS and possible improvements to the model itself.

[2] `https://nl.mathworks.com/products/simulink.html`

Chapter 2

Hydrogen-based renewable energy system (HRES)

The meaning of a HRES is already introduced in section 1.1. The configuration of a HRES depends on the geographical location, the country regulations and market, the energy sources and the services it must provide. The geographical location, for instance, determines which sources will be most efficient, what storage technologies are possible to use, whether the system is grid-connected or stand-alone and what transport technologies can be used. Furthermore, the service it provides, influences the scale of the individual components like the total storage capacity and hydrogen consumption rate. In addition, the service depends on the market as the system can be used to supply, for example, electrical energy, heat, transportation fuel or feedstock for chemical processes.

A HRES system must consist of at least an electrical and a hydrogen system. However, additional systems for feedstock and waste streams can be implemented. The electrical system consists of components that convert, manage and control the electrical flow. It describes the grid demand, electrical loads and how the source energy is converted into energy suitable for driving the hydrogen production. The hydrogen system consist of components needed to produce, transport, store and utilize hydrogen.

2.1 HRES configuration

The configuration of the HRES is based on a source, system and service (3S) approach (Acar & Dincer, 2019). The 3S approach separates the components of the total system into 3 subsystems; source, system and service. The source includes the primary energy and feedstock which are needed for the HRES. The system is the HBS which includes the production, transport and storage of hydrogen. Finally, the service describes the end-use of the hydrogen. Acar & Dincer (2019) performed an elaborate comparative assessment of the possible HRES options, shown in Fig. 2.1, based on recent findings in literature. Figures 2.2 - 2.4 show the results of Acar Dincer (2019) where each option was assessed based on the following criteria:

- Economic performance: Considers initial, operating and maintenance costs.
- Environmental performance: Considers GHG emissions, land use, water discharge quality and solid waste generation.
- Social performance: Considers impact on public health, employment opportunities, training opportunities and public acceptance.

- Technical performance: Includes energy and exergy efficiency, process control and feedstock.
- Reliability: Includes dependence on imported resources, predictability and scalability.

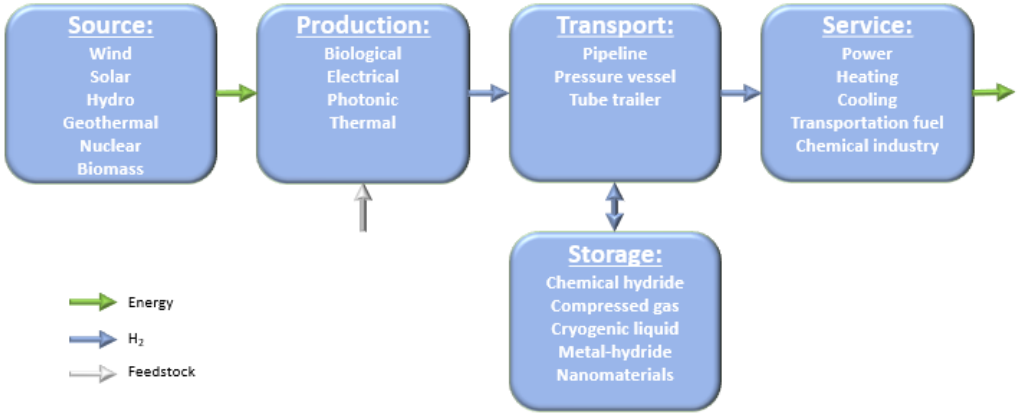

Figure 2.1: General HRES configuration options according to Acar & Dincer (2019).

2.1.1 Source

The source determines the energy needed to drive the hydrogen production. Section 1.2 clarified that this study focuses on a HES system driven by a wind farm or the power grid. The results from Acar & Dincer (2019), shown in Fig. 2.2, shows that wind energy scores second best together with hydropower after solar energy. Energy sources like biomass, geothermal, hydro and nuclear are not considered in this study as these are either not intermittent energy sources, do not have power as the main energy output or score significantly less on the overall performance compared to wind or solar energy, according to Acar & Dincer (2019).

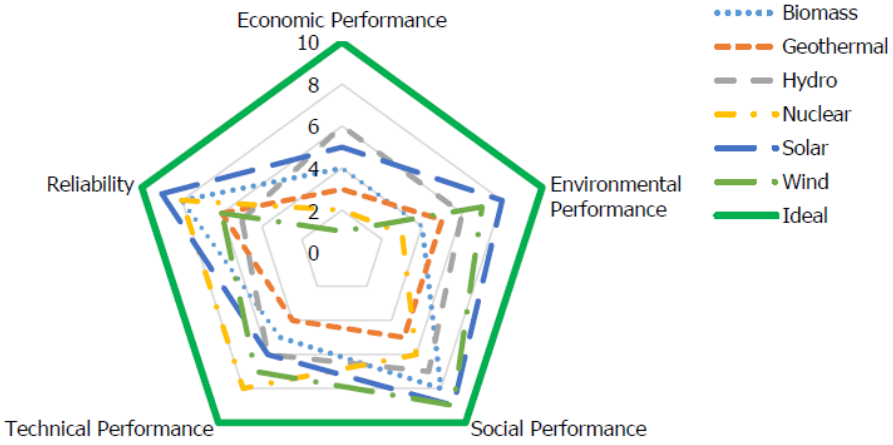

Figure 2.2: Overall performance of sources (Acar & Dincer, 2019).

Wind energy and solar energy are both intermittent renewable energy sources. Currently, however, the capacity factor of a wind farm on land is on average 25%, which is two-and-a-half times higher than that of a solar farm in The Netherlands. In addition, the wind farm capacity factor has the

potential to grow to 35-40% by implementing new design optimizations [1]. This makes a wind farm much more attractive.

2.1.2 System - Production

Acar & Dincer (2019) studied biological, electrical, photonic and thermal hydrogen production technologies. The rankings of these technologies are shown in Fig. 2.3. Biological production is not considered for this study as it needs micro-organisms instead of electrical power coming from the wind of power grid. Furthermore, a photonic process will not be considered as it needs sunlight and section 2.1.1 already elaborated that The Netherlands experience a lack of sunlight. Moreover, this technology is in the early research and development stage. Figure 2.3 shows that the electrical production technology has the best overall ranking where it outscores the thermal technology on all fronts except the social performance.

Figure 2.3: Overall performance of hydrogen production (Acar & Dincer, 2019).

Electrical hydrogen production is the logical choice due to the high overall performance and the fact that it needs electrical energy as the main input. Electrolysis and photolysis are both electrical hydrogen production processes. They are water-splitting technologies and thus only require water as a feedstock with oxygen as the sole by-product. Photolysis, however, needs sunlight, it suffers from a lack of effective photo-catalytic material and experiences extremely low efficiencies. Electrolysis, on the other hand, is for a large part already commercialized, an existing infrastructure is in place, it reaches reasonable efficiencies, performs well under highly dynamical circumstances and is scalable (Nikolaidis & Poullikkas, 2017). Therefore, electrolysis will be the choice for the hydrogen production system.

2.1.2.1 Electrolysis

There are three types of electrolysis: Alkaline electrolysis (AE), proton exchange membrane electrolysis (PEME) and solid oxide electrolysis (SOE). Table 2.1 summarizes several typical values of

[1] https://www.klimaatakkoord.nl/documenten/publicaties/2019/11/07/mmip2-hernieuwbare-elektriciteitsopwekking-op-land-en-de-gebouwde-omgeving

important electrolyzer parameters. SOEs are still in the research and development stage and are thus not applicable for large-scale hydrogen production, therefore, this technology will not be considered for this study.

Table 2.1: Parameters of state-of-the-art electrolysis technologies (Buttler & Spliethoff, 2018).

Specification	AE	PEME	SOE	Unit
Technology maturity	Commercial	Commercialization	Mid term	-
Cell temperature	60-90	50-80	700-900	°C
Cell pressure	10-30	20-50	1-15	bar
Current density	0.25-0.45	1.0-2.0	0.3-1.0	$A \cdot cm^{-2}$
Load flexibility	20-100	0-100	-100/+100	%
Cold start-up time	60-120	5-10	> 60	min
Warm start-up time	1-5	< 0.2	15	min
Nominal stack efficiency	63-71	60-68	100	%
Specific stack energy consumption	4.2-4.8	4.4-5.0	3	$kWh \cdot Nm^{-3}$
Nominal system efficiency	51-60	46-60	100	%
Specific system energy consumption	5.0-5.9	5.0-6.5	3.7-3.9	$kWh \cdot Nm^{-3}$
Max. nominal power per stack	6	2	< 0.01	MW
Hydrogen production per stack	< 1400	< 400	< 10	$Nm^3 \cdot h^{-1}$
Stack lifetime	55-120	60-100	8-20	kh
Efficiency degradation	0.25-1.5	0.5-2.5	3-50	%/year
Hydrogen purity	> 99.8	99.999	-	%
Investment costs	800-1500	1400-2100	> 2000	$€ \cdot kW^{-1}$
Maintenance costs	2-3	3-5	n.a.	% of investment per year

The AE is the most commercial technology and has the lowest investment and maintenance costs. Both AE and PEME can reach more or less the same efficiencies and are suitable for grid stabilising while at operating temperature. However, the PEME is chosen for this study due to the wide load flexibility, the fast dynamic response times for both cold and warm start-up, pure hydrogen production and high cell pressures (Buttler & Spliethoff, 2018). These factors will pose significant advantages when operating with intermittent energy sources and high storage pressures.

2.1.3 System - Storage

Acar & Dincer (2019) compared compressed gas, chemical and metal hydrides, cryogenic liquid and nanomaterial storage technologies. Figure 2.4 shows that the nanomaterial technology has the highest overall ranking and scores best on nearly all ranking criteria. However, this technique is in the early stages of development and is not applicable on industrial scale, therefore this option will not be considered. The cryogenic liquid technology scores lowest due to the extreme temperature requirements and hydrogen losses, making the technology expensive and hazardous. Chemical hydrides score well on reliability and environmental and technical performance, because the process is well understood and it has a high storage efficiency. However, it scores low on both economical and social performance due to the waste generation and logistics. The metal hydrides score slightly worse than chemical hydrides on economical and social performance mainly due to recycling challenges of storage material and waste. In terms of reliability it does better due to safe and modular operational possibilities with a wide applicability range and high storage densities. Compressed gas has the second lowest score, but scores high on reliability and reasonable on technical and economical performance. The high pressure negatively influences the environmental, social and economical performance due to safety risks and compression costs. It scores second best on economical performance thanks to the existing and well-developed technology which is available at relatively low costs (Acar & Dincer, 2019).

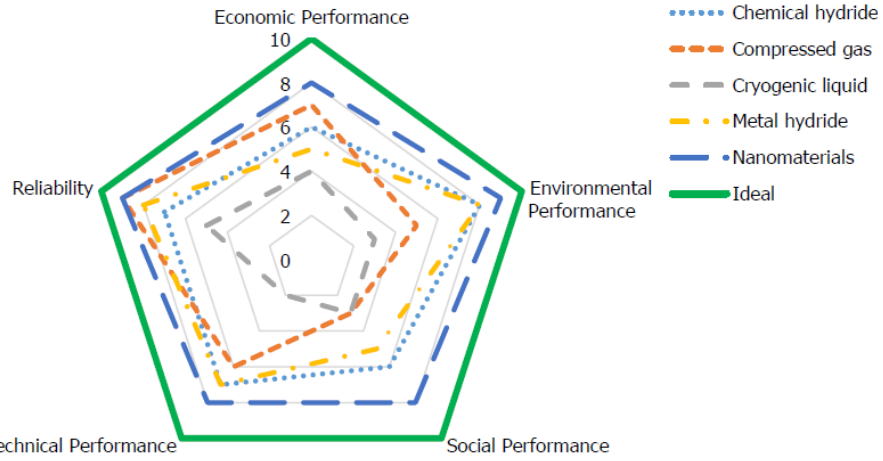

Figure 2.4: Overall performance of hydrogen storage (Acar & Dincer, 2019).

This study will use compressed gas as the storage technology. The main reason for not choosing the other options is that nanomaterial and metal hydride are still in the early research and development phase and not applicable on industrial scale, the overall performance of cryogenic liquid is way worse than compressed gas and chemical hydrides generate waste. Compressed gas storage is a well-developed technology which is applicable for large scale storage and scalable.

There are three main technologies which use compressed gas storage; hydrogen underground storage, storage in buried pipes and above ground spherical or cylindrical steel tanks (Bünger et al., 2016). Underground storage in, for instance, salt caverns, depleted oil reservoirs, aquifers and rock caverns, is significantly more cost effective than above ground tank storage technologies (Ripepi, 2018). Therefore, the above ground tanks will not be used. Even more specific, this study focuses on storing large quantities of pure hydrogen gas. Although, buried pipelines offer clean storage, they provide limited storage capacity and high specific costs (Ripepi, 2018). Salt cavern storage is the best choice of the underground storage possibilities as they are almost entirely hermetic, safe and least prone to contaminate the hydrogen gas. Furthermore, salt caverns are already widely used for natural gas storage and there are even several salt caverns in use for hydrogen storage in, for example, the United States and the United Kingdom (Andersson & Grönkvist, 2019).

2.1.4 System - Transport

The transport technology greatly depends on the storage method, the geographical location and the size of the system. In addition, the transport system must be able to quickly respond to changes in the supply and demand of hydrogen. Hydrogen can be transported as a gas, liquid or with material-based hydrogen carriers. As this study focuses on large scale, gaseous storage inside salt caverns only gaseous hydrogen transport will be considered. This gaseous transport can be done via pressure vessels arranged in tube trailers or via pipelines. Tube trailers are advantageous, because it requires the least intensive infrastructure changes and the knowledge is present due to experience with transportation of other gasses. However, delivery via tube trailers is not economically viable for long distances and high demands (Moradi & Groth, 2019). Therefore only pipeline transport will be considered as it is suited for high flow rates and pressures. Especially, for large scale systems, pipeline transport has proven to be the most cost effective per kilogram hydrogen delivered and it is obtained as the more environmental friendly way of delivery (Dincer & Acar, 2017). Lastly, pipeline offer quick response times due to the linepack.

2.1.5 Service

There are many services a HES can provide. For this study, the HES will provide two services. The first one, being an electrical power back-up which is able to balance supply and demand of electrical power. So, hydrogen will be consumed by a CCGT to produce electricity when renewables cannot satisfy the demand. This way, the surplus of renewable power can be stored in hydrogen and later be used when there is a power shortage.

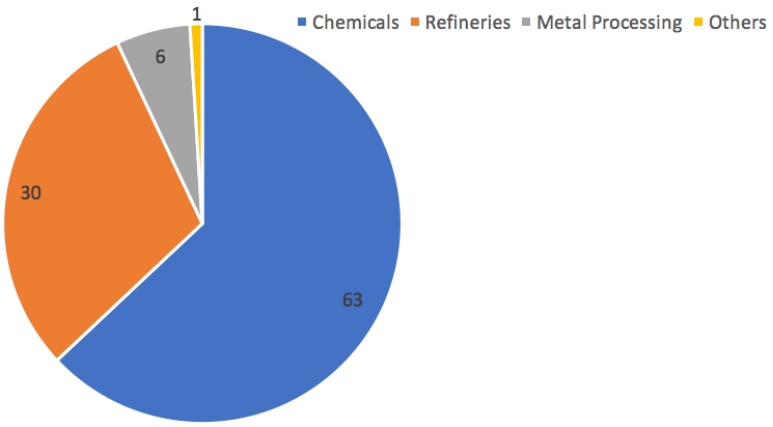

Figure 2.5: The total hydrogen consumption per industry[1].

The second service is producing hydrogen as feedstock for the industry. in Europe, 7 Mt of hydrogen is consumed by the total industry which is 90% of the total hydrogen market share. Figure 2.5[2] shows that most of the hydrogen is consumed by the chemical industry, followed by refineries. The main contributors to the high chemical industry market share are the producers of ammonia (84%), methanol (12%) polyurethane (2%) and nylon (2%). Here, almost 90% of the ammonia is used for the production of fertilizer[3]. Currently, the steel industry is not a significant hydrogen consumer. This can change, however, as hydrogen acts as a reductor agent in the metallurgy industry and using higher hydrogen volumes makes the process more efficient.

2.1.6 Conclusion

Figure 2.6 shows the resulting renewable energy source, the technologies used for the system and the services.

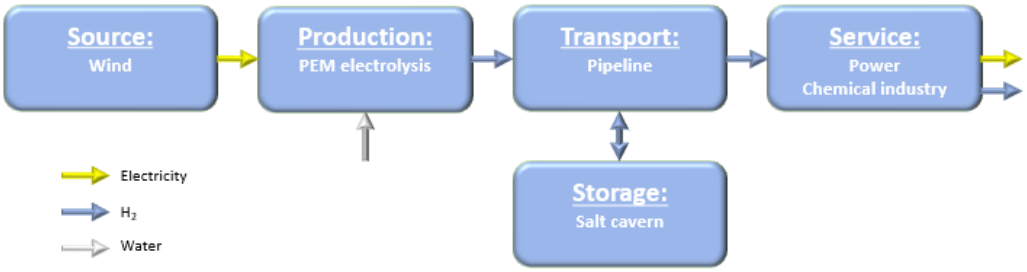

Figure 2.6: Chosen HRES configuration options for this study.

[2] https://hydrogeneurope.eu/decarbonise-industry
[3] https://hydrogeneurope.eu/hydrogen-industry

Chapter 3

Source, system and service technologies

This chapter gives a more elaborate description of the chosen technologies from chapter 2.

3.1 Wind energy

The wind provides solely kinetic energy which can by harnessed by a wind energy conversion system (WECS). A wind turbine extracts the kinetic energy from the air mass and converts it into mechanical energy. Theoretically, this conversion has a maximum efficiency of 59.3%, known as the Betz limit (Betz, 1967).

Generally, a WECS consists of a wind turbine, gearbox, a generator and a control system (Ayodele & Munda, 2019). However, direct drive systems, which do not use a gearbox, also exist and are praised for their easier operations and maintenance[1]. When a wind turbine is connected to a DC load, a rectifier is needed to convert the AC voltage output to a DC output. An electrical generator is driven by the turbine through a gearbox to produce electrical energy. A gearbox is needed when the inertia of the turbine does not allow the rotational speeds needed for the generator (Ayodele & Munda, 2019). Furthermore, a Maximum Power Point Tracking (MPPT) controller is oftentimes needed for a variable speed turbine to adjust the blade angles depending on the wind speed (Tawfiq et al., 2019). This controller assures that the optimal output is obtained within the operating range (Fathabadi, 2016).

Wind turbines either have a vertical (VAWT) or a horizontal (HAWT) axis. The main advantage of the latter is the variable blade pitch which enables the blades to optimally adjust the angle to obtain the maximum power from the wind. Also, the possibility of a high hub height results in more energy generation due to more significant wind speeds. Moreover, the perpendicular rotating blades result in high efficiencies. Drawbacks are the increased costs due to height, radar installation interference and the necessity for control systems to direct the blades in the correct position (Tawfiq et al., 2019).

Each turbine is designed to operate within a certain operating range called the cut-in and cut-out wind speeds. Outside this range the turbine must be stopped in order to prevent damage to the various components of the WECS. The low speed region, goes from zero to the cut-in speed. Here, the turbine must be stopped and disconnected from the grid to prevent the turbine from being driven by the generator. The second region is the moderate speed region which ranges from the cut-in speed

[1] https://www.power-eng.com/2011/03/01/direct-drive-vs-gearbox-progress-on-both-fronts/

to the rated speed. In this region the maximum available power is extracted from the wind by using controllers like MPPT. The last region is dominated by high wind speeds ranging from the rated speed to the cut-out speed. Here, the power is limited to the rated power to prevent overloading and mechanical failure of the WECS. After The cut-out speed the turbine must be shut-down to prevent possible structural overloads (Abdullah et al., 2012).

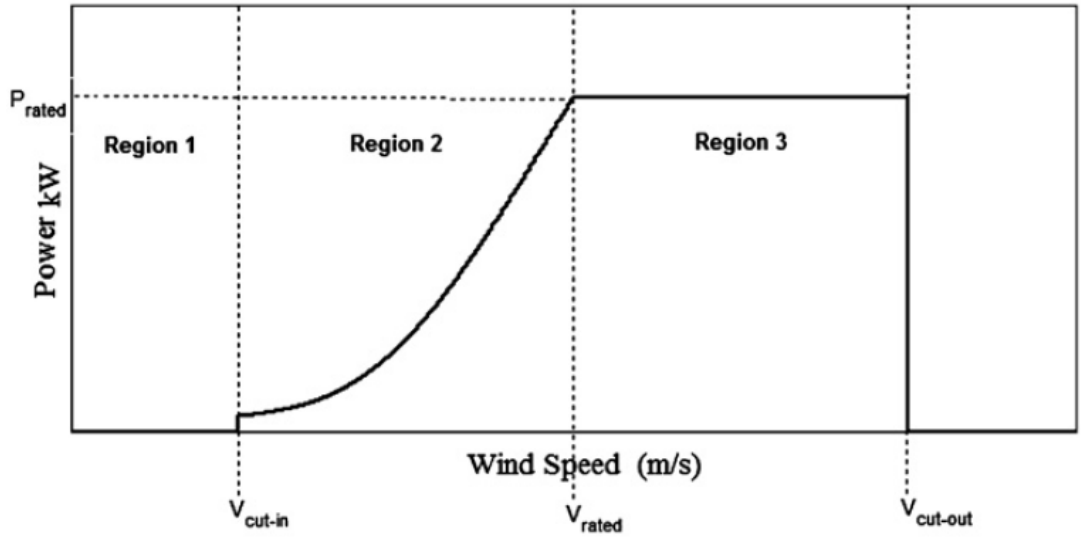

Figure 3.1: Typical power curve of a wind turbine (Abdullah et al., 2012).

3.2 Electrolysis

In this section a brief description of the electrolysis process is presented. Thereafter, the working principles of a PEME are elaborated.

3.2.1 Water splitting reaction

Electrolysis is the electrochemical conversion of water into hydrogen and oxygen done by an electrolyzer. All electrolyzer types make use of an anode, a cathode, an electrolyte and an electric current and water as the inputs. The main differences between the electrolyzer types are the electrolyte, catalysts and the operating conditions.

The overall reaction is equal for all types, as shown in Eq. (3.1). The direction of the reaction depends on the sign of the Gibbs free energy of the reaction, which can be evaluated using Eq. (3.2).

$$\mathrm{H_2O} + \Delta G_\mathrm{R} + T\Delta S_\mathrm{R} \rightarrow \mathrm{H_2} + \frac{1}{2}\mathrm{O_2} \tag{3.1}$$

$$\Delta G_\mathrm{R} = \Delta G_{\mathrm{f,H_2}} + \frac{1}{2}\Delta G_{\mathrm{f,O_2}} - \Delta G_{\mathrm{f,H_2}O} \tag{3.2}$$

Eq. 3.2 also holds for the enthalpy and entropy change of reaction. Filling in the values from Tab. 3.1 shows that $\Delta G^{\circ}_{\mathrm{R}} > 0$, making the reaction to proceed to the left side under NTP[2], thus resulting in water formation. However, an electrolyzer wants to split the water, making it necessary to supply the necessary electrical energy and heat needed for the reaction to proceed to the right side by means of an electrical current. Under normal conditions, $\Delta G^{\circ}_{\mathrm{R}} = 237.2 \left[\frac{\mathrm{kJ}}{\mathrm{mol}}\right]_{\mathrm{elec}}$ and $\mathrm{T}\Delta S^{\circ}_{\mathrm{R}} = 48.6 \left[\frac{\mathrm{kJ}}{\mathrm{mol}}\right]_{\mathrm{heat}}$ which are also known as the change in Gibbs free energy and the thermal irreversibilities of the reaction, respectively (Ulleberg, 2003). The overall reaction shows that energy is needed for the reaction to take place, making electrolysis an endothermic reaction. The total energy input for an electrolyzer cell operating under both reversible and normal conditions is equal to the total change in enthalpy of the water splitting reaction, $\Delta H^{\circ}_{\mathrm{R}} = 285.8 \left[\frac{\mathrm{kJ}}{\mathrm{mol}}\right]$. It must be noted that the values from Table 3.1 can vary as they depend on the reaction pressure and temperature. Often times, electrolyzers do not operate under normal conditions. The temperature dependency of G°_{R} can be calculated using thermodynamic principles.

Table 3.1: Thermodynamic formation properties of the water splitting reaction components at NTP.

Component	$\Delta H^{\circ}_{\mathrm{f}}$	$\Delta G^{\circ}_{\mathrm{f}}$	$\Delta S^{\circ}_{\mathrm{f}}$
-	$\mathrm{kJ \cdot mol^{-1}}$	$\mathrm{kJ \cdot mol^{-1}}$	$\mathrm{kJ \cdot (K \cdot mol)^{-1}}$
Hydrogen	0	0	130.59
Oxygen	0	0	205.03
Water (l)	-285.84	-237.19	69.94
Water (g)	-241.83	-228.59	188.72

Figure 3.2 shows the three different types of electrolyzers together with the in- and output components, catalyst materials, electrolyte types and the anode and cathode reactions.

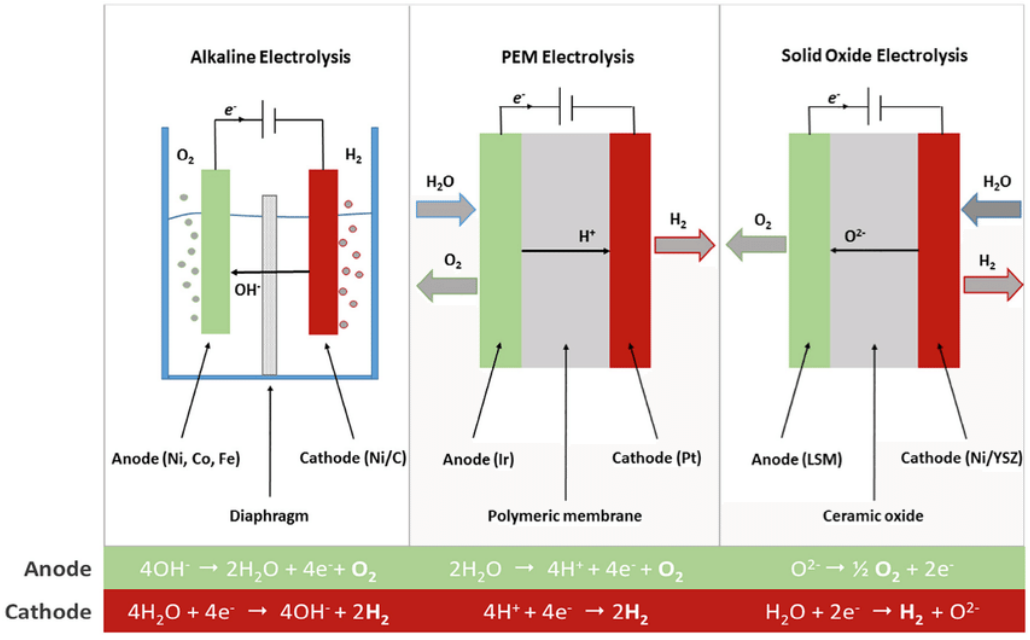

Figure 3.2: Difference between electrolyzer types (Sapountzi et al., 2017).

[2]Normal Temperature (293.15 K) and Pressure (1 atm)

3.2.2 PEM Electrolyzer system

Section 2.1.2 concluded that this study will make use of a PEME for the hydrogen production. More information on the alkaline and solid oxide electrolyzers can be found in Apx. H. Table 3.2 gives several commercially available PEMEs from different companies (Buttler & Spliethoff, 2018).

Table 3.2: Overview of several commercial PEME (Buttler & Spliethoff, 2018).

Manufacture [-]	Series [-]	Hydrogen rate [$Nm^3 \cdot h^{-1}$]	Rated power [MW]	Max. pressure [bar]	Spec. energy cons. [$kWh \cdot Nm^{-3}$]	η_{LHV} [-]	Load flexibility [%]
Giner Inc. (US)	Allagash	400	2	40	5	60	n.a.
Hydrogenics (CA)	HyLYZER-3000	300	1.5	30	5-5.4	56-60	1-100
Siemens (DE)	SILYZER 200	225	1.25	35	5.1-5.4	56-69	0-160
ITM Power (GB)		127	0.7	20–80	5.5	54	n.a.
Proton OnSite (US)	M400	50	0.25	30	5	60	0–100
AREVA H2Genu (FR)	E120v	30	0.13	35	4.4	68	10–150
H-TEC (DE)	ELS450	14.1	0.06	30-50	4.5	67	n.a.
Treadwell Corp. (US)		10.2	n.a.	76	n.a.	n.a.	n.a.
Angstrom Advanced (US)	HGH170000	10	0.06	4	5.8	52	n.a.
Kobelco Eco-Solutions (JP)	SH/SL60D	10	0.06	4–8	5.5–6.5	46–55	0–100
Sylatech (DE)	HE 32	2	0.01	30	4.9	61	n.a.
GreenHydrogenx (DK)	HyProvide P1	1	0.01	50	5.5	55	n.a.

The electrolyzer stack is where the half reactions take place which convert water into hydrogen and oxygen. Besides one or several stacks, a PEM electrolyzer system also consists of many other components in order to assure good working of the stacks called the balance of plant (BoP), as depicted in Fig. 3.4.

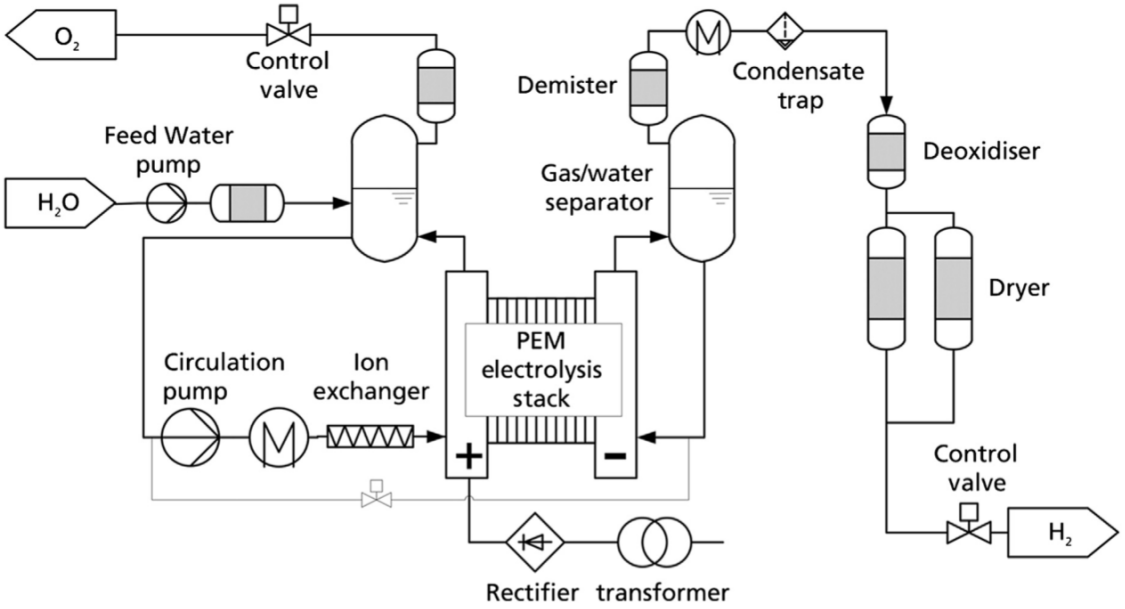

Figure 3.3: Schematic configuration of a PEME (Smolinka et al., 2015).

The BoP consists of components which carry out temperature and pressure regulation, stack in- and output conditioning and power supply regulation (Olivier et al., 2016). Depending on the technology suppliers, PEMEs can operate with only an anode circulating pump or with both an anode and a cathode circulating pump. Also, systems can both operate under equi-pressure or different pressures

at anode and cathode side (Bessarabov & Millet, 2018). Therefore, the configuration may differ slightly depending on the system, but most of the components given in Fig. 3.4 are often part of the system.

- **Power conditioning unit**: The electrical input is altered by a transformer and a rectifier in order to supply the stack with an appropriate DC power (Bessarabov & Millet, 2018).
- **Circulation pump**: During operation, a circulation pump maintains a constant water flow through the anode side of the electrolyzer stacks. This is done to supply water for the reaction, remove gases from the membrane electrode assembly to the gas separators and to improve the heat transport in the heat exchanger (Espinosa-López et al., 2018).
- **Heat exchangers (HEXs)**: A HEX is installed, after the circulation pump. The HEX removes the heat from the PEME which is generated due to stack overvoltages. At start-up, the heat exchanger is often turned off. During operation, the exchanger is used to maintain the operating temperature. An additional heat exchanger is installed after the hydrogen demister. This exchanger is used to cool down the water-saturated hydrogen to remove the water from the gas flow (Bessarabov & Millet, 2018).
- **Ion exchanger**: The water circulation loop can include an ion exchanger as a purification stage to maintain the required level of water purity. This device will be located between the heat exchanger and the inlet of the anode side of the stack.
- **Oxygen gas separator**: The oxygen gas separator is located after the anode outlet and separates the oxygen from the water. The oxygen is released into the atmosphere or compressed and stored for later use. The water is recycled back into the anode side water circulation loop.
- **Control valves**: These valves control the oxygen and hydrogen outlet pressures.
- **Demisters**: Demisters are located at the gas outlets of the hydrogen and oxygen separators and are used to remove droplets and aerosols from the gas flow.
- **Feed water pump**: Water is converted into hydrogen and oxygen by the electrolysis process. Therefore, a feed water pump is installed to add water to the system.
- **Water management unit**: The anode must be fed with purified and de-ionized water. This unit purifies the external water supplied by the feed water pump using water filters and ion exchangers (Bessarabov & Millet, 2018).
- **Water storage tank (optional)**: A storage tank is installed to store the demineralized water. From there a refilling pump is used to pump the water into the oxygen gas separator.
- **Hydrogen gas separator**: This separator is installed at the cathode outlet and separates the hydrogen from the water. The water is transferred back to the anode side at regular time intervals using a valve (Bessarabov & Millet, 2018).
- **Condensate trap**: A condensate trap is installed to reduce the dew point.
- **Deoxidizer**: The deoxidizer removes oxygen traces from the hydrogen flow by catalytic recombination.
- **Dryer**: The dryer is installed to dry out the water resulting from the deoxidizer.

3.2.2.1 PEM electrolyzer stack

An electrolyzer stack often consists of multiple cells which are held together by the end plates. Each cell consists of two bipolar plates and a membrane electrode assembly (MEA), as shown in Fig. 3.4. The bipolar plates have flow channels which direct and distribute the different mass flows. Under ideal conditions, water enters and oxygen leaves the bipolar plate at the anode side and hydrogen leaves the bipolar plate at the cathode side. An external electrical current is applied to the anode and cathode bipolar plates resulting in electron transport through the outer circuit of the electrolyzer cell, leaving the anode side positively charged and the cathode side negatively charged.

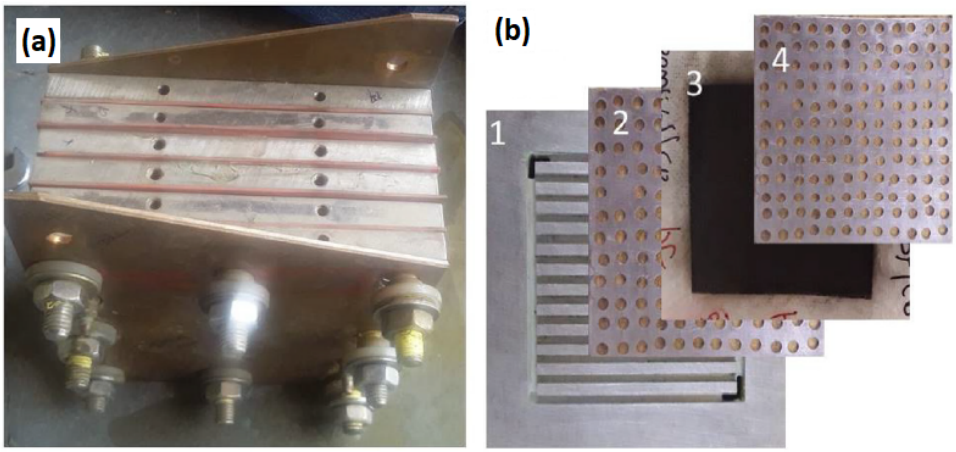

Figure 3.4: (a) Typical PEME stack, (b) Components of a single cell; 1. Bipolar plate, 2. Anode current collector, 3. MEA, 4. Cathode current collector. (Kumar & Himabindu, 2019).

The MEA consists of two gas diffusion layers, two catalytic layers and a proton exchange membrane (PEM). The anode gas diffusion layer realizes the diffusion of water vapor from the bipolar plate to the anode catalyst layer. The anode catalyst layer is where the oxygen evolution reaction (OER) takes place (Yigit & Selamet, 2016). Here, the water reacts with the catalyst to split into oxygen, hydrogen ions (H^+) and electrons. The gaseous oxygen diffuses through the anode gas diffusion layer to the anode bipolar plate. The electrons are driven through the outer circuit due to the applied voltage. The hydrogen atoms are positive ions (cations) which move through the PEM to the negatively charged cathode. At the cathode catalyst layer, the cations receive electrons from the outer circuit where they react with the catalyst to form hydrogen gas, known as the hydrogen evolution reaction (HER). The hydrogen gas diffuses through the cathode gas diffusion layer to the cathode bipolar plate where it is transported out of the cell (Toghyani et al., 2019). The bipolar plates and gas diffusion layers must be electrically and thermally conductive and chemically resistant in order to assure sufficient electron and heat transport.

$$\begin{aligned} 2H_2O \rightarrow O_2 + 4H^+ + 4e^- \qquad & \text{(Anode)} \\ 4H^+ + 4e^- \rightarrow 2H_2 \qquad & \text{(Cathode)} \end{aligned} \tag{3.3}$$

A solid polymeric membrane is used as an electrolyte, making the device compact with a membrane thickness of 20-300 µm which also resolves the leaking issue which often occurs in AEs. Furthermore, the electrolyte provides high proton conductivity, high pressure possibilities and low gas permeability (Aouali et al., 2017; Kumar & Himabindu, 2019). Due to the acidity and high voltages, these

types need noble catalysts which are expensive (Mohammadi & Mehrpooya, 2018). Iridium (Ir) and platinum (Pt) are often used for the anode and cathode, respectively (Sapountzi et al., 2017). PEMEs can make use of different solid polymeric membranes resulting in hydroxide anion or hydrogen cation transport through the membrane. However, the anion PEMEs, also known as solid alkaline electrolyzers, only exist at laboratory scale whereas the cation PEMEs are already commercialized.

The main challenge for cation PEMEs is to reduce the noble metal utilization. The anion PEME combines the advantages of the AE and the cation PEME. However, the electrolyte experiences a low hydroxide anion conductivity which must be improved to become a commercialized device (Sapountzi et al., 2017).

3.3 Hydrogen compression

At several locations inside the system gas compression is needed as hydrogen is produced at relatively low pressures[3]. Often directly after the electrolyzer a compressor is installed to increase the hydrogen pressure for transport through pipelines or to compress the hydrogen to the storage pressure.

3.4 Compressor types

Compressors can be classified as mechanical or non-mechanical compressors, as shown in Fig. 3.5. Mechanical compressors are widespread and are based on conversion of mechanical energy into gas energy. They can be positive displacement or dynamic (turbo) compressors. Positive displacement compressors are either reciprocating or rotary and they raise the pressure by reducing the volume in which the hydrogen gas is confined. This increases the number of collisions of the molecules among each other and with the surrounding walls resulting in a higher gas pressure (Sdanghi et al., 2019).

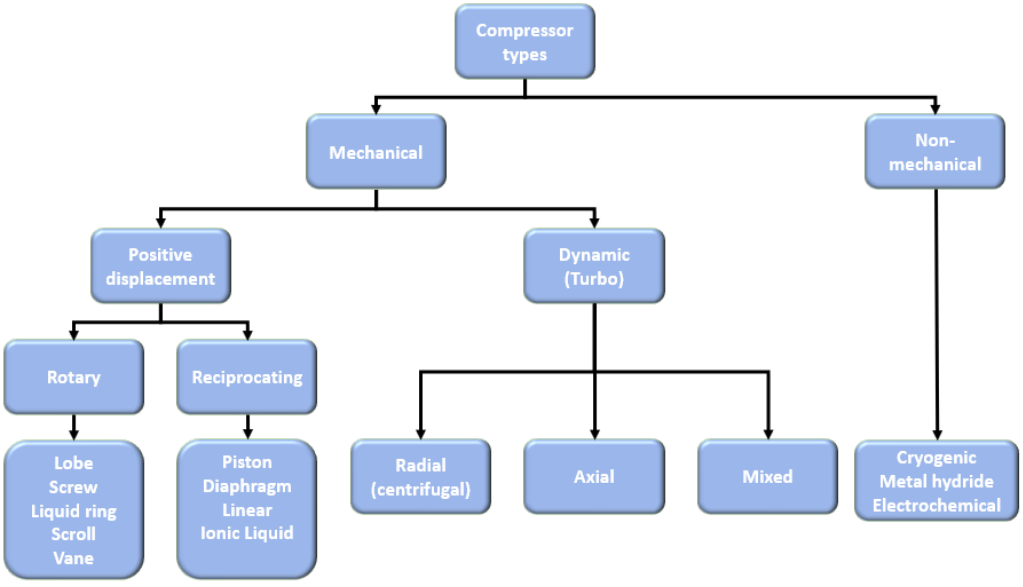

Figure 3.5: Overview of compressor types.

Dynamic compressors, on the other hand, first raise the velocity of the gas and then lower the flow velocity again by increasing the flow area leading to an increase in the static pressure. Due to the low

[3]https://www.energy.gov/eere/fuelcells/gaseous-hydrogen-compression

volumetric density of hydrogen, the compressor efficiency will be low (Makridis, 2017). Therefore, these compressors are not used for this study.

Non-mechanical compressors make use of other mechanisms as the ones described above. This category includes cryogenic, metal hydride and electrochemical compressors and are all still in the early research and development stage and only experience low flow rates (Sdanghi et al., 2019). Therefore, also these types will not be used for this study.

3.4.1 Positive displacement compressors

Reciprocating piston compressors (Fig. 3.6) are commonly used for compressing hydrogen above 30 bar levels, especially the oil-free variant. They are applicable for moderate flow rates and high pressures. The reciprocating motion of the piston causes the compression inside the gas chamber. The downward movement towards the bottom dead centre (BDC) causes the inlet valve to open, letting the gas into the chamber. The upwards movement towards the top dead centre (TDC) compresses the gas until the desired pressure is reached after which the gas will be discharged. The flow rate depends on the volume of the cylinder and the number of cycles per unit time. A bigger cylinder allows for more gas to enter the compression chamber. However, the bigger cylinder also increases the inertia of the piston which results in a lower compression speed. Therefore, a balance between volume and compressor speed must be determined to find the desired flow velocity. So, the operating conditions are essential sizing a compressor. Tight tolerances are needed to prevent leakage due to the extremely small hydrogen atom size, leading to increased friction losses. Moreover, the moving parts lead to pressure fluctuations resulting in vibrations, noises and possibly explosions. On the other hand, the devices are highly flexible and multi-stage configurations result in high pressure ratios (Sdanghi et al., 2019).

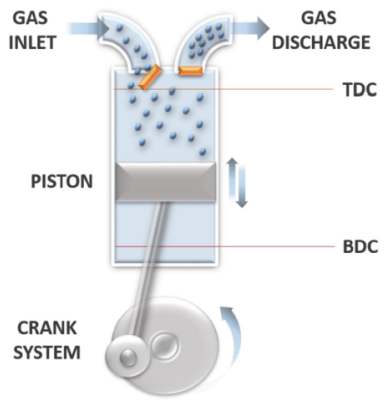

Figure 3.6: Reciprocating compressor (Sdanghi et al., 2019).

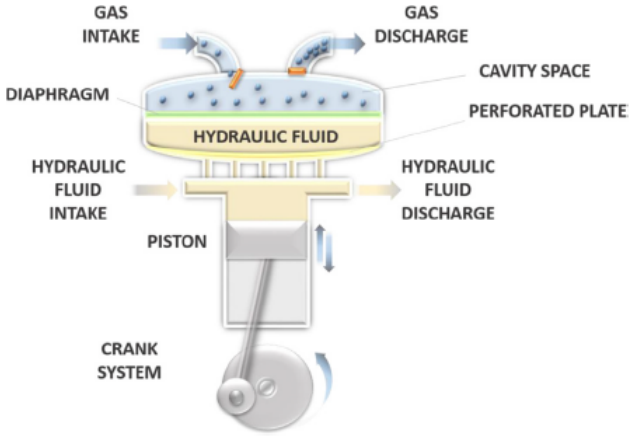

Figure 3.7: Metal diaphragm compressor (Sdanghi et al., 2019).

Diaphragm compressors (Fig. 3.7) experience high flow rates, low power consumption and low cooling requirements which makes them highly suitable for hydrogen compression. The low cooling requirements are the result of heat dissipation to the hydraulic fluid. These devices are ideal when contact between the gas and the piston should be prevented. The diaphragm is made of a process, middle and hydraulic plate which are on the gas, middle and hydraulic oil side, respectively. It operates somewhat identical to the reciprocating piston compressor. The gas is always separated from the oil

circuit resulting in an unchanged purity of the gas. Also, high volumetric efficiencies can be reached with these devices. However, the mechanical stresses during operation on the diaphragm lead to durability issues. Therefore, although high flow rates are possible, lower flow rates are preferred to limit the stresses on the diaphragm and prolong its lifetime (Sdanghi et al., 2019).

Linear compressors, often used in cryogenic hydrogen applications, are driven by Stirling cycle coolers. The compression process is identical to that of reciprocating compressors. However, in this case the piston is driven by a linear motor with a resonating spring system. This leads to less moving parts and thus less costs. These type of compressors are not used for hydrogen compression as they are considered an innovative solution for hydrogen compression, but efforts are done to make configurations suitable for hydrogen compression (Sdanghi et al., 2019).

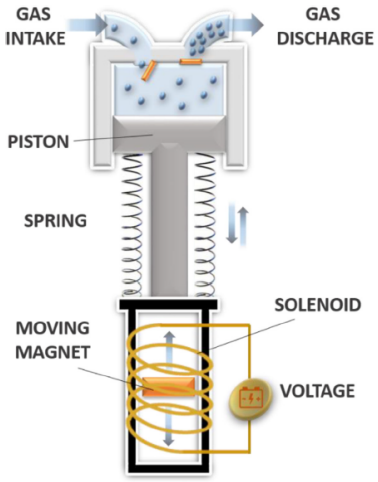

Figure 3.8: Linear compressor (Sdanghi et al., 2019).

3.5 Pipeline transport

Hydrogen delivery forms one of the four key parts of the HBS and contributes to the energy use, emissions and costs (Moradi & Groth, 2019). For hydrogen to become a successful replacement for fossil fuels, its delivery infrastructure must provide the same or a better level of safety, convenience and functionality as the existing fossil fuel infrastructure. Furthermore, hydrogen can be produced from various energy sources making both local and large, centralized production sites possible. The hydrogen infrastructure must be able to cope with these dispersed production sites[4].

Pipelines are best suited for transporting large quantities of gaseous hydrogen over large distances (Witkowski et al., 2017). Industrial hydrogen pipelines are already used by companies which produce hydrogen locally and then use the hydrogen as a feedstock for a nearby plant in which case the pipelines are very short (Gondal, 2016). On several locations in Europe, however, there are long pipelines in use which are shown in Tab. 3.3.

The existing length of hydrogen pipelines is insignificant compared to the natural gas infrastructure. The costs of laying out a pipeline infrastructure is immense and is even higher for hydrogen as hydrogen pipelines are these pipelines must withstand higher pressures, embrittlement and use tighter

[4] https://www.energy.gov/eere/fuelcells/downloads/fuel-cell-technologies-office-multi-year-research-development-and-22

Table 3.3: Operational hydrogen pipelines (Gondal, 2016).

Location [-]	Length [km]	Inner diameter [mm]	Annual transportation [$m^3 \cdot yr^{-1}$]	Operating pressure [bar]
France	550	100	$200 \cdot 10^6$	-
Belgium	80	150	-	100
England	16	-	-	50
Germany	220	100-300	$1 \cdot 10^6$	20

tolerance to prevent leakage (Gondal, 2016). Besides the material costs, also the installation costs, rights of way and miscellaneous costs are significant contributors to the costs. These installation costs are highly influenced by the pipe diameter (Yang & Ogden, 2007).

Pipelines are used for gas flow rates of several thousands of $kg \cdot hr^{-1}$ and are considered to have the lowest operation costs. However, the investment costs are very high, therefore steady, high-volume gas flows are preferred. The transmission and distribution pipelines typically operate between 30-150 bar and 10-50 bar, respectively, to enhance the delivery speed[5].

Besides hydrogen transportation, pipelines also serve as hydrogen storage. The amount of storage is significant and depends on the length, diameter and operating pressure of the pipeline. In case that the supply exceeds the demand, the hydrogen stalls in the pipeline which is known as the linepack (Gondal, 2016). The linepack makes it possible to instantly react to supply and demand variations.

3.5.1 Pipeline components

A pipeline assembly consists of many components. The main components that are of interest for modelling pipelines are listed below (Gondal, 2016).

- Pipelines: The pipelines contain and direct the gas flow to the desired location. These pipes must be leak proof, corrosion resistant, strong, durable and have low friction losses. The pipes are made out of mild, low carbon steel, because this leads to less significant embrittlement.
- Compression stations: Due to viscosity of the gas and friction losses inside the pipe, the flow encounters a resistance. This flow resistance results in a pressure drop along the pipeline. As the pressure in the pipe must stay within defined limits, compressors are installed at certain distances to increase the pressure, as shown in Fig. 3.9.
- Pressure-reduction stations: These stations are installed to connect two pipelines where the second pipeline operates at a lower pressure. This is done by a throttling valve.

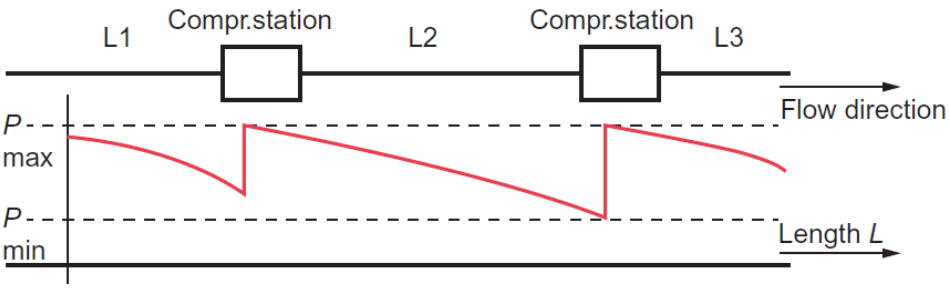

Figure 3.9: Pressure drop along pipelines (Gondal, 2016).

[5] https://www.energy.gov/sites/prod/files/2015/08/f25/fcto_myrdd_delivery.pdf

3.6 Salt cavern storage

Large-scale storage of hydrogen is an integral part of the HBS. Salt caverns are cylindrical-like domes at depths of several hundredths of metres under the surface. Bringing forth multiple advantage in terms of high-pressure gas storage. The often enormous size allows for large quantities of gas storage where high operational pressures are allowed. The minimum and maximum allowable hydrogen pressure increases even more when the cavern is located deeper underground as these values are often based on the geostatic rock pressure (Gabrielli et al., 2020). Above ground, only a small footprint is necessary and the specific investments costs per megawatt-hour are low (Wolf, 2015). The walls of salt caverns are stable and impenetrable to gas for sufficiently long periods. Also, the properties of the salt protects the cavern walls from fracturing and thus the loss of impermeability. The saline environment limits consumption of the stored hydrogen by biochemical reactions (Gabrielli et al., 2020). Furthermore, both low and high injection and withdrawal rates are possible making this storage type highly dynamic (Gabrielli et al., 2020).

Table 3.4: Typical storage capacities for several hydrogen storage technologies (Wolf, 2015).

Storage type [-]	Storage [MWh]	Storage type [-]	Storage [MWh]
Low pressure vessel	150	High pressure tube	4,300
High pressure vessel	2,250	Cavern	240,000

The impermeable nature of the salt cavern walls is beneficial for storing hydrogen, but only true for the undisturbed region. This is the region where the salt rock properties have not been modified by the excavation work. The disturbed region, or damaged zone, does develop a limited permeability to the gas. The reach of the damaged region is typically up to a salt rock depth of the cavern radius. Here, the pores in the damaged salt rock are occupied by the stored gas. During injection, the pressure inside the cavern increases and subsequently the pressure inside the salt rock increases due to a mass flux into the salt rock. When the injection stops, the mass flux into the salt rock will continue until an equilibrium pressure is reached between the cavern and the salt rock. During withdrawal the exact opposite occurs, resulting in a mass flux from the salt rock into the cavern, as shown in Fig. (3.10). However, the mass flux has a negligible effect on the cavern pressure if certain constraints are considered to ensure safe operation. This is also clear from the figure where the black line stays linear during injection, discharge and rest periods while the pressures at 20 and 50 metres still change. This is a result of the insignificant amount of mass in the salt rock pores compared to the stored mass inside the cavern (Gabrielli et al., 2020).

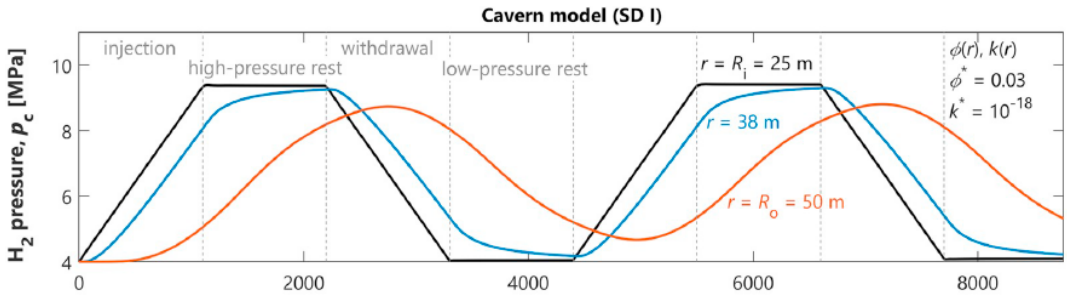

Figure 3.10: The black line represents the hydrogen pressure at the cavern wall. The blue and red line are the hydrogen pressure deeper in the cavern wall (Gabrielli et al., 2020).

Part II

Chapter 4

Modeling of system components

This chapter gives an elaborate overview of the modeling approach that is used for the HRES model. The various system components are modeled using the reviewed literature. All Matlab®-script and Matlab® Simulink input parameters for the various submodels are tabulated in Apx. E and F. Figure 4.1 gives the lay-out of the modeled HBS.

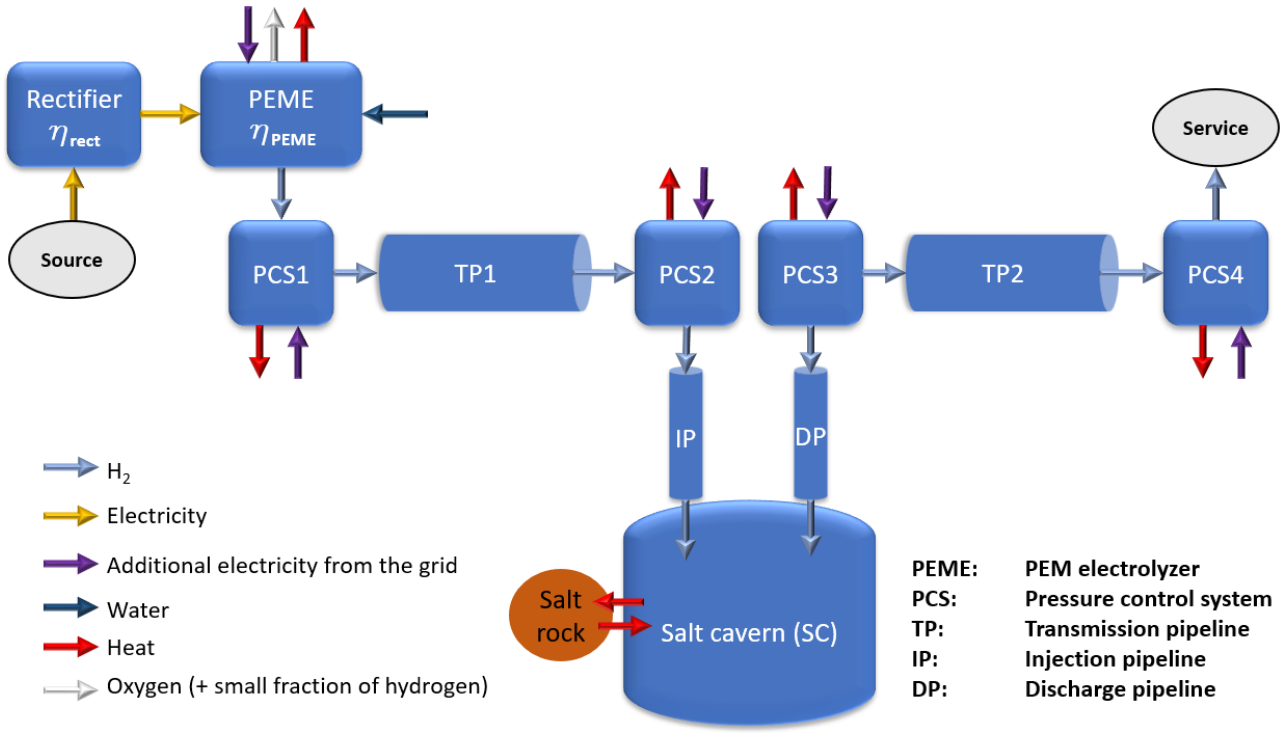

Figure 4.1: Schematic representation of the modeled hydrogen back-up system (HBS).

The HBS model uses a rectifier and a PEME to convert the source power into hydrogen. Here, the rectifier model uses a constant power conversion (AC to DC) efficiency. A zero-dimensional PEME model converts the electrical energy into chemical energy with a time dependent efficiency influenced by the PEME temperature, pressure and power consumption. The PEME BoP uses power coming from the power grid. A transport system consisting of pressure control station 1 (PCS1) and transmission pipeline 1 (TP1) delivers the hydrogen to the cavern. The hydrogen is injected into a 1000 metre deep cavern by PCS2 and an injection pipeline with nozzle (IP). The time dependant cavern

storage pressure and temperature is influenced by the injection and discharge hydrogen flow rates and heat exchange with the surrounding salt rock. A discharge pipeline (DP) is connected to PCS3 which adjusts the hydrogen temperature and pressure for TP2. Lastly, PCS4 adjusts the hydrogen flow properties to the desired service values. A PCS can use a throttling valve or a compressor, depending on the necessary pressure ratio, followed by a heat exchanger (HEX). The power consumption of the compressors with constant isentropic efficiency depend on the inlet flow properties of hydrogen and the pressure ratio. The heat removal by the HEX depends on the inlet and outlet properties of the hydrogen flow. The hydrogen is isothermically transported though pipelines using an one-dimensional model.

The detailed model is further elaborated in the following sections. The lay-out of the Matlab® Simulink model can be found in Apx. J.

4.1 Component properties

The fluids will be modeled as real gasses, therefore, REFPROP®[1] was used for estimating the component properties, making the equations of state obsolete. As Matlab® Simulink is not able to work directly with REFPROP®, property tables are made via a Matlab®-script. In Matlab® Simulink, 2D look-up tables are used to find the corresponding values. The ranges used for the tables are found in Apx. D.

4.2 Wind farm modeling

This section describes the modeling approach for the WECS.

4.2.1 Wind modeling

The wind speed is modeled using real-world historical hourly data obtained from the Koninklijk Nederlands Meteorologisch Instituut (KNMI)[2]. The wind power is modeled using Eq. (4.1).

$$P_{\text{wind}} = \frac{1}{2}\rho_{\text{air}} A_{\text{tur}} v_{\text{wind}}^3 \tag{4.1}$$

4.2.2 Wind turbine modeling

Generally, turbine models are classified into dynamic and static model. A dynamic model makes use of very short time steps in the range of seconds in order to capture the transients due to the inertia of the wind turbine caused by changing wind speeds. Static models are used for larger time steps as inertia is not taken into account. For system models, it is more convenient to use the static approach for a wind turbine as the overall results will not vary significantly (Valverde-Isorna et al., 2016). A relatively simple wind turbine model is used as it is not of interest for this study to make it complex. More complex models can be found in literature (Colombo et al., 2019; P. Li et al., 2019; Fathabadi, 2016).

The mechanical power is the product of the turbine power coefficient and the wind power. Normally, the power coefficient is a function of the tip speed ratio (TSR) and the blade pitch angle. The TSR

[1] `https://www.nist.gov/srd/refprop`
[2] `http://projects.knmi.nl/klimatologie/uurgegevens/selectie.cgi`

is the ratio between the velocity of the blade tip and the wind speed and the blade pitch angle is the angle at which the blade is positioned which is controlled by a MPPT controller. However, this study uses a constant power coefficient as this greatly simplifies the model, as shown in Eq. (4.2).

$$P_{\text{mech}} = C_{\text{tur,max}} \cdot P_{\text{wind}} \tag{4.2}$$

The rated mechanical power is modeled using Eq. (4.3) and makes use of the rated wind speed and the maximum power coefficient of the turbine.

$$P_{\text{rated}} = C_{\text{tur,max}} \cdot (\frac{1}{2}\rho_{\text{air}} A_{\text{tur}} v_{\text{rated}}^3) \tag{4.3}$$

The mechanical power produces a torque on the turbine shaft. This shaft is often attached to a gearbox to raise the rotational speed of the generator shaft. This generator produces the electrical output of the WECS. The turbine, gearbox and generator are all necessary components for a WECS, but they generate additional efficiency losses. The total WECS electrical power output is modeled using Eq. (4.4), which is the product of the number of turbines used, the overall WECS efficiency and the wind power.

$$\begin{aligned} P_{\text{WECS}} &= N_{\text{tur}} \cdot \eta_{\text{WECS}} \cdot P_{\text{wind}} \\ \text{with} \quad \eta_{\text{WECS}} &= C_{\text{tur,max}} \cdot \eta_{\text{gb}} \cdot \eta_{\text{gen}} \end{aligned} \tag{4.4}$$

4.2.3 Rectifier

A wind turbine generates electrical power that has a variable voltage magnitude and frequency depending on the wind speed. Therefore, several power electronics are needed to make the voltage suitable for the given load (Fathabadi, 2016).

A rectifier is an electronic device which is installed to convert the alternating current (AC) coming from the wind farm to a direct current (DC) suitable for the PEME. The voltage ratio is influenced by power dissipation into heat and losses in the transformer. A rectifier efficiency is typically somewhere between 80 - 95 % (Nematollahi et al., 2019). The rectifier model is kept simple with a constant efficiency, as shown in Eq. (4.5), which is common in literature (Nematollahi et al., 2019; Ayodele & Munda, 2019).

$$P_{\text{rect}} = \eta_{\text{rect}} \cdot P_{\text{WECS}} \tag{4.5}$$

4.3 PEM electrolyzer modeling

The modeling approach is based on the work of Espinoza-López et al. (2018), Sartory et al. (2017) and Yigit & Selamet (2016). The PEME model uses physical and electrochemical principles which were simulated zero-dimensional. The PEME model consists of multiple blocks and sub-blocks, as shown in Fig. 4.2. In addition, an exergy block is used for exergy calculations.

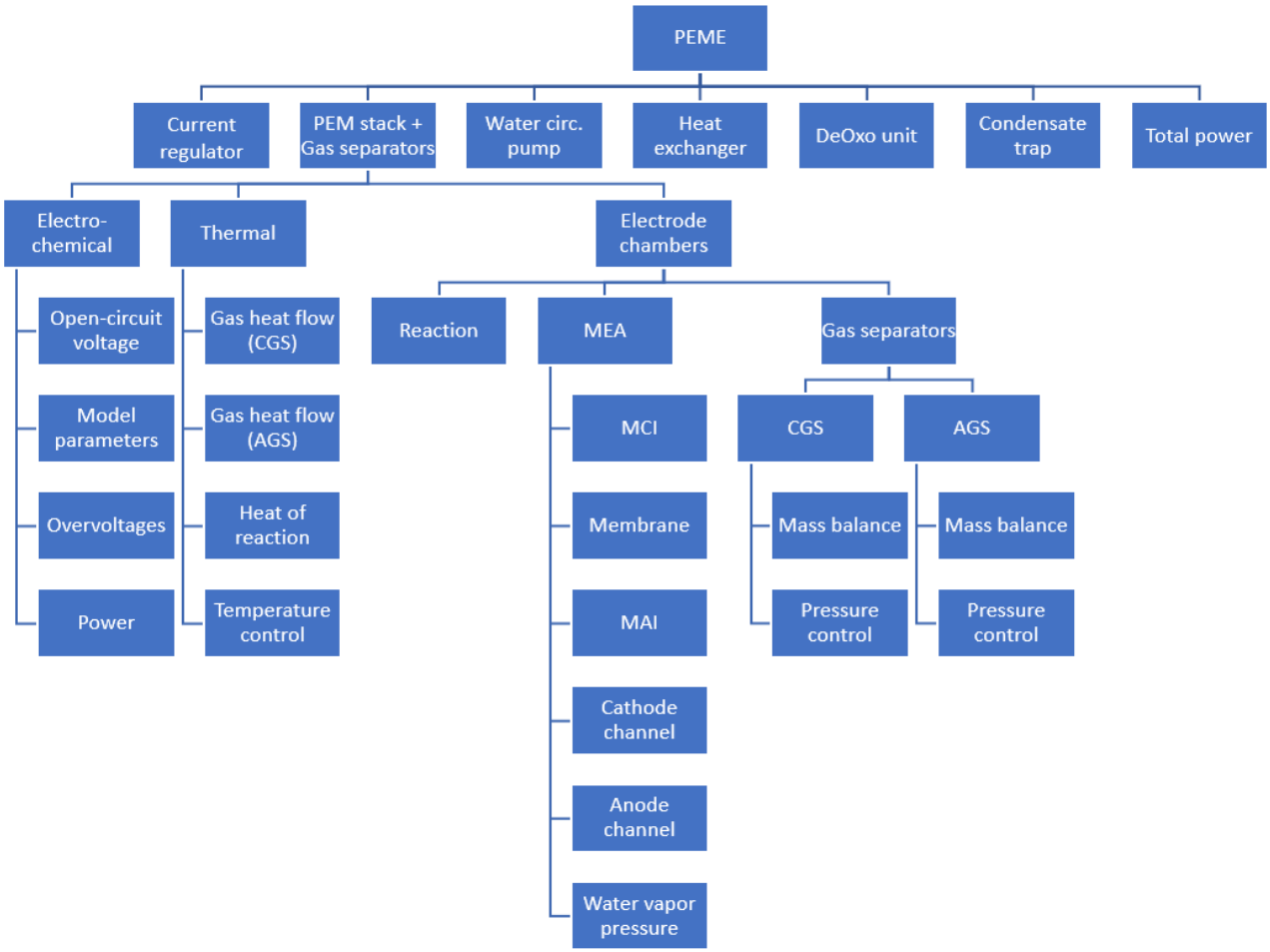

Figure 4.2: Block diagram of the PEME model.

4.3.1 Electrochemical submodel

The following assumptions are made:

- Liquid water exerts a partial pressure that is equal to its saturated vapor pressure at the given temperature.
- Is it assumed that the fluid regions of the electrolyzer are saturated with water vapor at all times.
- Cathode activation overvoltage is neglected.
- The exchange current density is not a function of physical characteristics of the membrane and catalyst, but it is expressed using an Arrhenius expression.

- The membrane protonic conductivity is assumed to be a function of temperature only.
- Concentration overvoltages are neglected due to the relatively low current densities.
- Electrical overvoltages due to electrical resistances are neglected as detailed knowledge is needed of the electrical components and it only leads to small errors.

4.3.1.1 Cell voltage

The theoretical cell voltage can be described using Eq. (4.6) and is the sum of the reversible cell voltage and the activation, ohmic and concentration overvoltages. However, due to the assumptions made, the cell voltage used in the model is calculated using Eq. (4.7).

$$U_\mathrm{c} = U_\mathrm{rev} + U_\mathrm{act} + U_\mathrm{ohm} + U_\mathrm{conc} \tag{4.6}$$

$$U_\mathrm{c} = U_\mathrm{ocv} + U_\mathrm{act,an} + U_\mathrm{ohm,mem} \tag{4.7}$$

4.3.1.2 Open-cell voltage

The reversible voltage represents the electromotive force that is needed to start the electrolysis reaction and is modeled using Eq. (4.8). Here, the change in Gibbs free energy of the reaction is divided by the number of electrons (z) involved and the Faraday's constant (F). However, it is difficult to calculate the change in Gibbs free energy of the reaction as it needs the the change in molar entropy and enthalpy of reaction at different temperatures and pressures which can only be found using difficult empirical equations.

$$U_\mathrm{rev}(p,T) = \frac{\Delta G_\mathrm{R}(p,T)}{zF} \tag{4.8}$$

Therefore, Eq. (4.9), also known as the open-cell voltage or Nernst potential, is used. This equation uses an empirical approximation for the reversible cell voltage at normal pressure[3] (U°_rev). Here, U°_rev describes the influence of the temperature on the reversible cell voltage at SATP[4]. The open-cell voltage is thus a function of pressure and temperature. (Espinosa-López et al., 2018).

$$\begin{aligned} U_\mathrm{rev} \approx U_\mathrm{ocv} &= U^\circ_\mathrm{rev}(T_\mathrm{st}) + \frac{RT}{zF}\ln\left(\frac{p_{\mathrm{O}_2}^{\frac{1}{2}} \cdot p_{\mathrm{H}_2}}{p_{\mathrm{H_2O}}}\right) \\ \text{with} \qquad U^\circ_\mathrm{rev}(T_\mathrm{st}) &= U_\mathrm{rev,SATP} - 0.0009 \cdot (T_\mathrm{st} - T_\mathrm{SATP}) \end{aligned} \tag{4.9}$$

The partial pressures of hydrogen at the cathode side and oxygen at the anode side are modeled using Dalton's law. The saturated vapor pressure is solely a function of temperature and is modeled using look-up tables made with REFPROP® .

[3] normal pressure = 1 atm

[4] Standard Ambient Temperature (298.15 K) and Pressure (1 atm)

$$
\begin{aligned}
p_{\mathrm{H_2,cat}} &= p_{\mathrm{cat}} - p_{\mathrm{O_2,cat}} - p_{\mathrm{H_2O,cat}} \\
p_{\mathrm{O_2,an}} &= p_{\mathrm{an}} - p_{\mathrm{O_2,an}} - p_{\mathrm{H_2O,an}} \\
p_{\mathrm{H_2O}} &= f(T)
\end{aligned}
\tag{4.10}
$$

4.3.1.3 The activation voltage

The activation voltage is the energy required at the anode and cathode to start the oxygen and hydrogen evolution reactions, respectively. This voltage can be estimated using the Butler-Volmer equation and takes the electrochemical kinetics into account. However, the reaction kinetics at the cathode are much faster than at the anode. Therefore, the cathode activation overvoltage is neglected as this leads to insignificant losses. Only the anode activation overvoltage is taken into account, as shown in Eq. (4.11). The charge transfer coefficient (α_{an}) can vary between 0.1 - 0.9, but is often taken as 0.5 (García-Valverde et al., 2012). The anode exchange current density ($i_{0,\mathrm{an}}$) depends on the physical characteristics of the membrane and catalyst and on the operating temperature (Liso et al., 2018). Literature suggests several values for the exchange current density which depend on the catalyst type. However, as the value also depends on temperature, the Arrhenius expression can be used to predict the exchange current density. This expression makes use of the activation energy needed for electron transport in the anode (E_{exc}) and the exchange current density at SATP ($i_{0,\mathrm{an,SATP}}$), as shown in Eq. (4.12).

$$
U_{\mathrm{act,an}} = \frac{RT}{2\alpha_{\mathrm{an}}F} \cdot \operatorname{asinh}\left(\frac{i}{2i_{0,\mathrm{an}}}\right) \tag{4.11}
$$

$$
i_{0,\mathrm{an}} = i_{0,\mathrm{an,SATP}} \cdot \exp\left(-\frac{E_{\mathrm{exc}}}{R} \cdot \left(\frac{1}{T} - \frac{1}{T_{\mathrm{SATP}}}\right)\right) \tag{4.12}
$$

4.3.1.4 The ohmic overpotential

The ohmic overpotential (Eq. (4.13)), takes the cell voltage losses into account caused by electrical resistances in the electrodes, current collectors and the bipolar plates and the protonic resistance through the membrane. In literature, equivalent electrical circuits are often used. However, for this method many specific values for all the different components are necessary which are often not known to the user. Therefore, the presented method only incorporates the membrane protonic resistance, because this resistance is most dominant (Liso et al., 2018; Espinosa-López et al., 2018). The membrane resistivity can be expressed with the membrane thickness and the membrane protonic conductivity, as shown in Eq. (4.14). The protonic conductivity is a function of the water content of the membrane and the temperature. As the exact composition of the membrane is not known, the Arrhenius expression will be used again, as shown in Eq. (4.15). Here, the activation energy required for the proton transport in the membrane and the membrane protonic conductivity at a reference pressure and temperature are experimentally determined by Espinoza-López (2018).

$$
U_{\mathrm{ohm}} = R_{\mathrm{mem}} \cdot I \tag{4.13}
$$

$$R_{\text{mem}} = \frac{\delta_{\text{mem}}}{\sigma_{\text{mem}}} \tag{4.14}$$

$$\sigma_{\text{mem}} = \sigma_{\text{mem,SATP}} \cdot \exp\left(-\frac{E_{\text{pro}}}{R} \cdot \left(\frac{1}{T} - \frac{1}{T_{\text{SATP}}}\right)\right) \tag{4.15}$$

4.3.1.5 The concentration overvoltage

The concentration overvoltage results from mass transport limitations of reactants at the electrodes at high current densities. These transport limitations cause a decreasing electrolyzer performance due to blocking of active sites on the electrodes, increase in electrical resistance and limited water diffusion to the active sites (Olivier et al., 2017). However, current densities up to 3 $\text{A}\cdot\text{cm}^{-2}$ result in negligible mass transfer losses, therefore, these losses are not incorporated into this model (Yigit & Selamet, 2016; Espinosa-López et al., 2018).

4.3.2 Electrode chambers submodel

The electrode chambers submodel simulates the gas production, water consumption, gas flows through the membrane and the magnitude and concentration of the flow at various locations.

4.3.2.1 Reaction

Faraday's law states that the production rate of hydrogen in an electrolyzer cell equals the electron transfer rate, or in other words, the electrical current in the external circuit. Therefore, the hydrogen production rate per cell can be calculated using Eq. (4.16) (Ulleberg, 2003). A faradaic efficiency of 1 gives the maximum theoretical hydrogen production rate. The mass transfer rates of water and oxygen can be calculated using the stoichiometry of the overall reaction, as shown in Eq. (4.17).

$$\dot{n}_{\text{H}_2} = \eta_{\text{F}} \frac{I_{\text{c}}}{zF} \quad \text{(per cell)} \tag{4.16}$$

$$\dot{n}_{\text{H}_2\text{O}} = 2\dot{n}_{\text{H}_2} = \dot{n}_{\text{O}_2} \tag{4.17}$$

4.3.2.2 Membrane electrode assembly

This section is based on the work of Sartory et al. (2017). Gas transport through the membrane is incorporated as it influences the purity and efficiency of a PEME. Furthermore, it constraints operating conditions like limiting the pressure at the anode and cathode side and the difference between them. The following assumptions are made:

- The membrane permeability of both oxygen and hydrogen is assumed to be constant.
- It is assumed that the membrane interfaces and the anode and cathode channels do not have storage capacity using a 0D modeling approach.
- The anode channel is assumed to be fully filled with liquid water.
- It is assumed that only gasses can permeate through the electrodes (anode and cathode).

- When the electrolyzer is off, the gas flows through the membrane will stop instantaneously. Therefore, the hydrogen molar fraction at the anode side will be zero instantly. The same holds for the oxygen molar fraction at the cathode side.
- It is assumed that water cannot permeate through the membrane.

Figure 4.3 shows the mass balances of the MEA in which the flow rates of water, hydrogen and oxygen are incorporated.

These values are determined at the membrane-anode interface (MAI) and membrane-cathode interface (MCI), the anode and cathode channel and the anode and cathode outlet. The interface is where the gas flows come into contact with the catalyst which is the location where the reaction takes place. The gas flow entering the anode channel is instantly taken away by the forced liquid water flow towards the anode outlet where it flows into the anode gas separator. The gas flow entering the cathode channel is passively transported towards the outlet due to the pressure difference.

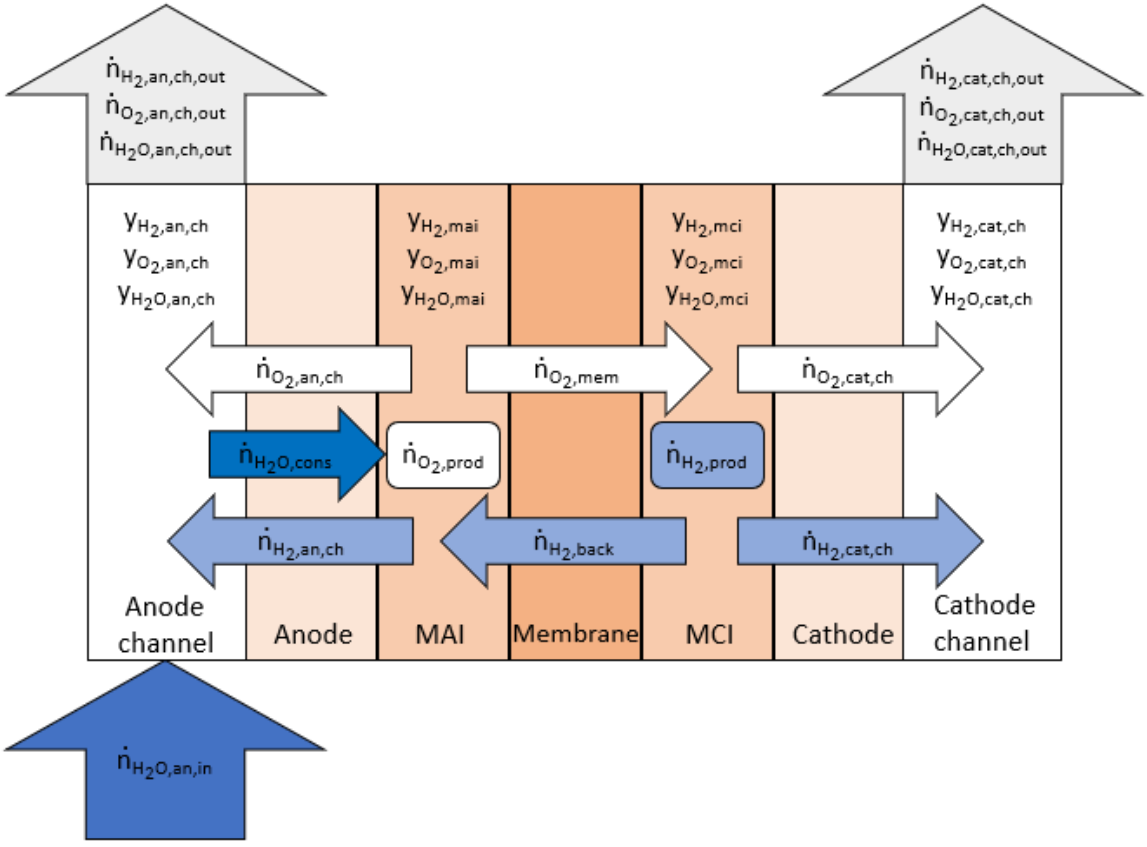

Figure 4.3: Schematic illustration of the various gas flows and molar fractions at different locations in the MEA and the electrode channels.

Membrane The membrane allows gas diffusion of hydrogen and oxygen called the hydrogen back flow and oxygen membrane flow, respectively. The magnitude of the oxygen membrane and hydrogen back flows are based on the membrane permeability of the gas, the geometry of the membrane and as a driving factor the difference between the partial pressures of the gas at the anode and cathode side, as shown in Eqs. (4.18) and (4.19), respectively (Sartory et al., 2017).

$$\dot{n}_{\mathrm{O_2,mem}} = P_{\mathrm{mem,O_2}} \cdot \frac{A_\mathrm{c} N_\mathrm{c}}{\delta_\mathrm{mem}} \cdot (p_\mathrm{an} y_{\mathrm{O_2,mai}} - p_\mathrm{cat} y_{\mathrm{O_2,mci}}) \tag{4.18}$$

$$\dot{n}_{\mathrm{H_2,back}} = P_{\mathrm{mem,H_2}} \cdot \frac{A_\mathrm{c} N_\mathrm{c}}{\delta_\mathrm{mem}} \cdot (p_\mathrm{cat} y_{\mathrm{H_2,mci}} - p_\mathrm{an} y_{\mathrm{H_2,mai}}) \tag{4.19}$$

Membrane interfaces The reactions take place at the membrane interfaces. The molar fractions at the membrane anode interface (MAI) and at the membrane cathode interface (MCI) are modeled using Eqs. (4.20) and (4.21), respectively, based on Dalton's Law (Sartory et al., 2017).

$$\begin{aligned} y_{\mathrm{H_2,mai}} &= \frac{\dot{n}_{\mathrm{H_2,back}}}{\dot{n}_{\mathrm{H_2,back}} + \dot{n}_{\mathrm{O_2,prod}}} \cdot (1 - y_{\mathrm{H_2O,mai}}) \\ y_{\mathrm{O_2,mai}} &= 1 - y_{\mathrm{H_2,mai}} - y_{\mathrm{H_2O}} \\ y_{\mathrm{H_2O,mai}} &= y_{\mathrm{H_2O,an,ch}} = \frac{p_{\mathrm{H_2O}}}{p_\mathrm{an}} \end{aligned} \tag{4.20}$$

$$\begin{aligned} y_{\mathrm{H_2,mci}} &= \frac{\dot{n}_{\mathrm{H_2,prod}}}{\dot{n}_{\mathrm{H_2,prod}} + \dot{n}_{\mathrm{O_2,mem}}} \cdot (1 - y_{\mathrm{H_2O,mci}}) \\ y_{\mathrm{O_2,mci}} &= 1 - y_{\mathrm{H_2,m,cat}} - y_{\mathrm{H_2O}} \\ y_{\mathrm{H_2O,mci}} &= y_{\mathrm{H_2O,cat,ch}} = \frac{p_{\mathrm{H_2O}}}{p_\mathrm{cat}} \end{aligned} \tag{4.21}$$

Anode channel The molar fractions and the mass balances for the anode channel are given by Eqs. (4.22, 4.23), respectively (Sartory et al., 2017).

$$\begin{aligned} y_{\mathrm{H_2,an,ch}} &= \frac{\dot{n}_{\mathrm{H_2,an,ch}}}{\dot{n}_{\mathrm{H_2,an,ch}} + \dot{n}_{\mathrm{O_2,an,ch}}} \cdot (1 - y_{\mathrm{H_2O,an,ch}}) \\ y_{\mathrm{O_2,an,ch}} &= 1 - y_{\mathrm{H_2,an,ch}} - y_{\mathrm{H_2O,an,ch}} \end{aligned} \tag{4.22}$$

$$\begin{aligned} \dot{n}_{\mathrm{H_2,an,ch}} - \dot{n}_{\mathrm{H_2,back}} &= 0 \\ \dot{n}_{\mathrm{O_2,an,ch}} - \dot{n}_{\mathrm{O_2,prod}} + \dot{n}_{\mathrm{O_2,mem}} &= 0 \end{aligned} \tag{4.23}$$

Cathode channel The molar fractions and the mass balances for the anode channel are given by Eqs. (4.24, 4.25), respectively (Sartory et al., 2017).

$$\begin{aligned} y_{\mathrm{H_2,cat,ch}} &= \frac{\dot{n}_{\mathrm{H_2,cat,ch}}}{\dot{n}_{\mathrm{H_2,cat,ch}} + \dot{n}_{\mathrm{O_2,mem}}} \cdot (1 - y_{\mathrm{H_2O,cat,ch}}) \\ y_{\mathrm{O_2,cat,ch}} &= 1 - y_{\mathrm{H_2,cat,ch}} - y_{\mathrm{H_2O,cat,ch}} \end{aligned} \tag{4.24}$$

Outlets No reactions or accumulation takes place at the channels, therefore, the gas flow composition at the channel outlet is equal to that of the channel itself.

$$\begin{aligned} \dot{n}_{\mathrm{H_2,ch,cat}} - \dot{n}_{\mathrm{H_2,prod}} + \dot{n}_{\mathrm{H_2,back}} &= 0 \\ \dot{n}_{\mathrm{O_2,mem}} - \dot{n}_{\mathrm{O_2,ch,cat}} &= 0 \end{aligned} \tag{4.25}$$

4.3.2.3 Gas separators

This submodel estimates the anode and cathode pressure and the composition of the gas flows leaving the leaving the electrolyzer.

- A well-stirred tank with uniform pressure, temperature and composition is assumed for both the anode and cathode side gas separators.
- The water content in the gas separator exerts a vapor pressure equal to the saturation pressure.
- The liquid water content does not take up storage space inside the gas separators.

Cathode gas separator mass balance The cathode gas separator (CGS) fills up until it reaches the desired operating pressure. When this pressure is reached, a controller will initiate an outlet flow with a gas composition equal to that of the gas separator itself. The density of the hydrogen in the CGS is modeled using Eq. (4.26). This density is used to calculate the hydrogen partial pressure with the real gas law.

$$\begin{gathered} \frac{V_{\mathrm{CGS}}}{M_{\mathrm{H_2}}} \cdot \frac{d}{dt} \rho_{\mathrm{H_2,CGS}} = \dot{n}_{\mathrm{H_2,cat,ch}} - \dot{n}_{\mathrm{H_2,CGS,out}} \\ \text{with} \qquad \dot{n}_{\mathrm{H_2,CGS,out}} = y_{\mathrm{H_2,CGS}} \cdot \dot{n}_{\mathrm{tot,CGS}} \end{gathered} \tag{4.26}$$

The outflow of the CGS is composed of hydrogen, oxygen and water vapor. Equation (4.27) and (4.28) are used to calculate the hydrogen and oxygen molar fractions at the CGS, respectively.

$$y_{\mathrm{H_2,CGS}} = \frac{n_{\mathrm{H_2,CGS}}}{n_{\mathrm{O_2,CGS}} + n_{\mathrm{H_2,CGS}}} (1 - y_{\mathrm{H_2O}}) \tag{4.27}$$

$$y_{\mathrm{O_2,CGS}} = 1 - n_{\mathrm{H_2,CGS}} - y_{\mathrm{H_2O}} \tag{4.28}$$

The initial conditions are given in Pascals. Therefore, the real gas law is used to convert the initial partial pressure into initial density of the component.

These molar fractions and the total CGS flow are used to find the molar flow per component. Consequently, the same procedure is used to find the values for the anode gas separator (AGS). The total pressure is the summation of the partial pressures of hydrogen, oxygen and water vapor, as shown in Eq. (4.29).

$$p_{\mathrm{H_2},i} + p_{\mathrm{O_2},i} + y_{\mathrm{H_2O}} = p_{\mathrm{tot},i} \qquad (i = \mathrm{CGS}, \mathrm{AGS}) \tag{4.29}$$

4.3.3 Thermal submodel

A lumped thermal capacitance model is assumed for the PEME. The control volume used for the PEME model consists of the electrolyzer stack, the circulating water loop, the CGS, the AGS and the circulation pump. This control volume is used to define the heat losses of the system to the environment. So, an overall thermal capacity is used which can be interpreted as the thermal capacitance of the circulating water loop which has an uniform temperature at all times (Espinosa-López et al., 2018). Figure 4.4 gives a schematic illustration of the PEME control volume with the several heat flows.

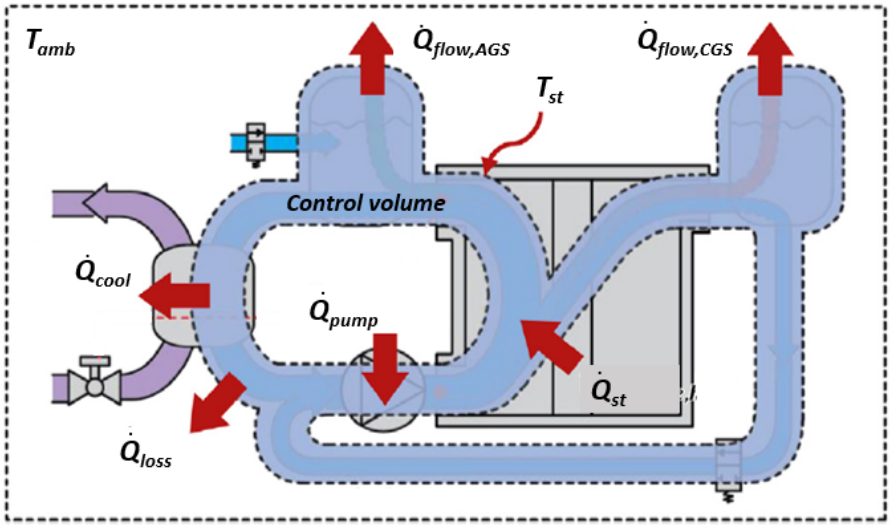

Figure 4.4: Schematic illustration of the PEME control volume used for the heat balance (Espinosa-López et al., 2018).

The balance shown in Eq. (4.30) consists of the overall thermal capacity factor, the heat generation due to voltage losses inside the stacks, heat generation by pump inefficiencies, heat removed by the heat exchanger, heat loss to the environment and sensible heat loss caused by the outgoing gas flows (Espinosa-López et al., 2018). The following assumptions have been made:

- The PEME has a overall lumped thermal heat capacity (Espinosa-López et al., 2018).
- The temperature is uniform throughout the control volume, so temperature gradients are neglected (Espinosa-López et al., 2018).
- An overall thermal heat resistance of the PEME is assumed (Espinosa-López et al., 2018).
- The heat exchanger is only able to cool down the system (Espinosa-López et al., 2018).
- Heat loss due to water evaporation and heat needed to warm up the water entering the system are neglected (Espinosa-López et al., 2018).

$$C_{\mathrm{th}} \frac{dT}{dt} = \dot{Q}_{\mathrm{st}} + \dot{Q}_{\mathrm{pump}} - \dot{Q}_{\mathrm{cool}} - \dot{Q}_{\mathrm{loss}} - \dot{Q}_{\mathrm{flow}} \tag{4.30}$$

The heat generated by the stack results from the difference between the cell voltage and the thermoneutral voltage and is calculated using Eq. (4.31). Here, the thermal-neutral voltage is a function

of the enthalpy change of reaction which in turn is a function of temperature and pressure. For this study, it is assumed that it is only a function of temperature and it will be calculated using REFPROP® , as shown in Eq. (4.32).

$$\dot{Q}_{\mathrm{st}} = I_{\mathrm{c}} \cdot N_{\mathrm{c}} \cdot N_{\mathrm{st}} \cdot (U_{\mathrm{c}} - U_{\text{th-n}}) \tag{4.31}$$

$$U_{\text{th-n}} = \frac{\Delta H_{\mathrm{R}}}{zF} \approx \frac{f(T)}{zF} \tag{4.32}$$

A pump is never 100% efficient due to friction losses These losses generate heat which is dissipated into the water flow. The magnitude of the heat generation by the pump is calculated using Eq. (4.33). The circulation pump will be further elaborated in section 4.3.4.

$$\dot{Q}_{\mathrm{pump}} = P_{\mathrm{pump,shaft}} - P_{\mathrm{pump,hydr}} \tag{4.33}$$

A cooling system is installed to regulate the water temperature to prevent overheating and to maintain the preferred operating temperature of the electrolyzer. During start-up, no cooling is needed as the reaction needs thermal energy. When the operating temperature is reached a controller regulates the operating temperature. The necessary cooling energy, is calculated by setting the left-hand-side of Eq. (4.30) equal to zero and rearrange it, as shown in Eq. (4.34).

$$\dot{Q}_{\mathrm{cool}} = \dot{Q}_{\mathrm{st}} + \dot{Q}_{\mathrm{pump}} - \dot{Q}_{\mathrm{loss}} - \dot{Q}_{\mathrm{flow}} \tag{4.34}$$

The heat loss to the environment is calculated using Eq. (4.35).

$$\dot{Q}_{\mathrm{loss}} = N_{\mathrm{st}} \cdot \frac{T_{\mathrm{st}} - T_{\mathrm{amb}}}{R_{\mathrm{th}}} \tag{4.35}$$

The last term of Eq. (4.30) represents the heat leaving the system with the gas flows which is calculated according to Eq. (4.36). The enthalpy and molar flux are modeled using REFPROP® and Faraday's Law (Eq. 4.16), respectively.

$$\dot{Q}_{\mathrm{flow}} = \sum_{i=1} \dot{n}_{\mathrm{i,AGS}} \cdot \mathrm{d}h_{\mathrm{i,AGS}} + \sum_{i=1} \dot{n}_{\mathrm{i,CGS}} \cdot \mathrm{d}h_{\mathrm{i,CGS}} \quad i = \mathrm{H_2}, \mathrm{O_2} \tag{4.36}$$

4.3.4 Water circulation pump

The pump is responsible for circulating the water through the anode channel. The first fraction of Eq. (4.37) gives the total water flow based on the consumed water at the anode.

$$P_{\text{pump,hydr}} = \frac{\dot{n}_{\text{w}}}{N_{\text{w}}} \cdot M_{\text{w}} g H_{\text{pump}}$$

$$P_{\text{pump,shaft}} = \frac{P_{\text{pump,hydr}}}{\eta_{\text{mech}}} \tag{4.37}$$

$$P_{\text{pump,el}} = \frac{P_{\text{pump,shaft}}}{\eta_{\text{el}}}$$

4.3.5 Heat exchanger

The heat exchanger (HEX) is responsible for taking away the excess heat of the PEME by using water as the refrigerant. For this, the sink also needs a circulation pump. The pump power depends largely on the sink mass flow which is calculated according to Eq. (4.38). The average sink specific heat capacity is calculated with REFPROP® using the average sink temperature and pressure. A constant pinch temperature (ΔT_{p}) which is the minimum temperature difference between the sink and source flow is assumed. Also, a constant sink temperature increase (ΔT_{sink}) is assumed. Theoretically, these assumptions result in a continuously changing heat transfer area or overall heat transfer coefficient of the HEX. The electrical power for the heat exchanger pump is calculated analogously to Eq. (4.37) by replacing $\frac{\dot{n}_{\text{w}}}{N_{\text{w}}}$ with $\dot{m}_{\text{hex,in}}$.

$$\dot{m}_{\text{hex,in}} = \frac{\dot{Q}_{\text{hex}}}{c_{p,\text{refrig}} \cdot \Delta T_{\text{sink}}} \qquad \text{with} \qquad \bar{T}_{\text{hex}} = T_{\text{st}} - \Delta T_{\text{p}} - 0.5 \cdot \Delta T_{\text{sink}} \tag{4.38}$$

4.3.6 DeOxo unit

The DeOxo unit is responsible for catalytically removing the oxygen from the flow. The model uses the following assumption:

- It is assumed that the DeOxo unit removes all oxygen from the flow.
- No hydrogen is lost.
- Pressure drop is neglected.

4.3.7 Condensate trap

The condensate trap removes the water vapor from the flow by lowering the temperature. The model uses the following assumption:

- It is assumed that condensate trap removes all water vapor from the flow.
- There is no pressure drop.
- No hydrogen is lost.

The heat that needs to be removed from the flow in order to cool the flow to the operating temperature of the condensate trap is calculated analogously to Eq. (4.38).

4.3.8 Total power

This submodel accounts for all the power that is needed for the PEME and models the various system efficiencies. The faradaic efficiency is the ratio between the usable hydrogen flow and the maximum theoretical flow, as shown in Eq. (4.40).

$$\begin{aligned} P_{\text{BoP}} &= P_{\text{circ-pump}} + P_{\text{hex-pump}} \\ P_{\text{PEME}} &= n_{\text{st}} \cdot P_{\text{st}} + P_{\text{BoP}} \end{aligned} \tag{4.39}$$

The various PEME efficiencies are modeled according to Eq. (4.40) to (4.44).

$$\eta_{\text{F}} = \frac{\dot{n}_{\text{H}_2,\text{cat,out}}}{\dot{n}_{\text{H}_2,\text{th}}} \qquad \text{(Faraday efficiency)} \tag{4.40}$$

$$\eta_{\text{st}} = \frac{\dot{n}_{\text{H}_2,\text{cat,out}} \cdot E_{\text{LHV}}}{n_{\text{st}} \cdot P_{\text{st}}} \qquad \text{(First law stack efficiency)} \tag{4.41}$$

$$\eta_{\text{el}} = \frac{n_{\text{st}} \cdot P_{\text{st}}}{P_{\text{PEME}}} \qquad \text{(Electrical efficiency)} \tag{4.42}$$

$$\eta_{\text{ee}} = \frac{U_{\text{th-n}}}{U_{\text{st}}} \qquad \text{(Electrical-energy efficiency)} \tag{4.43}$$

$$\eta_{\text{tot}} = \frac{\dot{n}_{\text{H}_2,\text{cat,out}} \cdot E_{\text{LHV}}}{P_{\text{PEME}}} \qquad \text{(Total efficiency)} \tag{4.44}$$

4.3.9 Exergy

Exergy is the maximum theoretical work that can be obtained from a system when the system comes into equilibrium with the environment, also known as the dead state. Whereas energy is always conserved, exergy can be destroyed by irreversibilities. Exergy can also be transferred from and to another system and when it is transferred to the environment it is typically called exergy destruction (Moran et al., 2010). Exergy destruction, in particular, is a good estimate to determine system losses.

Equation (4.45) gives an exergy balance for a system (Demirel, 2013).

$$\sum_{in} \left(1 - \frac{T_0}{T_{\text{in}}}\right) \dot{Q}_{\text{in}} + \dot{W}_{\text{in}} + \sum_{\text{in}} \dot{m} \cdot ex_{\text{f}} = \sum_{\text{out}} \left(1 - \frac{T_0}{T_{\text{out}}}\right) \dot{Q}_{\text{out}} + \dot{W}_{\text{out}} + \sum_{\text{out}} \dot{m} \cdot ex_{\text{f}} + \dot{E}x_{\text{d}} \tag{4.45}$$

An electrolyzer system does not produce any work. The system has a constant volume, so no volume work will be done. The work done on this system comes from the electrical energy input for the stacks and the power input for the circulation and HEX pumps. Furthermore, there will be no heat

input as the system can only cool itself down. The excess heat of the system is removed by the HEX with the temperature of the stack and heat is removed at the condensate trap. Therefore, after some rearrangements, Eq. (4.45) will become Eq. (4.46), giving the exergy destruction of the electrolyzer system.

$$\dot{E}x_d = \dot{W}_{\text{in}} - \sum_{\text{out}} \left(1 - \frac{T_0}{T_{\text{out}}}\right) \dot{Q}_{\text{out}} + \sum_{\text{in}} \dot{m} \cdot ex_{\text{f}} - \sum_{\text{out}} \dot{m} \cdot ex_{\text{f}} \tag{4.46}$$

$$\text{with} \quad \sum_{\text{out}} \left(1 - \frac{T_0}{T_{\text{out}}}\right) \dot{Q}_{\text{out}} = \left(1 - \frac{T_{\text{amb}}}{T_{\text{st}}}\right) \dot{Q}_{\text{cool}} + \left(1 - \frac{T_{\text{amb}}}{T_{\text{ct}}}\right) \dot{Q}_{\text{ct}} \qquad \text{and} \quad \dot{W}_{\text{in}} = \dot{P}_{\text{PEME}}$$

The flow exergy is modeled according to Eq. (4.47). The total flow exergy is made up of the thermo-mechanical and the chemical exergy. The first is the summation of the physical properties of the component, the kinetic exergy and the potential exergy. However, the kinetic and potential exergy are assumed to be small and are therefore neglected, as shown in Eq. (4.48). The chemical exergy of hydrogen only varies slightly with its lower heating value (Demirel, 2013). Therefore, the hydrogen chemical exergy[5] and the LHV[6] are assumed equal and constant for this study.

$$ex_{\text{f}} = ex_{\text{f,th-mech}} + ex_{\text{f,chem}} \tag{4.47}$$

$$ex_{\text{th-mech}} = (h - h_0) - T \cdot (s - s_0) + \frac{v^2}{2} + gz \approx (h - h_0) - T \cdot (s - s_0) \tag{4.48}$$

4.3.10 Sensitivity analysis of the PEM electrolyzer

Several simulation runs are done, given in Apx. L, using the model of this study which proved that PEMEs are more efficient at increased temperatures and lower pressures. These results where also found in literature (Espinosa-López et al., 2018; Toghyani et al., 2019; Sartory et al., 2017).

[5] Molar Chemical Exergy of hydrogen relative to a reference atmosphere at $p_0 = 100kPa, T_0 = 25°C$, and 60% relative humidity

[6] `https://h2tools.org/hyarc/calculator-tools/lower-and-higher-heating-values-fuels`

4.4 Pressure control modeling

In the following section the pressure control model will be elaborated. This section consists of the modeling approaches for a single stage reciprocating compressor, an isenthalpic throttling valve and an after-cooler.

4.4.1 Positive displacement compressors

The compression approach from Dixon & Hall (2013) is used for modeling the compressor.

- A constant isentropic compressor efficiency is assumed.
- Velocities at in- and outlet are the same.
- Steady-state operation is assumed.

Compression stage An one stage compressor process with after cooler is assumed. This cooler is used to cool the flow to its initial temperature. The isentropic compressor outlet temperature is calculated according to Eq. (4.49).

$$\frac{T_{2,\text{is}}}{T_1} = \left(\frac{p_2}{p_1}\right)^{\frac{\gamma-1}{\gamma}} \tag{4.49}$$

A constant isentropic efficiency is assumed, making it possible to use Eq. (4.50) to estimate to real outlet temperature by using the isentropic outlet and inlet temperatures.

$$\eta_{\text{is}} = \frac{T_{2,\text{is}} - T_1}{T_2 - T_1} \tag{4.50}$$

Power consumption The work done by the compressor is estimated using Eq. (4.51) (Saadat-Targhi et al., 2016). Here, the enthalpies are found with REFPROP® using the temperatures and pressures as inputs. The compressor power consumption can be estimates using Eq. 4.52.

$$W_{\text{comp}} = \dot{m} \cdot (h_{\text{out}} - h_{\text{in}}) \tag{4.51}$$

$$P_{\text{comp}} = \frac{W_{\text{comp}}}{\eta_{\text{mech}}} \tag{4.52}$$

4.4.2 Throttling valve

A throttling valve between two systems is needed when the outlet pressure of the gas flow must be lower than the inlet pressure. Isenthalpic expansion is assumed, so no energy will be extracted from the stream. Hydrogen has a negative Joule-Thompson coefficient, meaning that the pressure will increase during throttling processes (Winterbone & Turan, 2015). REFPROP® is used to determine the outlet temperature during throttling, as shown in Eq. (4.53).

$$\begin{aligned} h_{\text{in}} &= f(T_{\text{in}}, p_{\text{in}}) \\ T_{\text{out}} &= f(h_{\text{in}}, p_{\text{out}}) \end{aligned} \tag{4.53}$$

4.4.3 After-cooler

An after-cooler is used to cool the hydrogen flow back to the compressor or throttling valve inlet temperature. The power consumed by this cooler is not incorporated in the model. Equation (4.54) gives an estimation of the hydrogen enthalpy at the inlet and the outlet of the after-cooler as a function of the temperature and pressure using REFPROP® .

$$\begin{aligned} h_{\text{hex,in}} &= f(T_{\text{hex,in}}, p_{\text{hex}}) \\ h_{\text{hex,out}} &= f(T_{\text{hex,out}}, p_{\text{hex}}) \end{aligned} \tag{4.54}$$

The product of the mass flow and the enthalpy difference gives the necessary heat removal by the HEX, as shown in Eq. 4.55

$$\dot{Q}_{\text{hex}} = \dot{m} \cdot (h_{\text{hex,out}} - h_{\text{hex,in}}) \tag{4.55}$$

4.4.4 Pressure control exergy

The exergy balance for a single-stage compressor, a throttling valve and an after-cooler are elaborated in this section. The compressor does work on the system and the inlet and outlet mass flows are assumed equal due to the steady-state operation assumption. Furthermore, the adiabatic process assumption results in the lack of heat loss to the environment, so Eq. (4.45) becomes Eq. (4.56).

$$\dot{E}x_{\text{d}} = \dot{W}_{\text{comp}} + \dot{m} \cdot (ex_{\text{f,in}} - ex_{\text{f,out}}) = \dot{W}_{\text{comp}} + \dot{m} \cdot [(h_{\text{in}} - h_{\text{out}}) - T_0(s_{\text{in}} - s_{\text{out}})] \tag{4.56}$$

The equation can be further simplified by substituting Eq. (4.51) into Eq. (4.56), as shown in Eq. (4.57)

$$\dot{E}x_{\text{d}} = \dot{m} \cdot T_0(s_{\text{out}} - s_{\text{in}}) \tag{4.57}$$

The throttling process is assumed isenthalpic, therefore, the exergy destruction can be modeled using Eq. (4.58) which is equal to the compressor exergy equation.

$$\dot{E}x_{\text{d}} = \dot{m} \cdot T_0(s_{\text{out}} - s_{\text{in}}) \tag{4.58}$$

The exergy destruction of the after-cooler is modeled using Eq. (4.59).

$$\dot{E}x_{\text{d}} = \left(1 - \frac{T_{\text{amb}}}{T_{\text{hex,out}}}\right) \dot{Q}_{\text{hex}} + \dot{m} \cdot [(h_{\text{in}} - h_{\text{out}}) - T_0(s_{\text{in}} - s_{\text{out}})] \tag{4.59}$$

4.5 Salt cavern

The salt cavern will be used as the control volume of the whole system. The minimum and maximum allowable pressure of the the cavern determines whether hydrogen can be injected or discharged. The minimum cavern pressure is determined by the so-called cushion gas that is necessary to prevent the cavern from collapsing. Generally, this cushion gas is around 30% of the total storage capacity (Maton et al., 2013). At each time step, the thermodynamic properties like pressure, density and temperature inside the cavern are calculated depending on the mass and energy balances. The following assumptions have been made for the salt cavern:

- All properties inside the cavern are assumed to be uniform, comparable to a well-stirred tank. This is reasonable due to gas circulation inside the cavern as a result of natural convection (Maton et al., 2013).
- The salt cavern is modeled as a cylinder which is common for describing the shape of a salt cavern (Bérest, 2019).
- One-dimensional radial heat transfer is assumed based on natural convection and conduction resistances (Maton et al., 2013).
- Hydrogen leakage from auxiliary equipment is assumed negligible.
- Hydrogen leakage through the salt cavern walls is assumed negligible (Gabrielli et al., 2020).
- It is assumed that the salt cavern is made of salt rock without brine in the pores. This assumption is valid for caverns which are operational for longer periods with many completed charge and discharge cycles.
- Natural convective heat transfer between the gas and the internal rock is present.
- Hydrogen is assumed to be the only component present in the cavern.
- Gravitational effects are neglected. This assumption is reasonable due the the low density nature of hydrogen making potential energy changes negligible.
- Due to small temperature changes, slow dynamics and a small hydrogen heat capacity compared to the salt rock heat capacity, the heat penetration depth is assumed to be 1 metre. After that, the salt rock acts as a constant and uniform temperature reservoir.
- The cavern has a constant volume.
- Simultaneous injection and discharge are assumed possible.

Figure 4.5 show a schematic illustration of the salt cavern.

4.5.1 Continuity submodel

The density change rate depends on the difference between the injection and discharge flows (Ripepi, 2018).

$$V_{\text{cav}} \cdot \frac{d\rho_{\text{cav}}}{dt} = \dot{m}_{\text{in}} - \dot{m}_{\text{out}} \tag{4.60}$$

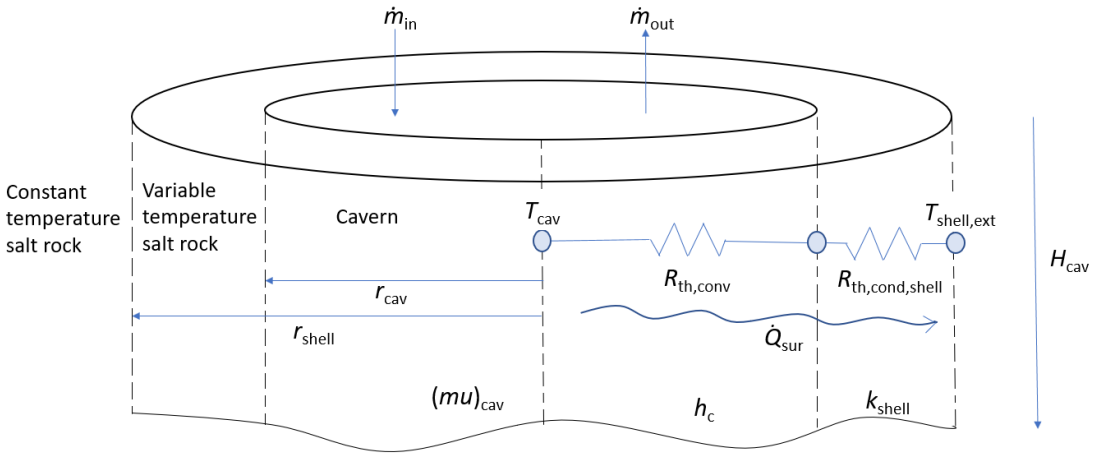

Figure 4.5: Schematic illustration of the salt cavern used for the mass and energy balances.

4.5.2 Energy balance submodel

The energy balance of Eq. (4.61) shows on the left side the change in thermal capacity of the salt cavern and on the right side the different heat flows. The first and second term on the right-side are the inlet and outlet heat flows, respectively. The last term is the heat exchange with the surroundings.

$$\frac{d(mu)_{\text{cav}}}{dt} = \dot{m}_{\text{in}}(h_{\text{in}} - h_{\text{cav}}) - \dot{m}_{\text{out}}(h_{\text{out}} - h_{\text{cav}}) - \dot{Q}_{\text{sur}} \tag{4.61}$$

This balance is used to determine the temperature inside the cavern by calculating the internal energy of the cavern which is shown in Eq. (4.62) (Moran et al., 2010).

$$u_{\text{cav}} = h_{\text{cav}} - p_{\text{cav}}v_{\text{cav}} = h_{\text{cav}} - \frac{p_{\text{cav}}}{\rho_{\text{cav}}} \tag{4.62}$$

As the enthalpy of the outlet flow and the cavern are the same, the first term on the right-hand-side cancels out in Eq. (4.61). The stored mass depends on time due to the inlet and outlet mass flows. The mass is the product of the density and the volume of the cavern. The volume is constant, so this can be taken out of the differential (Ripepi, 2018; Dooner & Wang, 2019). Lastly, substituting Eq. (4.62) into Eq. (4.61) will give Eq. (4.63) after some rearranging.

$$\begin{gathered} \rho_{\text{cav}}V_{\text{cav}}\frac{du_{\text{cav}}}{dt} = \dot{m}_{\text{in}}(h_{\text{in}} - h_{\text{cav}}) - \dot{Q}_{\text{sur}} \\ \text{with} \qquad \frac{du_{\text{cav}}}{dt} = \frac{dh_{\text{cav}}}{dt} - \frac{1}{\rho_{\text{cav}}}\frac{dp_{\text{cav}}}{dt} \end{gathered} \tag{4.63}$$

The heat exchange with the surrounding salt rock is calculated according to Eqs. (4.64) and (4.65) (Ripepi, 2018).

$$\dot{Q}_{\text{sur}} = \frac{T_{\text{cav}} - T_{\text{shell,ext}}}{R_{\text{th,tot}}} \tag{4.64}$$

$$
\begin{aligned}
R_{\mathrm{th,tot}} &= R_{\mathrm{th,conv}} + R_{\mathrm{th,cond,shell}} \\
R_{\mathrm{th,conv}} &= \frac{1}{h_{\mathrm{c}} \cdot 2\pi r_{\mathrm{cav}} H_{\mathrm{cav}}} \\
R_{\mathrm{th,cond,shell}} &= \ln\frac{r_{\mathrm{shell,ext}}}{r_{\mathrm{shell,int}}} \cdot \frac{1}{k_{\mathrm{shell}} \cdot 2\pi H_{\mathrm{cav}}}
\end{aligned}
\tag{4.65}
$$

The temperature can now be calculated using REFPROP® with the internal energy and the density as the inputs.

$$
T_{\mathrm{cav}} = f(u_{\mathrm{cav}}, \rho_{\mathrm{cav}}) \tag{4.66}
$$

4.5.3 Cavern pressure submodel

At low pressure, the compressibility factor of all gasses reach unity. However, the system compresses the hydrogen to high pressures which will influence the compressibility factor. For this study, REFPROP® in combination with the real gas law will be used, as shown in Eq. 4.67 and 4.68, respectively. For Z = 1, Eq. (4.68) will become the ideal gas law.

$$
Z_{\mathrm{cav}} = f(\rho_{\mathrm{cav}}, T_{\mathrm{cav}}) \tag{4.67}
$$

$$
p_{\mathrm{cav}} = Z_{\mathrm{cav}} \rho_{\mathrm{cav}} \bar{R}_{\mathrm{cav}} T_{\mathrm{cav}} \tag{4.68}
$$

4.5.4 Storage submodel

This submodel calculates the stored mass and chemical energy at each time instant using Eq. (4.69) and (4.70), respectively.

$$
m_{\mathrm{cav}} = \rho_{\mathrm{cav}} \cdot V_{\mathrm{cav}} \tag{4.69}
$$

$$
E_{\mathrm{chem,cav}} = m_{\mathrm{cav}} \cdot E_{\mathrm{LHV}_{\mathrm{H_2}}} \tag{4.70}
$$

4.5.5 Storage exergy

The volume of the cavern does not change and the kinetic and potential energy are neglected. Therefore the total storage exergy in the salt cavern is written according to Eq. (4.71).

$$
\begin{aligned}
&Ex_{\mathrm{cav}} = (U - U_0) + p_0(V - V_0) - T_0(S - S_0) + E_{\mathrm{kin}} + E_{\mathrm{pot}} + E_{\mathrm{chem}} \quad \rightarrow \\
&Ex_{\mathrm{cav}} = (U - U_0) - T_0(S - S_0) + E_{\mathrm{chem}}
\end{aligned}
\tag{4.71}
$$

4.6 Pipelines

Gaseous hydrogen will be transported through pipelines. As the connecting pipelines between the hydrogen storage system components can be tenths to hundredths of kilometres long, it can take a significant amount of time before steady-state conditions are reached. This is due to the fact that gasses are compressible (White, 2003). So, when a certain quantity of mass enters the pipeline it will not instantly exit the pipe outlet with the same quantity. Therefore, the transient behaviour of the gas flow plays an important role in the system.

4.6.1 1D compressible isothermal pipe flow

The flow of a one-dimensional, compressible and viscous heat conducting fluid can be described by averaging the three-dimensional equations for mass, momentum and energy conservation across the pipe (Helgaker, 2013). The energy equation, however, is neglected as isothermal pipe flow is assumed. This assumption is substantiated by the fact that the gas flow is cooled to the environment temperature before entering the pipe. Moreover, one-dimensional flow is assumed, as the pipe length is multiple orders of magnitude larger than the pipe diameter (Helgaker, 2013), therefore, the axial flow is the dominant flow. The flow resistance caused by friction with the pipe walls is incorporated using a friction factor. These assumptions simplify the computation of the flow dynamics. The resulting governing equations for this type of flow are given in Eq. (4.72) and (4.73).

$$\frac{\partial \rho}{\partial t} + \frac{\partial \rho v}{\partial x} = 0 \qquad \text{(Continuity)} \tag{4.72}$$

$$\frac{\partial \rho v}{\partial t} + \frac{\partial p}{\partial x} + \frac{\partial \rho v^2}{\partial x} = -\frac{f \rho |v| v}{2D} - \rho g \sin\theta \qquad \text{(Momentum)} \tag{4.73}$$

The above equations state that mass and momentum must be conserved for the system to be real. The third term on the left-hand side of the momentum equation is the convective term which describes the change of the gas properties due to movement of the fluid. The two terms on the right-hand side of the momentum equation are the friction and gravity term, respectively. Meaning, the density and velocity of the fluid are influenced by friction with the pipe wall and by the height differences along the pipe. Besides the isothermal and 1D flow assumptions, several other assumptions are made to further simplify the equations which are all listed below.

- 1D flow: It is assumed that the flow has only one direction being the axial direction. So, no flow in the radial direction.
- Isothermal flow: Flow temperature stays constant in space and time due to heat exchange with the surroundings. This is justified as operational data of a 48 kilometer on-shore natural gas pipeline operated by *Gassco* only shows a temperature difference of 3°C between the inlet and outlet (Helgaker, 2013). Furthermore, this study will use a gas inlet temperature equal to the ground temperature, minimizing heat transfer. Lastly, hydrogen has a relatively small Joule-Thomson coefficient of approximately 0.3 °C·MPa^{-1}. So, the temperature change due pressure drop along the pipeline is negligible.
- Horizontal straight pipe flow: The transportation pipe angle with the ground is zero and there are no bends in the pipe. However, the injection and discharge pipelines are vertical pipes, so in these cases gravity does play a role.

- Constant pipe diameter.
- Negligible convective term: Rewriting the convective term of Eq. (4.73) gives $\frac{\partial p}{\partial x}\frac{u^2}{c^2}$. For hydrogen pipelines, the gas velocity is significantly smaller than the speed of sound, resulting in a negligible contribution of the convective term.

After applying all the assumptions to Eqs. (4.72) and (4.73), the flow equations can be rewritten, as shown in Eqs. (4.74) and (4.75).

$$\frac{\partial \rho}{\partial t} + \frac{\partial \rho v}{\partial x} = 0 \qquad \text{(Continuity)} \tag{4.74}$$

$$\frac{\partial \rho v}{\partial t} + \frac{p}{\partial x} = -\frac{f \rho |v| v}{2D} \qquad \text{(Momentum)} \tag{4.75}$$

The real gas law, shown in Eq. (4.68), is needed to solve the conservation equations. This equation describes how the state variables are related to each other in which the compressibility factor is a function of the pressure and temperature of the fluid. Furthermore, a relation between the mass flow rate and the velocity must be incorporated, shown in Eq. (4.76).

$$\dot{m} = \rho v A \tag{4.76}$$

The flow equations can be rewritten, by using the definition for the speed of sound from Eq. (4.77) with Eq. (4.76) and (4.68), into Eq. (4.78-4.79).

$$Z \bar{R} T = \frac{p}{\rho} = c^2 \tag{4.77}$$

$$\frac{\partial p}{\partial t} + \frac{c^2}{A}\frac{\partial \dot{m}}{\partial x} = 0 \qquad \text{(Continuity)} \tag{4.78}$$

$$\frac{1}{A}\frac{\partial \dot{m}}{\partial t} + \frac{\partial p}{\partial x} = -\frac{f c^2 \dot{m} |\dot{m}|}{2DA^2 p} \qquad \text{(Momentum)} \tag{4.79}$$

4.6.1.1 Friction factor

The friction factor is a dimensionless factor which links the losses due to friction between the inner pipe wall and the fluid. The friction factor is highly dependent on the Reynolds number and thus the velocity of the fluid. The three relevant flow types in rough conduits are given below.

- Laminar flow: Re = 0 - 2300
- Transitional flow: Re = 2300 - 4000
- Fully turbulent flow: Re > 4000

The fluid flow in pipelines connected to intermittent sources and services will be zero at certain time instants and more than zero at other time instants, meaning that all three flow types will be present, resulting in varying friction factors along the pipe at each instant. The Reynolds number can be rewritten in other terms as shown in Eq. (4.80), making it dependent on the mass flow and the dynamic viscosity.

$$Re = \frac{\rho u D}{\mu} = \frac{4}{\pi D} \frac{\dot{m}(x,t)}{\mu(T)} \tag{4.80}$$

Figure 4.6. shows that the pressure only has a small influence on the dynamic viscosity. Taking the dynamic viscosity at 10°C and using typical pipeline values, the dynamic viscosity only decreases by 1.2% going from 100 to 60 bar. Furthermore, isothermal pipe flow is assumed, so the temperature of the gas will not change. Therefore, the dynamic viscosity is almost constant in space and time. Therefore, the Reynolds number is mainly influenced by the mass flow.

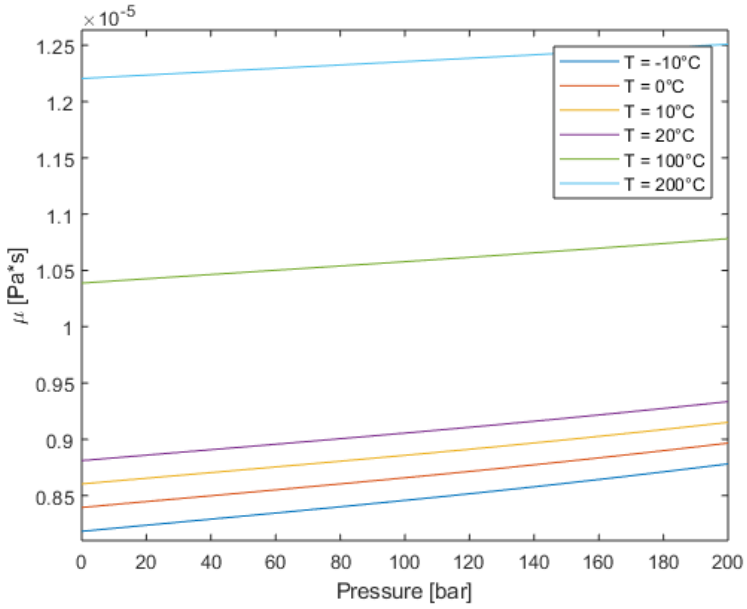

Figure 4.6: Influence of temperature and pressure on the dynamic viscosity of hydrogen.

Table 4.1 shows the Reynolds numbers for a low range of mass flows. Here, the pipe diameter is 0.2 meters and the dynamic viscosity is taken at 75 bar and 10°C This shows that already at low mass flows the fluid is in the fully turbulent regime. Therefore, correlations relating the Reynolds number and the friction factor can be used which are only valid for this flow regime.

Table 4.1: Reynolds number at various mass flows.

Parameter	Value					Unit
Mass flow	0.01	0.02	0.03	0.04	0.05	$kg{\cdot}s^{-1}$
Reynolds number	7,241	14,448	21,722	28,962	36,203	[-]

As the friction factor cannot be determined exactly for turbulent flows, a correlation is used based on empirical data (Helgaker, 2013). The Colebrook-White correlation is widely used and accepted for determining Darcy's friction factor of pipes (Colebrook & White, 1937). This equation correlates the friction factor to the pipe relative roughness and the Reynolds number of the fluid. However, this equation is implicit and needs iteration to find the correct values. Therefore, the Haalands relation, which is explicit, will be used (Haaland, 1983), as shown in Eq. (4.81). The friction factor for $0 < \mathrm{Re} < 4000$ will be set to the value calculated for $\mathrm{Re} = 4000$.

$$\frac{1}{\sqrt{f}} = -1.8 \log\left(\frac{\epsilon}{3.7D}^{1.11} + \frac{6.9}{Re}\right) \qquad \text{for} \quad Re \geq 4000 \tag{4.81}$$

4.6.2 Numerical methods

The governing equations are a system of hyperbolic partial differential equations. These equation are solved by using a suitable numerical approach. There are four methods, namely the method of characteristics and the finite volume, finite difference and finite element methods. Literature shows that the method of characteristics is slow, difficult to implement and bound to small time steps and that the finite element method is computationally demanding for pipe flows (Helgaker, 2013). Finite difference methods, however, are commonly used for one-dimensional compressible pipe flows. Here, the governing equations are converted to the algebraic form in discrete time and space. The values are calculated for each node at each time step. Discretization can be done either implicitly or explicitly in time. The former is the easier method, but is limited to small time steps due to the instability of the solution. This solution is, therefore, bound by the Courant-Friedrich-Lewy (CFL) condition which is shown in Eq. (4.82).

$$(|v| + c)\frac{\Delta t}{\Delta x} \leq 1 \tag{4.82}$$

The latter is more complex, but is unconditionally stable despite the size of the temporal and spatial steps which is beneficial for long, high pressure pipelines (Helgaker, 2013).

Several methods can be used to discretize time for implicit finite difference methods, like the backward Euler, Newton-Rhapson and the cell centered method. The backward Euler method is simple and approximates the spatial derivatives either by upwind or centered differences. the Newton-Rhapson method can solve a system of non-linear equations, but this is computationally intensive for complex networks and long pipelines. The cell centered method solves the partial derivatives for each pipe section instead of the pipe nodes. The cell centered method will be used as the discretization errors are lowest, it is unconditionally stable and the boundary conditions are easy to handle (Helgaker, 2013).

4.6.2.1 Cell centered linear implicit finite difference method

A cell centered linear implicit finite difference method is used. This method is first order correct in time and second order correct in space. The temporal and spatial derivatives and individual terms of the flow parameters are estimated using Eqs. (4.83) - (4.84).

$$\frac{\partial Y(x_I, t_{n+1})}{\partial t} = \frac{Y(x_{n+1}, t_{i+1}) + Y(x_n, t_{i+1}) - [Y(x_{n+1}, t_i) + Y(x_n, t_i)]}{2\partial t} + \mathcal{O}(\partial t) \tag{4.83}$$

$$\frac{\partial Y(x_I, t_{n+1})}{\partial x} = \frac{Y(x_{n+1}, t_{i+1}) - Y(x_n, t_{i+1})}{\partial x} + \mathcal{O}(\partial x^2) \tag{4.84}$$

$$Y(x_I, t_{n+1}) = \frac{Y(x_{n+1}, t_{i+1}) + Y(x_n, t_{i+1})}{2} + \mathcal{O}(\partial x^2) \tag{4.85}$$

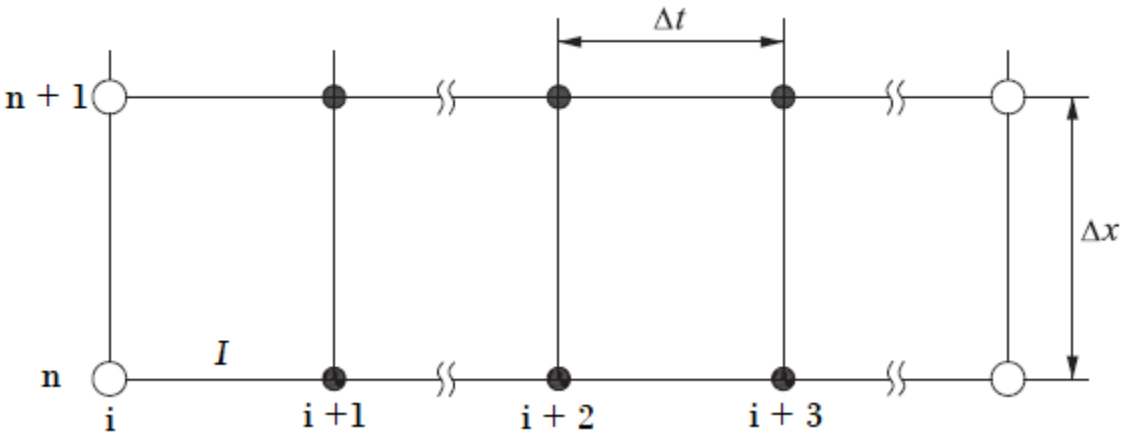

Figure 4.7: Grid used for the numerical method.

Equations with non-linear terms cannot be solved using the chosen numerical method. Therefore, the non-linear friction term, is linearized about the previous time step by using a first order Taylor expansion, as shown in Eq. (4.86) (Helgaker, 2013). Here, the Y-variable is the mass flow from the friction term of Eq. (4.79).

$$Y(x_I, t_{i+1}) = Y(x_I, t_i) + (t_{i+1} - t_i) \cdot \frac{\partial Y(x_I, t_i)}{\partial t} + \mathcal{O}(\partial t^2) \tag{4.86}$$

By implementing the equation for the friction term and Eqs. (4.83) and (4.85) into Eq. (4.86), the non-linear friction term can be developed into the following linearized approximation:

$$\frac{K}{A}\frac{\dot{m}(x_I, t_{i+1})^2}{p(x_I, t_{i+1})} \approx K\frac{\dot{m}(x_{n+1}, t_i) + \dot{m}(x_n, t_i)}{p(x_{n+1}, t_i) + p(x_n, t_i)} \left(\dot{m}(x_{n+1}, t_{i+1}) + \dot{m}(x_n, t_{i+1}) - \frac{\dot{m}(x_{n+1}, t_i) + \dot{m}(x_n, t_i)}{2} \right)$$

$$\text{with} \qquad K = \frac{c^2(x_I, t_i) \cdot f(x_I, t_i)}{2DA} \tag{4.87}$$

Now, the governing equations for mass and momentum form a system of linear equations, shown in Eqs. (4.88) and (4.89). The linearized equations can be numerically solved using an iterative process.

(Continuity)

$$\frac{p(x_{n+1},t_{i+1})+p(x_n,t_{i+1})-[p(x_{n+1},t_i)+p(x_n,t_i)]}{2\partial t}+\frac{c^2}{A}\cdot\frac{\dot{m}(x_{n+1},t_{i+1})-\dot{m}(x_n,t_{i+1})}{\partial x}=0 \tag{4.88}$$

(Momentum)

$$\frac{1}{A}\cdot\frac{\dot{m}(x_{n+1},t_{i+1})+\dot{m}(x_n,t_{i+1})-[\dot{m}(x_{n+1},t_i)+\dot{m}(x_n,t_i)]}{2\Delta t}+\frac{p(x_{n+1},t_{i+1})-p(x_n,t_{i+1})}{\Delta x}= \tag{4.89}$$

$$-\frac{K}{A}\cdot\frac{\dot{m}(x_{n+1},t_i)+\dot{m}(x_n,t_i)}{p(x_{n+1},t_i)+p(x_n,t_i)}\left(\dot{m}(x_{n+1},t_{i+1})+\dot{m}(x_n,t_{i+1})-\frac{\dot{m}(x_{n+1},t_i)+\dot{m}(x_n,t_i)}{2}\right)$$

4.6.3 Pipeline exergy

The total exergy destruction due to the pipe flow is calculated according to (4.45). Here, the potential energy is neglected, but the kinetic energy is taken into account as this can play a significant role in long pipelines with large pressure drops. Lastly, isothermal pipe flow is assumed, so there will be no heat flow and no work is done on or done by the system. The resulting exergy destruction balance is shown in Eq. (4.90).

$$\dot{E}x_d=\dot{m}_{\text{in}}\cdot ex_{\text{f,in}}-\dot{m}_{\text{out}}\cdot ex_{\text{f,out}}\qquad\text{with}\qquad ex_{\text{f}}=(h-h_0)-T_0(s-s_0)+\frac{v^2}{2} \tag{4.90}$$

4.6.4 Sensitivity analysis of pipeline model

Four parameters determining the pipe flow are analysed, being the pipe length, diameter, pressure and temperature. The sensitivity analysis of the pipe flow model can be found in Apx. M. The results showed that longer pipelines, smaller pipe diameters, low pressure pipes and higher flow temperatures all result in more pressure losses along the pipeline. Here, the pipe diameter has the biggest influence on the pressure drop.

Chapter 5

Validation of the model

The following chapter gives the validation of the electrolyzer and the pipeline models. The cavern model is not validated as the pressure results from a simple mass balance and the temperature fluctuation is minimal during operation due to the low Joule-Thompson coefficient and the low heat exchange with the surrounding walls.

5.1 PEM electrolyzer

The PEME is validated using the experimental data of Espinosa-López et al. (2018). Polarization curves show the connection between the input current density and the output cell voltage. These curves are influenced by the operating temperature and pressure. The polarization curves for this study are created by running the electrolyzer model under steady-state conditions, meaning that the operating temperature and pressure do not change in time. Furthermore, the membrane is assumed to be impenetrable to the present gasses. Therefore, only hydrogen will be present at the cathode and only oxygen at the anode. However, the vapor pressure does influence the partial pressures at both electrodes. The sole input parameter is the current density which increases from 0.0 to 2.0 A/cm^2 with 0.01 A/cm^2 increments. The results are shown in Fig. 5.1, showing a good match.

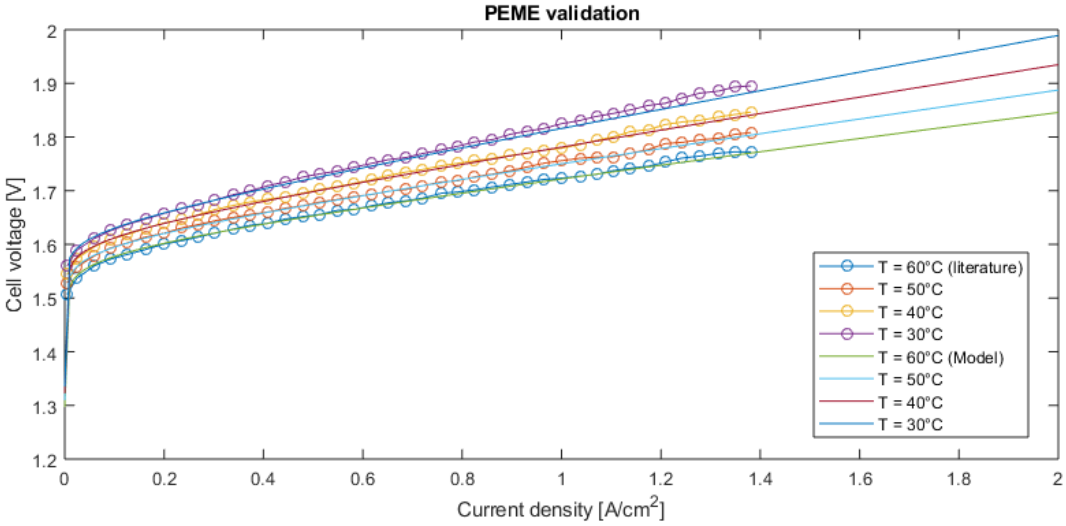

Figure 5.1: Validation of the PEME cell voltage at various temperatures and current densities. Lines: Literature values, Circles: This model. The cathode and anode pressures were 35 and 34 bar.

The dynamic behaviour of the electrolyzer is also validated with experimental data from Espinosa-López et al. (2018). In this case, the membrane is still impenetrable and the pressure is kept constant. The simulation results and the experimental data are plotted in Fig. 5.2, showing a good match with the experiments. The wave pattern of the experimental data is due to periodic re-circulation of cooled-down water into the PEME.

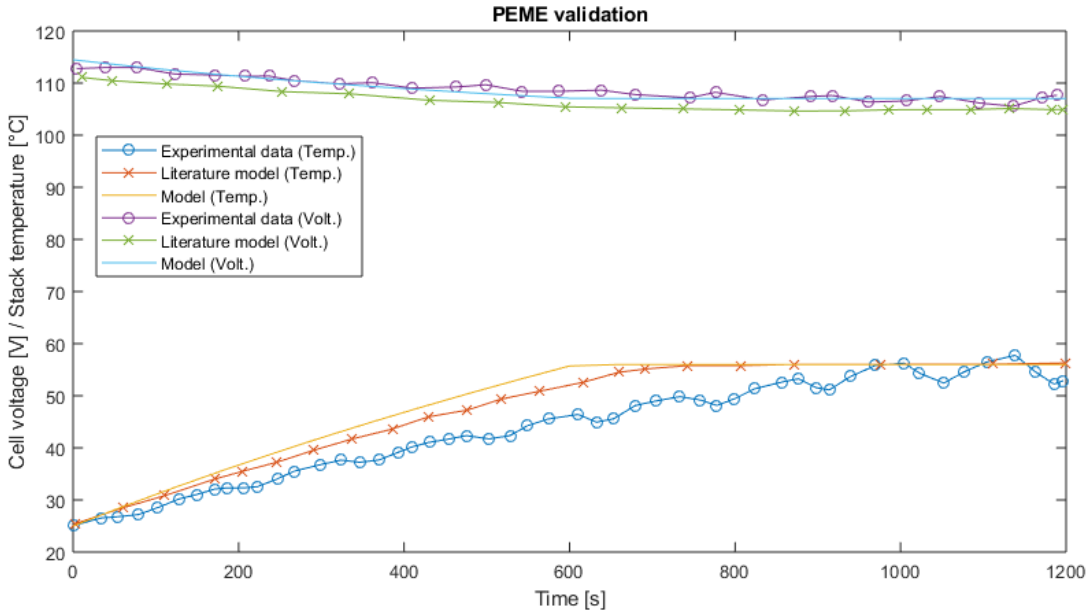

Figure 5.2: Validation of the transient behaviour of the cell voltage and stack temperature. The ambient and operating temperature were set to 25°C and 56°C, respectively. The cathode and anode pressure were 35 and 34 bar, respectively. The current density was set to 1.39 $A \cdot cm^{-2}$.

The validations are sufficient for guaranteeing realistic simulation results for the stated model assumptions. Membrane crossover was not validated as no experimental data was found in literature (Espinosa-López et al., 2018).

5.2 Pipeline

Two important factors of the pipe flow are the pressure drop due to friction and the duration of the transient phase before reaching steady state conditions. As there is limited data available for hydrogen pipelines, experimental data of methane pipelines is used.

5.2.1 Methane pipeline

The test case and simulation results from Helgaker (2013) are used to determine whether the pipeline model is correctly implemented. This case simulates 2 days of operation where the outlet mass flow of a 48 kilometres pipeline is varied from 300 to 400 to 200 and finally 300 $kg \cdot s^{-1}$. Each mass flow lasts for 6 hours. The input values used for the model are given in Table 5.1.

The the mass flow and pressure of the simulation results of Helgaker (2013) and from this study are shown in Figs. 5.3 and 5.4, respectively. The results show an excellent match. So, it can be concluded that the model is correctly implemented for continuous mass flows.

Table 5.1: Input parameters for the pipeline model used for validation.

Parameter	Value	Unit
Pipe length	48000	m
Discretization length	4000	m
Pipe diameter	1.016	m
Time step	10	s
Pipe roughness	$1.5e^{-6}$	m
Pipe friction factor	0.0075	-
Speed of sound (methane)	380	m/s

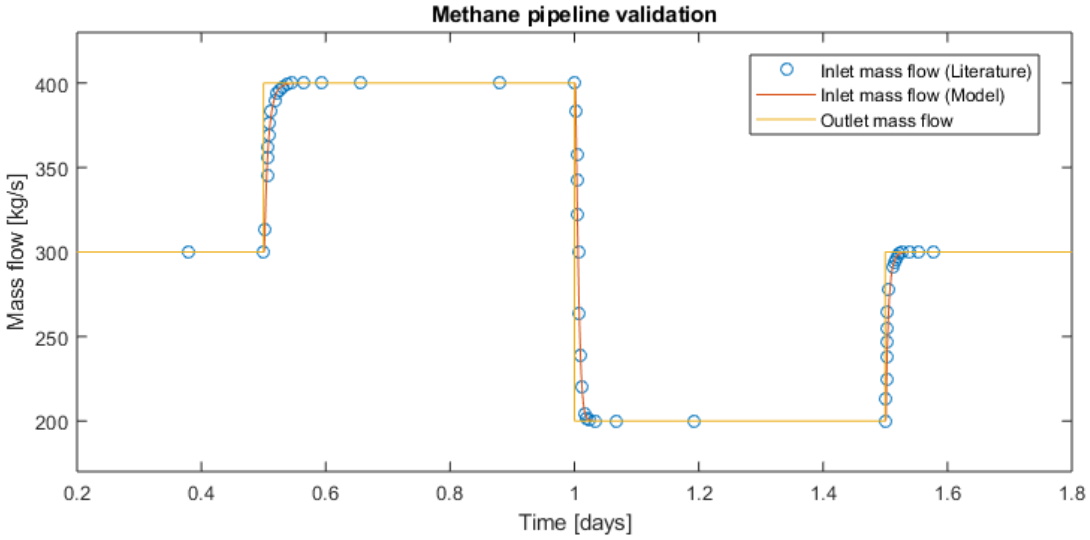

Figure 5.3: Validation of the pipe mass flow.

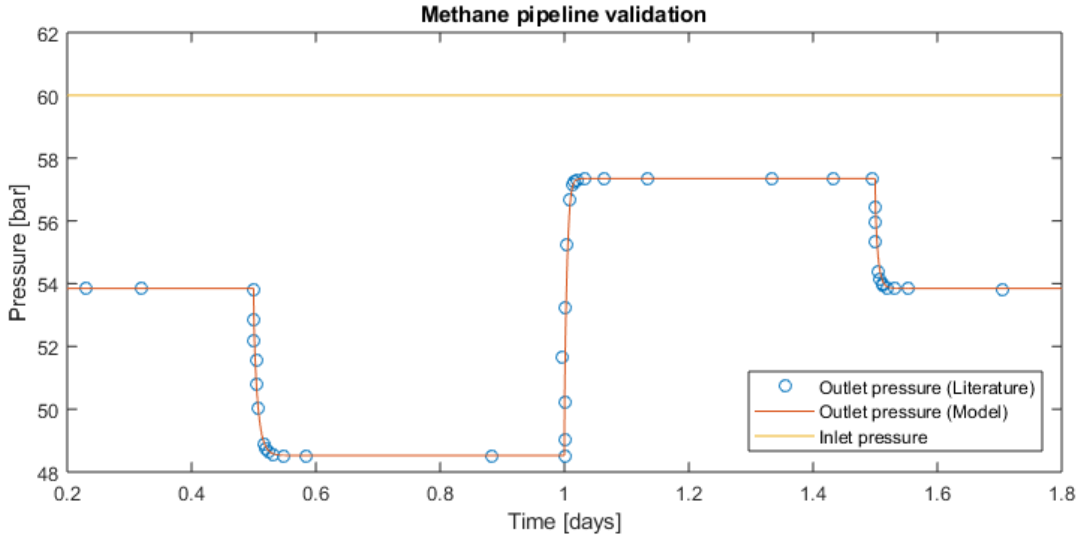

Figure 5.4: Validation of the pipe pressure.

Chapter 6

Intermittent pipe flow

The start-up and shut-down of the pipe flow is important for this study as the pipelines are connected to intermittent hydrogen production and consumption systems. This section shows the effect of sudden opening and closing of valves. Furthermore, an algorithm is implemented which prevents oscillating flow along the pipe as this is not a realistic phenomenon under normal pipe operation.

The linearization of the friction term in Eq. (4.75) is only valid for mass flows greater than zero (Luskin, 1979). Meaning, the friction only works in one direction, being from the outlet to the inlet of the pipeline. So, when the mass flow at a certain location along the pipe drops below zero, the friction factor should be negative in order to dampen the flow. This effect was proven by a test case given in Apx. K. However, during real pipeline operation the mass flow will never be negative at either end of the pipe. Therefore, the pipe model is adjusted to prevent negative mass flows, which is elaborated in section 6.1.2.

6.1 Hydrogen pipeline

The main differences between methane and hydrogen properties, which influence the flow, are the molar mass and the dynamic viscosity. These parameters influence the speed of sound and the Reynolds number, respectively. Under identical conditions[1], the speed of sound of hydrogen is approximately 3.2 times larger than that of methane. The Reynolds number, under identical conditions[1], is approximately 1.49 times the value of methane, resulting in a lower friction factor for hydrogen. However, the speed of sound has much more influence on the friction losses, therefore, relatively more friction losses occur for hydrogen flow.

To compare the performance results of a hydrogen pipeline with a methane pipeline, the total chemical energy content of the flow will be kept approximately equal, according to Eq. (6.1). As the LHV of hydrogen is higher, a lower mass flow is used. Here, it must be noted that the hydrogen flow velocity will be approximately 4.2 times faster under identical conditions[1] due to its low density.

$$E_{\mathrm{LHV}_{\mathrm{H_2}}} \cdot \dot{m}_{\mathrm{H_2},in} = E_{\mathrm{LHV}_{\mathrm{CH_4},in}} \cdot \dot{m}_{\mathrm{CH_4}} \tag{6.1}$$

When maintaining the same discretization values as for the methane pipeline, the CFL number will become higher than 1 due to the higher speed of sound. However, this is not a problem as the used numerical method is unconditionally stable (Helgaker, 2013).

[1] p = 90 bar, T = 10°C and $\dot{m}$ = 1 kg·s^{-1}

6.1.1 Grid-dependency study

The pipelines are discretized in space and time which lead to certain errors. Analogous with Helgaker (2013), a numerical result computed with a very fine grid is assumed to be the exact solution. In practice, the computational time for such a fine grid will be too long. Therefore, several simulations are done with different temporal and spatial steps, while keeping the CFL number (Eq. 4.82) at 0.95, to determine the relative errors between the exact solution and the coarser grids. The temporal and spatial steps are summarized in Table 6.1.

Table 6.1: Temporal and spatial steps for simulation runs with CFL = 0.95, the number of calculated data points and the time needed to simulate 30 minutes are given.

Run	1	2	3	4	5	6	7	8
dt [s]	0.3125	1	2.5	5	10	20	40	60
dx [m]	125	400	1000	2000	4000	8000	16000	24000
Pipe nodes [-]	385	121	49	25	13	7	4	3
Data points (30 minute run) [-]	2,216,600	217,800	34,560	9,000	2,340	630	180	90
Simulation time [s]	1929.173	94.914	12.792	4.816	1.991	0.906	0.526	0.371

A numerical case with different mass flow conditions is used to determine the accuracy of the different grids. Fast transient conditions are used for the output mass flow, meaning that the outlet mass flow follows step changes or in other words instant changes. The simulations started with a zero mass flow followed by a specific flow profile and ending with a zero mass flow again.

Figure 6.1 shows the results of the simulations. The plot clearly illustrates that steady-state conditions are reached at almost the same time for all runs. Especially, after the second and third outlet mass flow step change, when there is a continuous mass flow, the results are almost identical. However, at the start of the simulation and after the last step change there are significant differences of which the former becomes more clear in Fig. 6.2. Here, the five finest grids (run 1 - run 5) show relatively equal results, but the three courser grids show different results. The point where the finer grids cross is around t = 43.5 s. This, not coincidentally, is the time it takes for the pressure (acoustic) wave, caused by instantaneously opening the valve at the pipe end, to reach the other end of the pipe, according to $t = \frac{L}{c} = \frac{48000}{1100.4} = 43.62$s. The sudden rise of the inlet mass flow occurs due to the pressure wave which initiates the bulk mass flow along the pipe. After around 43.5 seconds, as the friction losses start to influence the bulk mass flow, the flow acceleration decreases. The time steps of the two coarser grids are close to or greater than 43.5 seconds and are, therefore, not able to capture this effect.

The figures show that the inlet mass flow starts to oscillate after sudden closing of the outlet valve at t = 10,800 s. This is caused by the fact that, at this stage, the pipe flow is modeled using a constant inlet pressure which is also depicted in Fig. 6.3. The oscillations are also occurring in the outlet pressure profile. However, the final pipe flow model will incorporate an algorithm which prevent this oscillating behaviour.

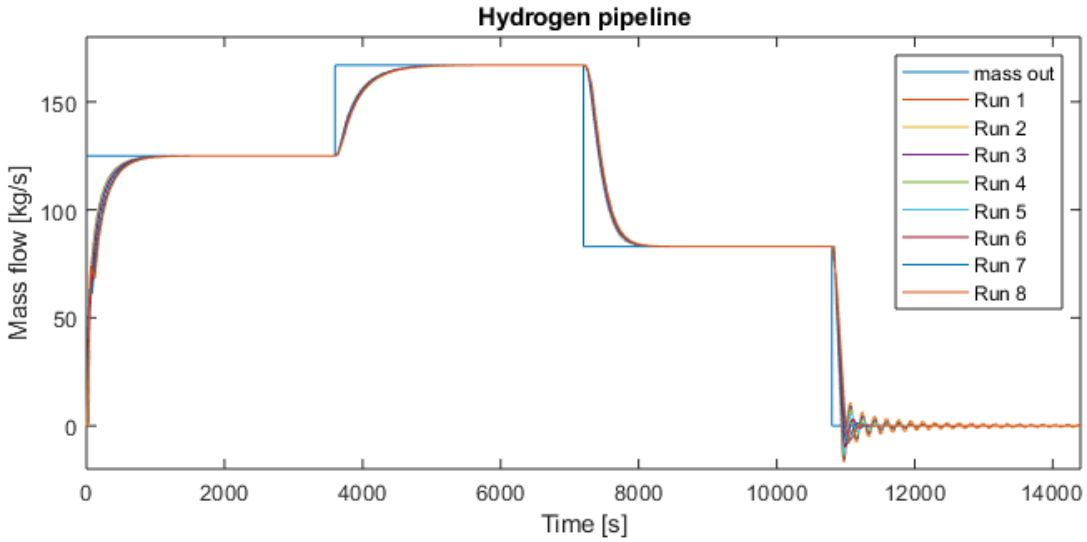

Figure 6.1: Response of the inlet mass flow on an outlet mass flow profile using different grids.

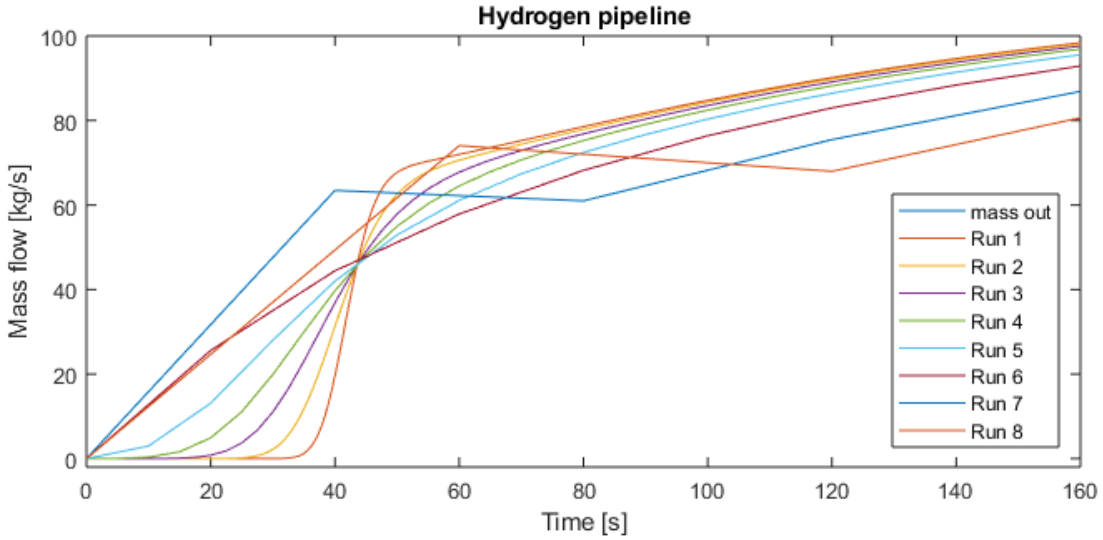

Figure 6.2: Response of the inlet mass flows on the instant opening of the outlet valve. This plot depicts the first 160 seconds of Fig. 6.1.

The results of the pressure plot are shown in Fig. 6.3. The error at the beginning is less significant as in the mass plot. Fig. 6.4 shows that the 5 finer grids capture the sudden pressure drop at the pipe outlet quite well, especially the finest grid. This is the sudden pressure drop which causes the pressure wave along the pipe. The coarser grids, on the other hand, show a more linear drop.

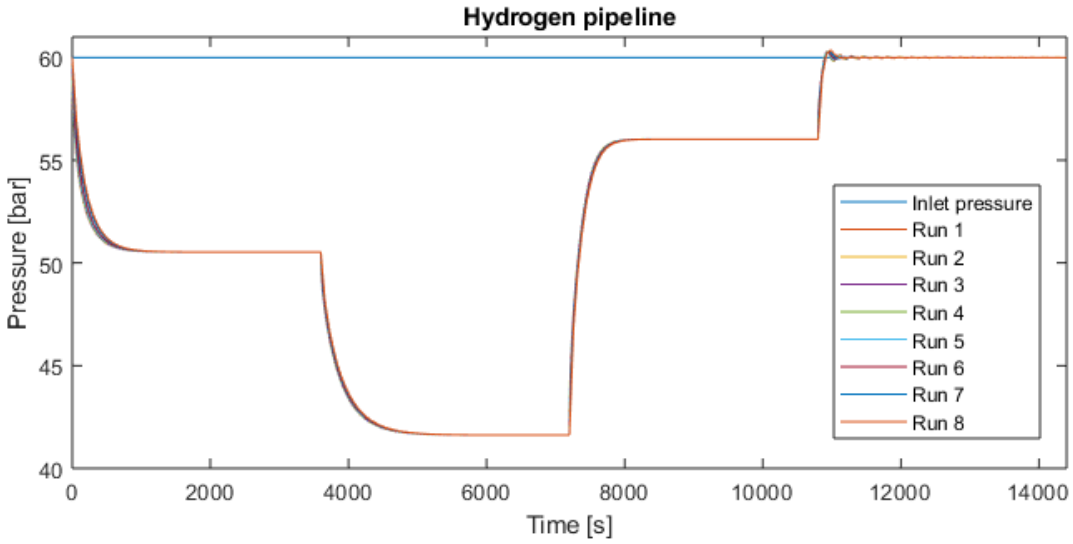

Figure 6.3: Response of the outlet pressure on an outlet mass flow profile using different grids.

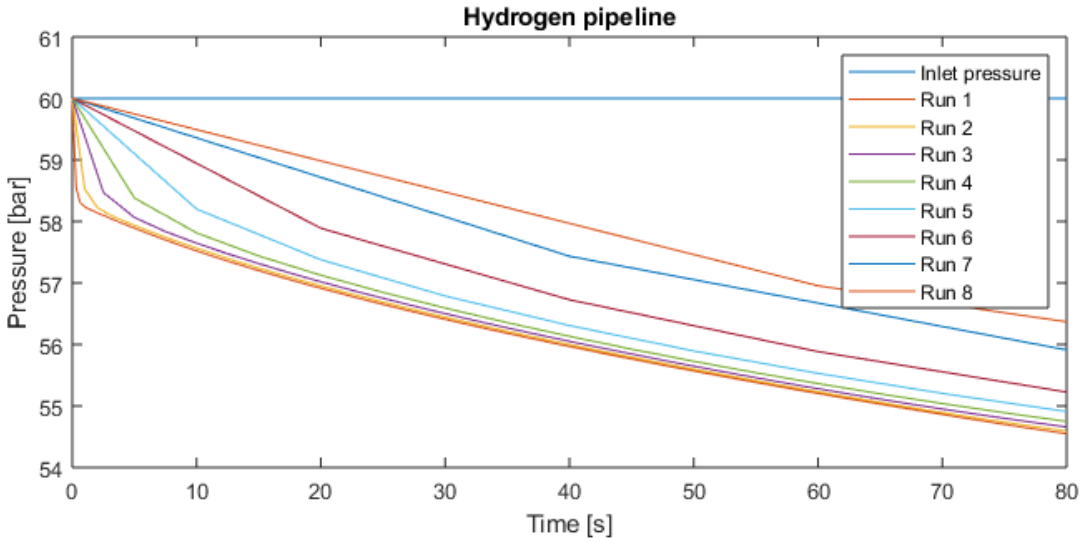

Figure 6.4: Response of the outlet pressure on the instant opening of the outlet valve. This plot shows the first 80 seconds of Fig. 6.3.

A comparison between the pressure results from the methane (Fig. 5.4) and the hydrogen (Fig. 6.3) pipeline substantiates that transporting the same amount of chemical energy, the pressure losses in a hydrogen pipeline are larger.

The fine grid gives the most exact solution, however, this case takes about 32 minutes to simulate a 30 minute run. The figures show that the differences between the finest and the most coarse grid are relatively small, except for start-up and shut-down of the mass flow. However, the simulation time of Run 8 is 5200 times faster than that of Run 1. Moreover, the transient periods for these runs take about 25 minutes, meaning that small time steps (Δt <10 s) are not necessary to capture the transient behaviour of the pipelines. Therefore, the model uses a time step of 60 seconds as this

will greatly enhance the simulation speed and will still be able to capture sudden flow changes. The spatial step will be adjusted per case in order to minimize the model errors.

For the grid-dependency study, a constant friction factor and speed of sound is used. However, in reality the friction factor varies significantly due to the transient nature and the highly fluctuating mass flow. Therefore, for this study, the friction factor and speed of sound will be a function of space and time. This will make the simulation more accurate.

6.1.2 Pipeline algorithm

An algorithm for the pipe flow is written for this study. This algorithm determines when to switch between different input values when calculating the flow parameters based on defined conditions. These conditions are given below:

- Switch between transient and steady-state flow: During steady-state flow, all flow parameters stay constant, therefore, the numerical iteration method is not necessary. So all output values are equal to the input values. This significantly increases simulation speed during steady-state flow.
- Switch between defined known flow values at pipe inlet and outlet: In order to solve for the flow, two of the four inlet and outlet values (p_{in}, p_{out}, $\dot{m}_{\text{in}}$, $\dot{m}_{\text{out}}$) must be known at each time instant. For example, during flow $\dot{m}_{\text{in}}$, p_{out} are the known model input values at each time instant. After the inlet valve closes, the average pipeline pressure starts to increase. When this pressure reaches its initial condition, the outlet valve will also close. At this point, the known model input values are switched to $\dot{m}_{\text{in}}$ and $\dot{m}_{\text{out}}$ which are both set to zero. Now, the oscillating flow in the totally closed pipeline can still be captured and no oscillation between negative and positive flow occurs at the pipe outlet. When the flow initiates again, the known values switch back to $\dot{m}_{\text{in}}$, p_{out}.
- Varying start-up temporal step: Large temporal and spatial steps cause large errors during pipeline start-up, as shown in section 6.1.1. In order to prevent this, the algorithm causes the model to use a smaller temporal step during start-up of the flow, thus reducing the computational error.
- Varying pipeline temporal step: The model can also use a smaller pipeline temporal step compared to the overall model temporal step during the whole simulation.

Part III

Chapter 7

Cases: Sizing the hydrogen-based energy system

This section describes sizing of the 4 cases (Fig. 7.1). These cases will be used to analyse the hydrogen system and the modeling performance.

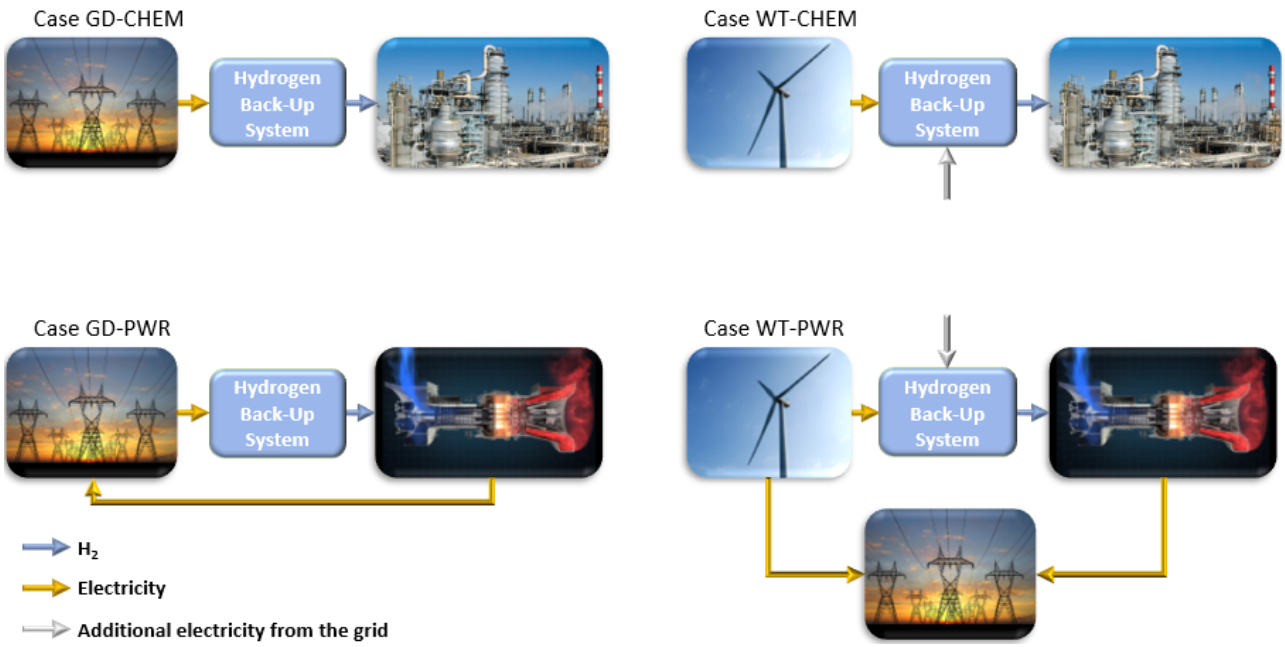

Figure 7.1: Simplified schematic of the HES with the various possible sources and services.

The model makes use of many set parameters determined by literature which are given in Chapter 4. However, there are several case dependent parameters which will be elaborated in this section. These case dependent parameters depend on the input and output profiles of the HES. The input for the source is either a hourly wind or a hourly APX price profile. These profiles are historical data sets of 2017. The output of the service is a hydrogen demand profile for the chemical industry or a certain energy demand for a CCGT. Based on these profiles, the case dependent parameters, listed below, are determined.

- Number of wind turbines in the wind farm.

- Maximum APX price for PEME operation.
- Number of PEME stacks.
- Transmission, injection and discharge pipeline diameters.
- Diameter and height of the salt cavern and thus the cavern volume.
- Minimum APX price for the CCGT operation.

Operational limits of the HES The cavern is assumed to be at a depth of 1000 metres where the minimum and maximum allowable pressures are 60 and 180 bar. The HES operates such that the initial and final pressures inside the cavern are approximately equal and that the minimum and maximum cavern pressure stays within a 61-65 bar and 175-179 bar range, respectively. Ensuring that the cavern pressure limits are never reached and that the cavern capacity is almost fully used. Furthermore, the maximum cavern pressure gradient is 1.0 MPa·day^{-1}. The first and second transmission pipelines are both 50 kilometres long and operate between 90-125 bar and 70-100 bar, respectively. All the PEME stacks operate as one unit with a single power input and under the same conditions.

Reference case A Reference Case (RC) is defined to size the HES for the different cases. Here, the wind farm, PEME and CCGT were all given approximately the same rated power. The RC makes use of a 294 MW PEME consisting of 5000 stacks driven by a wind farm consisting of 104 turbines with a rated power output, after WECS losses and conversion by the rectifier, of around 2.83 MW per turbine.

7.1 Case GD-CHEM: Power grid - Chemical industry

This section gives the case where a constant and continuous flow of hydrogen is delivered to the chemical industry. Therefore, no service conversion process is included as the hydrogen will be the final product of this system. Uses for the hydrogen are given in section 2.1.5. The PEME always runs at the rated power during operation. The delivery values for the chemical industry are given in Table 7.1.

Table 7.1: Values of the chemical industry parameters.

Parameter	Value	Unit
Mass flow	3000	$Nm^3 \cdot h^{-1}$
Delivery pressure	20	bar
Delivery temperature	10	°C

7.1.1 APX spot price for power

The maximum APX price at which the PEME is operational and the APX spot price profile determine the hydrogen production profile.

The PEME needs electricity bought from the APX to produce hydrogen. A certain maximum APX price is chosen for the PEME at which electricity is bought from the market. For all prices equal or below this maximum price, the PEME will be operational. Figure 7.2 shows average hydrogen cost for the PEME averaged over a year as a function of the maximum APX price. The plot is valid for any PEME size as it gives the specific hydrogen price. The curve is not linear as the average hydrogen

cost depends on both the APX spot price for power and the amount of hours that the PEME operates during certain spot prices. For example, for a maximum price of 30 €·MWh^{-1}, the average production cost per kilogram hydrogen in 2017 is €1.468. The CCGT is also plotted and is used later on.

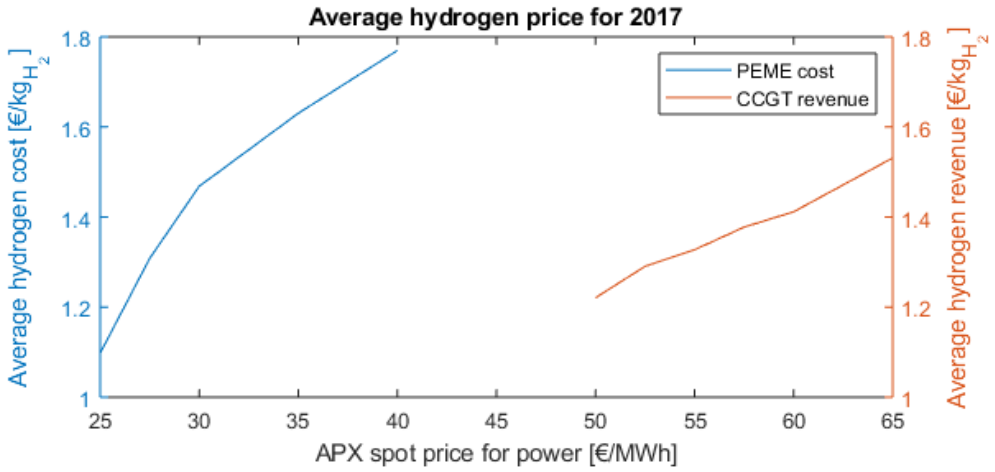

Figure 7.2: Average hydrogen cost and revenue of the PEME and CCGT for 2017, respectively, based on APX price.

It would be beneficial to only operate the PEME when the APX price is low in order to lower the hydrogen production costs. However, a lower APX price also results in less production as the capacity factor of the PEME will decrease, as shown in Fig. 7.3. This figure shows the total PEME cost and produced hydrogen mass for 2017 using the PEME of the RC.

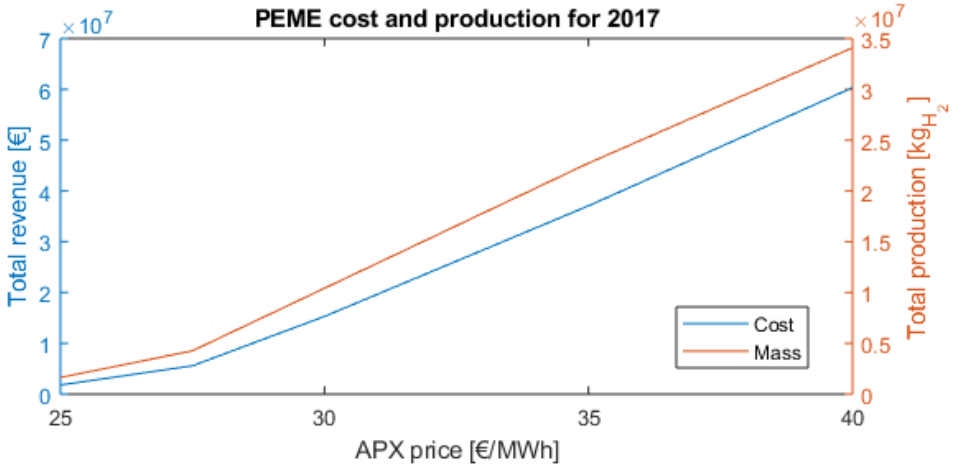

Figure 7.3: Total hydrogen production and cost of the PEME using the RC for 2017.

7.1.2 Sizing the system

As can be seen in Fig. 7.2, both 30 and 35 €·MWh^{-1} give a reasonable PEME cost. However, for the lower price, the capacity factor will be low resulting in the need of a higher maximum output. It is preferred to have a higher capacity factor which also results in a more evenly hydrogen production throughout the year, therefore, 35 €·MWh^{-1} is used.

Figure 7.3 shows that for this price 22.73 million kilogram of hydrogen is produced by the RC PEME. As this is too much for Case GD-CHEM, the number of PEME stacks will be determined according to Eq. 7.1.

$$n_{\text{st}} = \frac{M_{\text{chem}}}{M_{\text{PEME,ref}}} \cdot n_{\text{st,ref}} = \frac{2.1625e^6}{2.2735e^7} \cdot 5000 = 475.6 \approx 476 \tag{7.1}$$

A year run is done with the correctly sized PEME, resulting in a production, consumption and accumulation profile (Fig. 7.4) from which the necessary storage capacity can be determined at each time instant during 2017.

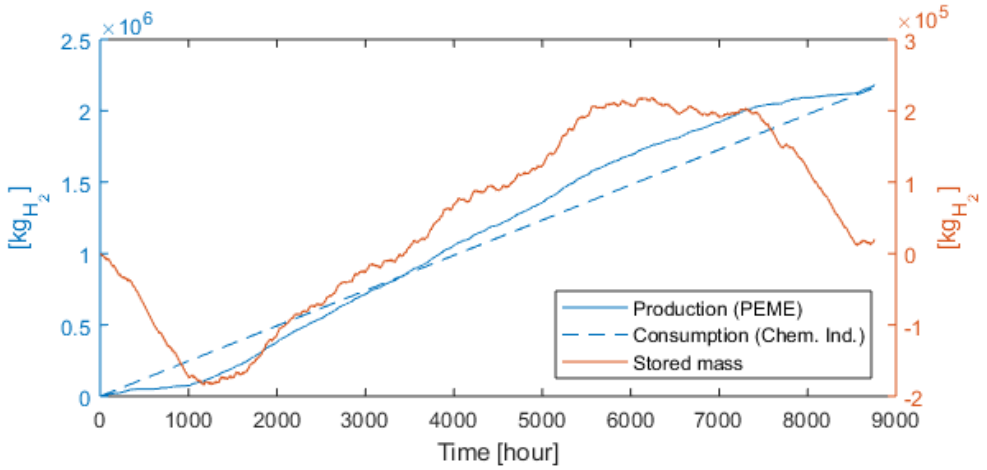

Figure 7.4: Production, consumption and net stored mass of Case GD-CHEM for 2017.

This plot is used to estimate the cavern volume using the real gas law and difference between the minimum and maximum 'Stored mass' multiplied with the working gas to cushion gas ratio and a safety factor, as shown in Eq. 7.2. The compressibility factor is taken at 180 bar pressure and 45°C, which are the maximum cavern pressure and ground temperature at a depth of 1000 metres, respectively.

$$V_{\text{cav}} \approx \frac{Z\bar{R}T}{p_{\text{max}}}\Delta M \cdot \frac{p_{\text{max}}}{p_{\text{max}} - p_{\text{min}}} \cdot F_{\text{s}} = \frac{1.45e^6}{180e^5} \cdot (2.18e^5 - -1.85e^5) \cdot \frac{180}{180 - 60} \cdot 1.2 = 53,656 \text{ m}^3$$

$$\Delta M = (M_{\text{max}} - M_{\text{min}}) \tag{7.2}$$

As the mass flows are significantly lower for Case GD-CHEM than for the RC, the pipeline diameters will be sized accordingly to maintain a reasonable pressure drop and to keep the pressure range of the first and second transmission pipelines between the defined operating pressure ranges. The case dependent parameters are given in Table 7.4. Here, the final cavern volume is slightly larger than the calculated value as the radius and height of the cavern are rounded off to integers.

7.2 Case WT-CHEM: Wind - Chemical industry

A wind farm produces electrical power for the electrolyzer based on a hourly wind profile. Due to the variable wind farm power output, the PEME will be running under various current densities resulting in a fluctuating hydrogen output. Only the rectifier and the PEME stacks will use the wind power. The other components take the electricity from the grid. The chemical industry parameters are equal to Case GD-CHEM and are given in Table 7.1.

7.2.1 Sizing the system

The hydrogen consumption profile is already clarified in section 7.1.1. The hydrogen production, on the other hand, depends on the wind profile, wind farm size and PEME size. First, the rated power of the wind farm and the rated power of the PEME are set approximately equal. The rated input power of the PEME and the rated rectifier power output are approximately linearly dependent on the number of stacks and the number of turbines, respectively, as shown in Figs. 7.5 and 7.6. Figure 7.5 shows the PEME power consumption as a function of the rectifier power output. This figure clearly shows that the PEME only operates between a minimum and maximum power range. The RC PEME with 5000 stacks, for example, operates between 91 and 294 MW.

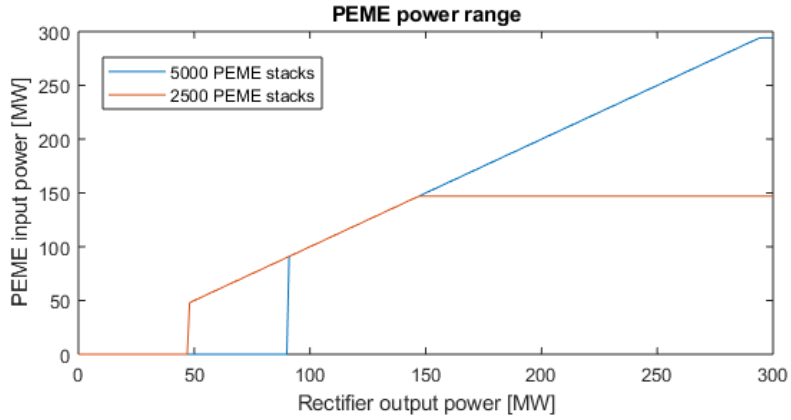

Figure 7.5: PEME power input as a function of the rectifier power output.

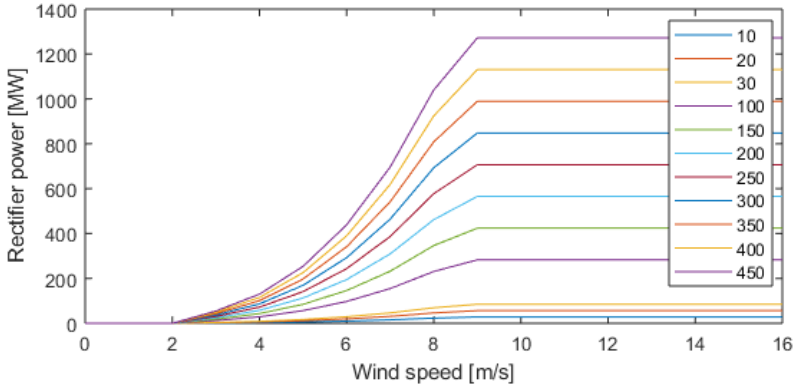

Figure 7.6: Rectifier power output as a function of wind speed for several wind farm sizes.

Figure 7.6 shows the rectifier output as a function of the wind speed for several wind farm sizes. The wind farm only produces power within a certain wind speed range and more turbines result in more power generation. The rated power of the RC PEME is 294 MW, resulting in 0.0588 MW·stack^{-1}. The rated power of a wind farm with 100 turbines gives 282.7 MW at the rectifier output, resulting in 2.827 MW·turbine^{-1}.

Equation (7.3) is used to estimate the size of the wind farm needed for the RC. Thereafter, a year run is done to determine the capacity factor of the PEME. This capacity factor stays approximately equal when the rated powers of the PEME and wind farm are kept equal. In turn, the hydrogen production per stack depends on this capacity factor.

$$N_{\text{tur}} = \frac{P_{\text{PEME,rated}}}{P_{\text{tur,rated}}} \tag{7.3}$$

The number of stacks needed for Case WT-CHEM can be determined using Eq. 7.4 where the total mass of hydrogen for the chemical industry is divided by the amount of hydrogen that a single stack can produce under a certain capacity factor.

$$N_{\text{st}} = \frac{M_{\text{ch-ind}}}{M_{\text{st}} \cdot CF_{\text{PEME}}} \tag{7.4}$$

Finally, the wind farm size is determined using the new rated power of the PEME using Eq. (7.3) again. The procedure from section 7.1.2 is taken to find the cavern volume. The resulting values can be found in Table 7.4.

7.3 Case GD-PWR: Power grid - Power back-up

This section describes the case where the hydrogen is used for electricity production by a CCGT. When the APX spot price is low, electricity is bought to power the PEME and when the APX spot price is high the electricity produced by the CCGT is sold. For this system to be feasible, at least the operational energy costs should be lower than the revenue. The CCGT parameters are shown in Table 7.2 and several operational constraints are listed below.

- The CCGT ramp up time from zero to full load is one hour.
- The CCGT ramp down time from full to zero load is 30 minutes.
- The CCGT turbine only switches on when the spot price for power is higher than or equal to a certain value for at least 4 hours.

Table 7.2: Model input parameters for the CCGT.

Parameter	Value	Unit
Linear ramp up rate	3535	$Nm^3 \cdot h^{-1}$
Linear ramp down rate	7070	$Nm^3 \cdot h^{-1}$
Maximum power output	350	MW
Efficiency	0.55	-
Delivery pressure	20	bar
Delivery temperature	10	°C

7.3.1 APX

Historical hourly APX price data from 2017 is sorted based on price level, shown in Fig. 7.7. The left peak shows a high energy price which is beneficial for the gas turbine to generate revenue. An energy price range of 50 - 60 €·MWh^{-1} will be used as the minimum price range for the CCGT to be operational as this covers most of the peak. The right side of the plot are the low prices which are beneficial for the PEME. The maximum electricity price range in which the PEME will be operational is set to 25 - 40 €·MWh^{-1}. Meaning that there is also a price range where both the PEME and the CCGT are switched off.

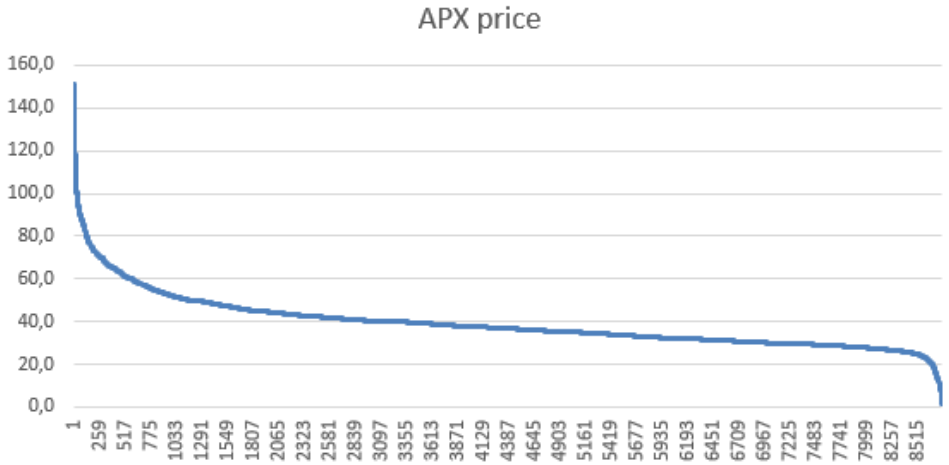

Figure 7.7: Hourly APX spot prices for power sorted by the amount of hours it occurs during 2017.

Figure 7.2 which has been discussed earlier shows the hydrogen revenue curve for the CCGT. The position on the curve determines the revenue per kilogram of hydrogen consumed by the CCGT. When, for example, electricity is sold from a minimum price of 60 €·MWh^{-1}, the average hydrogen revenue for 2017 will be 1.412 €·kg$_{H_2}^{-1}$. So, the cost price must be at least equal or preferable lower than this price to break-ever or gain profits, respectively. This cost price, in turn, depends on the maximum price for which the PEME is operational. In this situation, the maximum spot price used for the PEME must be equal or lower than 29.1 €·MWh^{-1} in order to break-even or gain profits, respectively. Figure 7.2 shows that a break-even point is possible between the upper and lower hydrogen revenue for the CCGT, being 1.221 and 1.531 €·kg$_{H_2}^{-1}$, respectively, as the PEME curve crosses all these prices. So, the PEME maximum price must be somewhere between 26 - 32 €·MWh^{-1}.

7.3.2 Sizing the system

A price of 60 €·MWh^{-1} is taken for the CCGT as a profit is possible for this price and a sufficient revenue of approximately 10.8 million euro is obtained, as shown in Fig. 7.8. This means that around 7.7 million kilogram of hydrogen is needed for the CCGT. A buy price of 27.5 €·MWh^{-1} is used for the PEME, resulting in a slightly lower cost price per kilogram hydrogen produced compared to the revenue per kilogram hydrogen consumed.

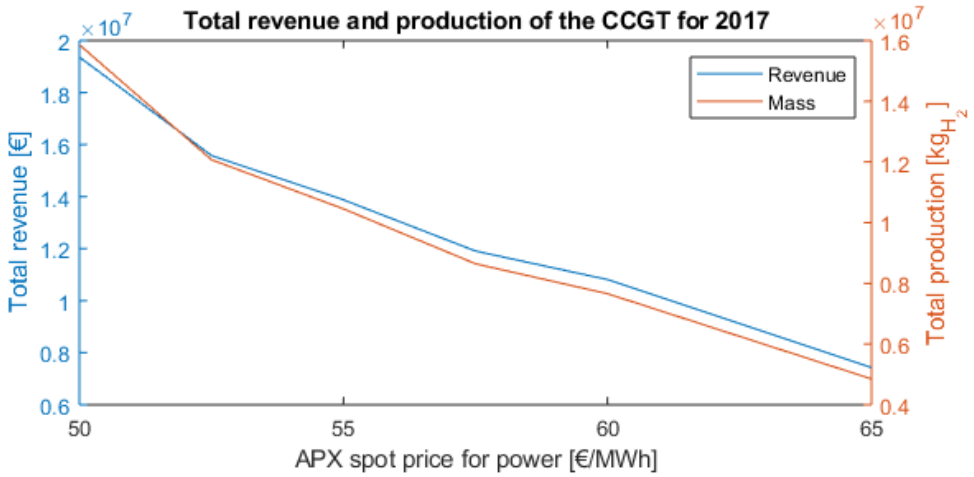

Figure 7.8: Total revenue and consumed mass values for 2017 for different minimum APX prices used for the CCGT.

The size of the PEME is determined by the maximum APX price of 27.50 €·MWh^{-1} and an annual production capacity of 7.7 million kg. Fig. 7.3 shows that the annual production at this cost price of the RC PEME is around 4.3 million kilogram hydrogen. Therefore, the PEME must become a factor $\frac{7.7}{4.3}$ bigger resulting in a PEME with approximately 9000 stacks (Rated power of 529 MW). Sizing of the cavern follows the approach from section 7.1.2.

7.4 Case WT-PWR: Wind farm - Power back-up

The wind-based system makes use of a constant base load of 100 MW. When the power production by the wind farm exceeds the base load, the excessive power is used to drive the PEME. If the wind power drops under the base load, the gas turbine is switched on to produce electricity to meet the base load demand. For this case, the CCGT constraints given in section 7.3 were neglected. The CCGT input parameters are given in Table 7.3. The electricity used for the PCSs and the PEME BoP will be taken from the power grid.

Table 7.3: Input parameters for the CCGT for Case WT-PWR

Parameter	Value	Unit
Maximum power output	100	MW
Efficiency	0.55	-
Delivery pressure	20	bar
Delivery temperature	10	°C

7.4.1 Sizing the system

Part of the base load power requirements are met by the wind farm and part by the CCGT. However, the CCGT route, or indirect route, encounters many more losses due to hydrogen production, transport, storage and conversion into electricity. The wind farm and PEME are sized using Figure 7.9. Several simulations for 2017 are done to find certain power curves as a function of the number of turbines.

More turbines, means more direct supply and less indirect supply up until a certain number of turbines. The red line represents the energy surplus coming from the wind farm, thus after subtracting the base load. The direct base load supply by the wind farm does not consider additional power losses. The yellow line represents the energy needed for the indirect route to produce sufficient hydrogen to satisfy the base load demand. This value is calculated by dividing the indirect base load supply by the assumed indirect route efficiency of around 24%[1]. Note, this efficiency does not take the wind farm losses into account.

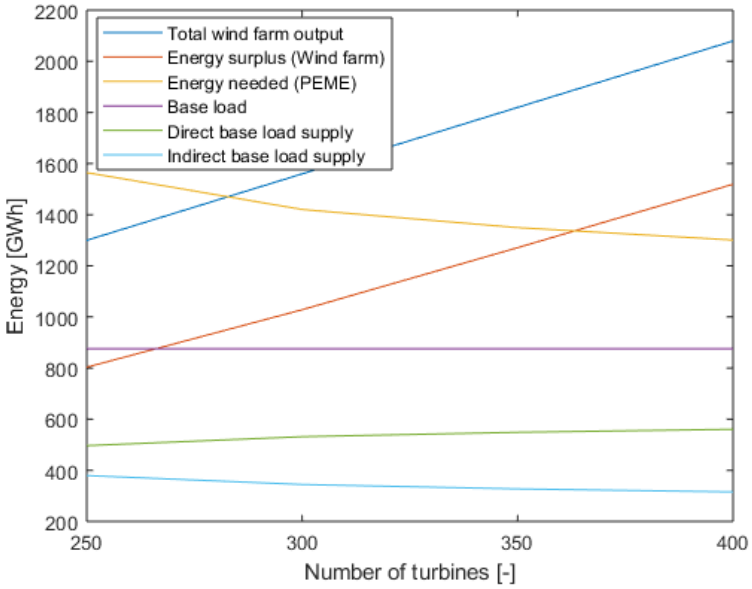

Figure 7.9: Plot for matching the wind farm size with the base load.

The point where the red and yellow lines cross, is the point where the total base load is met during the whole year. Therefore, around 367 turbines are needed. To match the rated wind farm output with the rated PEME power, around 17,913 stacks are needed. The cavern volume and pipeline diameters are fitted according to the methods explained in previous sections. The result are given in Tab. 7.4.

7.5 Sizing results

Table 7.4: Case dependent HES configuration.

Parameter	Case GD-CHEM	Case WT-CHEM	Case GD-PWR	Case WT-PWR	Unit
APX_{PEME}	35	-	27.5	-	€·MWh^{-1}
APX_{GT}	-	-	60	-	€·MWh^{-1}
N_{tur}	-	30	-	367	-
n_s	476	1,450	9,000	17,913	-
V_{cav}	54,475	59,923	942,100	794,190	m^3
r_{cav}	17	17	42	40	m
h_{cav}	60	66	170	158	m
p_{ini}	116	132	121	141	bar
D_{TP1}	0.07	0.085	0.18	0.2	m
D_{TP2}	0.048	0.48	0.22	0.145	m
D_{IP}	0.07	0.085	0.18	0.2	m
D_{DP}	0.048	0.048	0.22	0.145	m
p_{TP1}	90	90	90	90	bar
p_{TP2}	90	90	90	90	bar

[1]Assumed rectifier, PEME, PEME power limits, and CCGT efficiencies of 0.90, 0.70, 0.70 and 0.55, respectively

Chapter 8

Analysis of the cases

In this chapter the results of the 4 cases are presented and analysed. Some of the results are already presented in section 7, being the case dependent input parameters which determine the configuration of the HES. The output parameters, on the other hand, are the results of the simulation runs which are divided into operational and performance results. The results are produced by the HES model by simulating a year of operation of the 4 cases, starting from 1 January till 31 December 2017.

Operational The operational results show if the system components are properly controlled, the thermodynamical behaviour is realistic and if the HBS meets the demand. These results include:

- Pressure and temperature range of the salt cavern.
- Surplus of chemical energy inside salt cavern.
- Wind farm, PEME and CCGT capacity factor.
- PEME, compressors and CCGT on-off switches.
- Minimum and maximum component pressures, temperatures and mass flow rates.

Moreover, the dynamics of the system are analyzed by plotting the results of the components during certain transient periods and describing the behaviour. As the behaviour per component may not differ much per case, a component will only be analyzed for the most interesting case. Moreover, the stated operating limits from Ch. 7 will be used to determine whether the system operates within these limits.

Performance The performance results give the energy and exergy flows and the efficiencies of the HBS. For Case GD-PWR, these results will also show whether the system is feasible in terms of operational costs and revenue.

- Energy input and output.
- Heat removal.
- Exergy destruction.
- Energy and exergy efficiency.

8.1 Wind farm

The wind farm has a capacity factor (CF) of 19%, meaning that the farm only has 1,655 full load hours per year. Therefore, it must be relatively large to meet the power demand. The used turbines have a cut-in, rated and cut-out wind speed of 3, 11.5 and 25 $m \cdot s^{-1}$, respectively. When studying the wind speed data at turbine height (Fig. 8.1), most hours the wind speed varies between 1.3 - 8.1 $m \cdot s^{-1}$ with an average speed of 5.4 $m \cdot s^{-1}$ and a mean deviation of 2.4 $m \cdot s^{-1}$. These values are far below the rated wind speed. Apx. O gives a description of the wind power losses, for Case WT-CHEM, due to the wind farm operational limits.

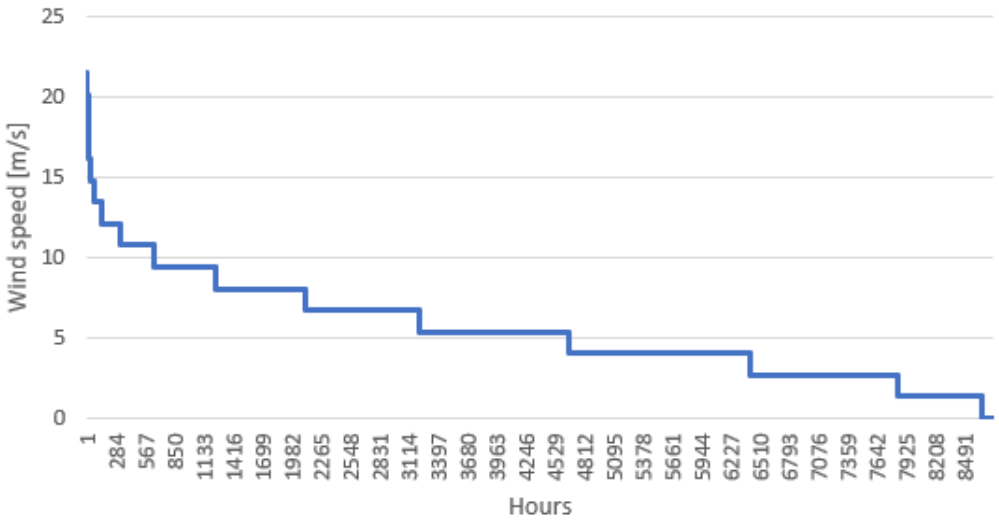

Figure 8.1: Sorted hourly wind speed data.

The capacity factor can be increased by using different turbines with lower cut-in and rated speeds which are closer to ground level. This way the rated power output of the wind farm will be lower, but due to a higher CF, the demand will still be met.

The power loss from a wind farm is significant. A wind farm can theoretically only capture 59.4% of the wind power, known as the Betz limit. Furthermore, the mechanical, gearbox and generator losses all lower the resulting wind farm output. For this study, the losses of the wind farm will not be considered when calculating the power-to-gas efficiency. Therefore, the wind farm power output will be the starting point.

8.2 Salt cavern

The salt cavern functions as the control volume of the HES, therefore, the yearly pressure profile inside the cavern is an important result. Figures 8.2 - 8.5 present the properties of the stored hydrogen during one year for all cases. Hereby, it is important that the initial and final pressures are almost equal, so that the supply and demand is balanced over a whole year. Furthermore, the minimum and maximum pressure must be in the defined range, ensuring full use of the cavern capacity. Lastly, the pressure gradient cannot exceed a certain limit as this may cause unwanted defects in the cavern walls.

The small variance between the initial and final pressures for all cases indicate that the PEMEs are correctly sized. This can also be seen in Table 8.1 where the amount of overproduction is insignificant compared to the stored chemical energy.

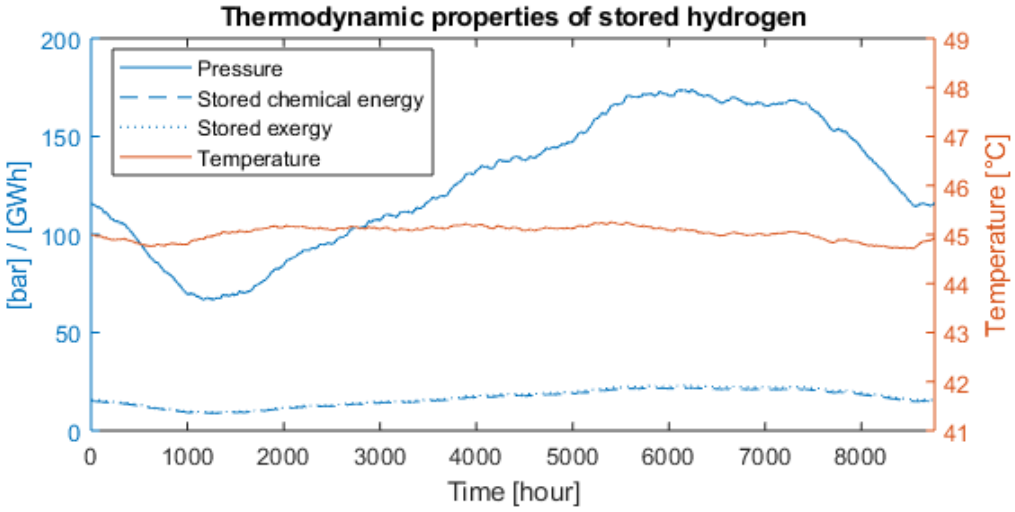

Figure 8.2: Year results of salt cavern operation (Case GD-CHEM).

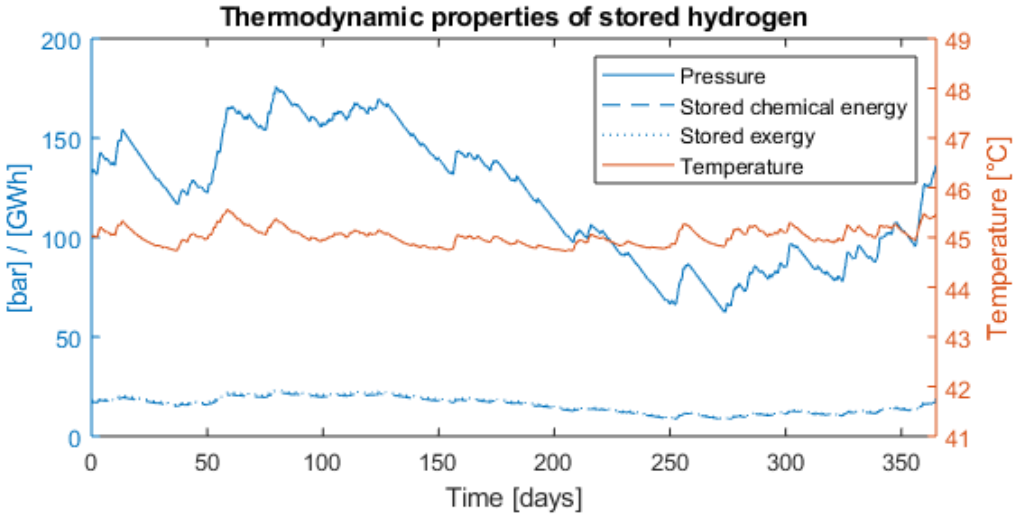

Figure 8.3: Year results of salt cavern operation (Case WT-CHEM).

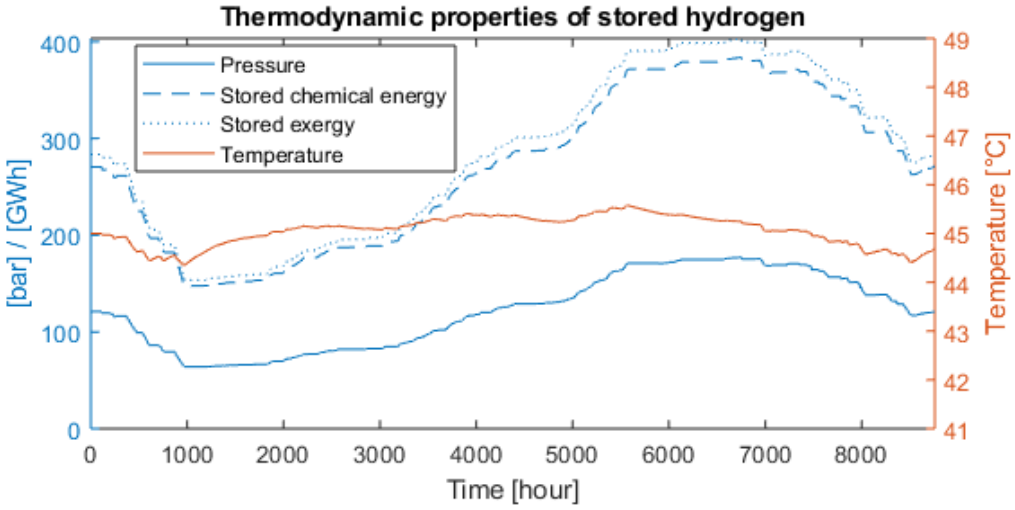

Figure 8.4: Year results of salt cavern operation. (Case GD-PWR).

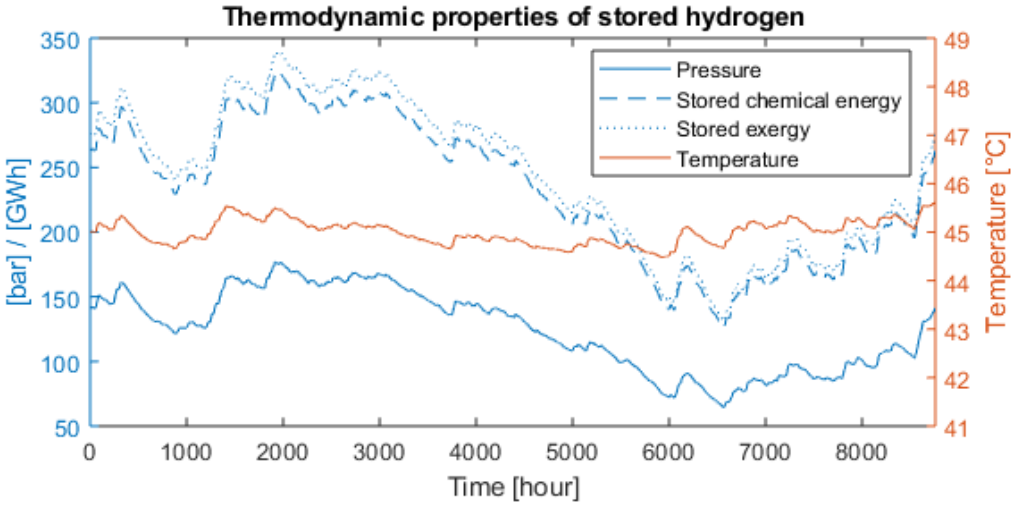

Figure 8.5: Year results of salt cavern operation (Case WT-PWR).

The results from Tab. 8.1 show that Case GD-PWR and WT-PWR fully operate within the defined limits. Therefore, the cavern is correctly sized for these cases. Case GD-CHEM, however, does not make full use of the total cavern capacity, so a slightly smaller cavern should have been used. Case WT-CHEM experiences a slightly too high pressure gradient at certain moments. Using a bigger cavern, however, will result in more unused capacity, therefore, a smaller PEME with a higher capacity factor is the more desirable solution. This way, the PEME output will be more spread throughout the year.

Table 8.1: Salt cavern storage results.

Parameter	Limits	Case GD-CHEM	Case WT-CHEM	Case GD-PWR	Case WT-PWR	Unit
Min./Max. pressure	60-65 / 175-180	66/174	62/176	64/177	65/177	bar
Min./Max. pressure gradient	-10/10	-0.1/2.3	-1.8/10.6	-7.9/4.5	-2.7/9.6	$\text{bar}\cdot\text{day}^{-1}$
Overproduction	-	0.05	0.46	0.64	0.06	GWh

An interesting feature of both GD cases is that during the winter months, the cavern is discharged while during the summer months the cavern is charged. Meaning that during the summer months, the APX spot price for power is low and thus the PEME is operational. Therefore, the HESs demands seasonal storage as most of the hydrogen is produced during the summer months and only to a small fraction during the winter months. For the WT cases, on the other hand, it is the other way around. So, the cavern is discharged during the summer months due to lower average wind speeds while there is still significant power demand. So, for all cases, the caverns only have one charge-discharge cycle during 2017.

The caverns for the PWR cases are much larger than the CHEM cases due to the fact that no simultaneous injection and discharge takes place and they experience higher injection and discharge mass flow rates.

For Case GD-PWR, the cavern pressure stays relatively constant during certain periods as there is no injection or discharge flow. During these periods, the spot price is too low for the CCGT to be operational and too high for the PEME be operational. The only pressure changes during these periods are caused by temperature change due to heat exchange with the cavern walls. For this case, the plot also clearly depicts that the stored exergy compared to the chemical energy is significantly larger at high pressures than for low pressures. This effect is strengthened by the fact that the cavern volume is extremely large.

8.2.1 Cavern temperature

The temperature curves only show a slight variation, meaning that the cavern pressure fluctuation does not have a significant influence on the stored hydrogen temperature. However, the temperature profile does follow the pressure profile on a short time frame, as can be seen in Fig. 8.6. In the long time frame, on the other hand, the temperature profile does not show the same yearly wave pattern as the pressure. As pressure increases, the internal energy also increases and thus the temperature of the cavern. However, the stored gas exchanges heat with the surrounding walls. At temperatures above 45°C, heat flows from the stored hydrogen to the walls and at temperatures below 45°C the exact opposite occurs which is visible at t = 6915 and t = 6894, respectively. Furthermore, the gas enters the cavern at 45°C, so the enthalpy of this inlet stream will have little to no effect on the temperature, especially when the cavern pressure is high as heat capacity of the cavern is much higher due to the amount of mass.

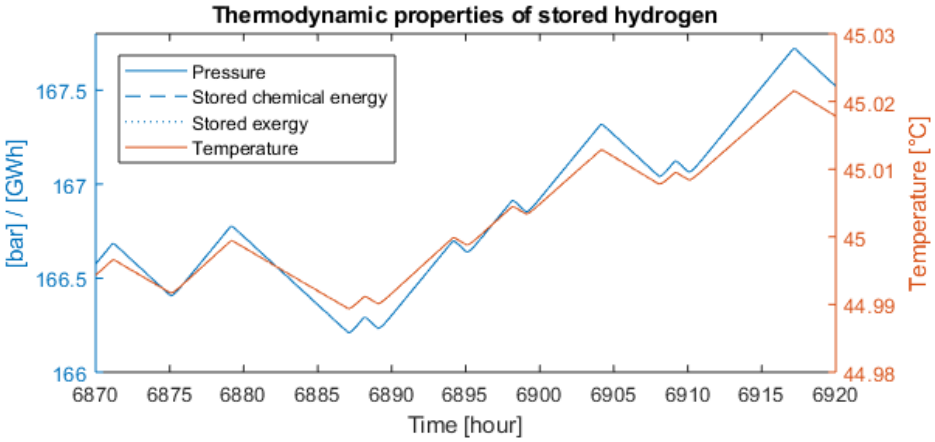

Figure 8.6: Close-up of Fig. 8.2 (Case GD-CHEM).

8.3 Case GD-CHEM: PEM electrolyzer

In this section, the PEME model results are elaborated by using Case GD-CHEM.

8.3.1 Operational conditions

For Case GD-CHEM, the PEME can either be totally off or operational at the rated power. Figure 8.7 shows that the operational pressure and temperature are equal to the set values of 35 bar, 60 °C, respectively. This proves that the model pressure and temperature are correctly controlled. It takes about 24 minutes before the PEME reaches steady state conditions starting from the initial conditions and 14 hours to cool from operational temperature to within 2% of the initial temperature.

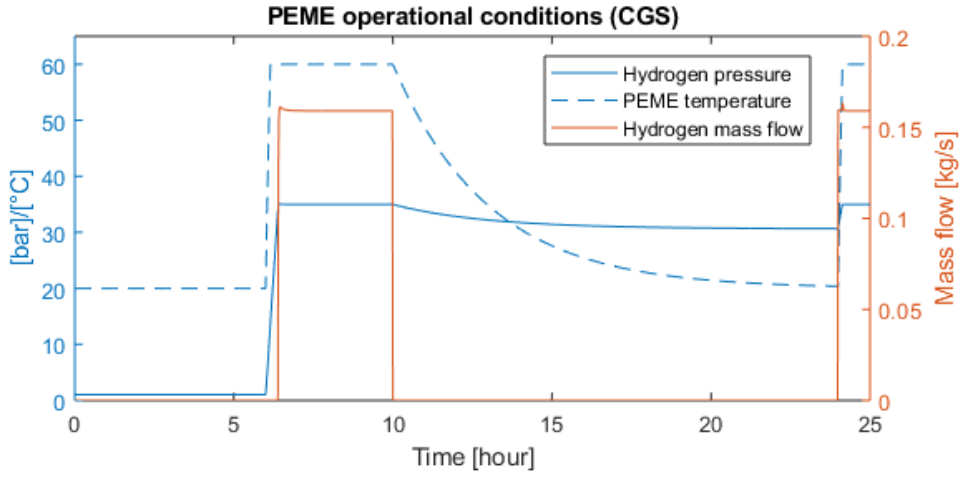

Figure 8.7: Operational conditions of the CGS. (Case GD-CHEM)

Figure 8.8 shows the various the heat flows of the PEME. All flows are plotted positive, however, the 'HEX', 'Loss', 'Anode gas flow' and 'Cathode gas flow' curves are leaving the system. It is clear that the stacks overvoltage has the biggest impact on the PEME temperature increase.

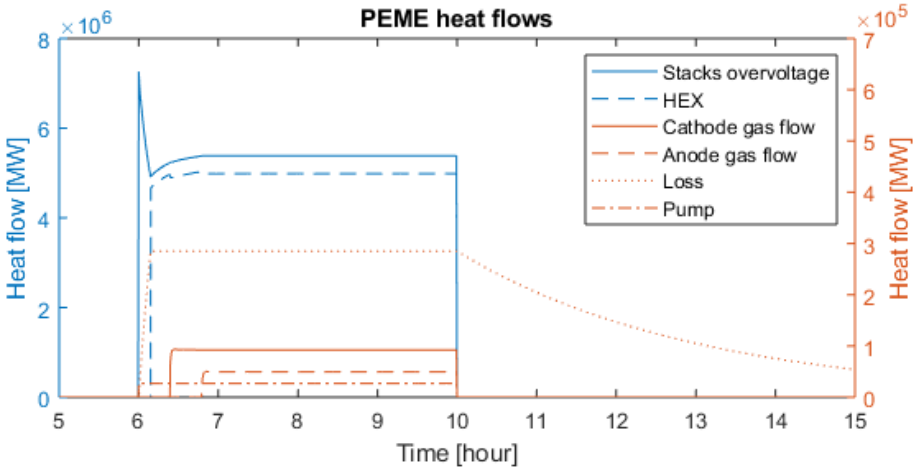

Figure 8.8: Heat flows of the PEME for one start-up and shut-down cycle. (Case GD-CHEM)

The cell voltage is higher than the thermal-neutral voltage due to several voltage losses in the stacks

(Fig. 8.9). This overvoltage is dissipated into heat energy thus increasing the cell temperature. The stacks overvoltage spike is mainly due to the membrane protonic conductivity. As the stack temperature increases, the protonic conductivity increases, thus lowering the membrane protonic resistance. Moreover, the activation overvoltage also has a small effect on this spike as the exchange current density increases with increasing temperature.

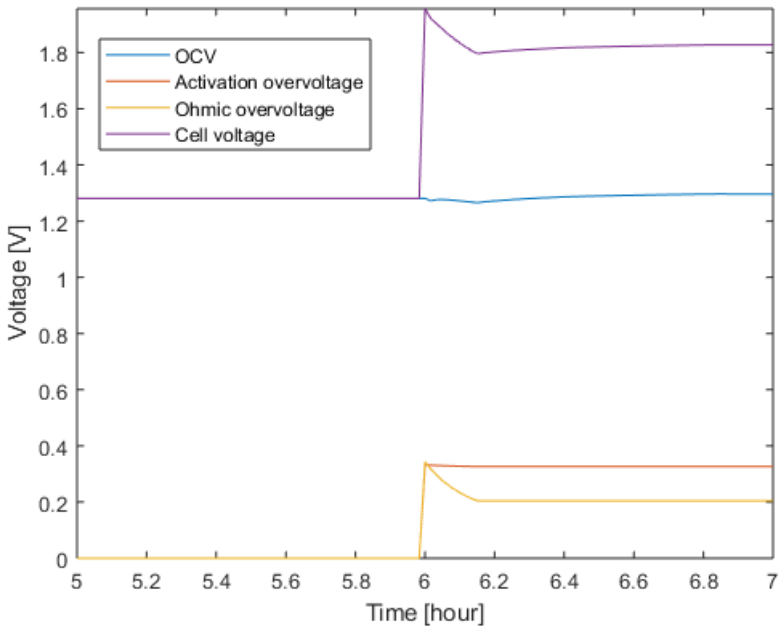

Figure 8.9: Cell voltage and overvoltages. (Case GD-CHEM)

Furthermore, the heat loss to the environment and the cathode and anode gas flow heat losses are insignificant compared to the heat production, therefore, the HEX must remove most of the heat in order to maintain the operational temperature. In reality, the HEX will have to remove slightly less heat as hydrogen and oxygen flows are saturated with water vapor and the heat loss due to vaporization is not taken into account as is the sensible heat required to warm up the fresh water inflow.

8.4 Case WT-CHEM: PEM electrolyzer

In this case, the PEME can operate in five different modes, namely off, three inter-stages and rated power modes. Figure 8.10 illustrates that the hydrogen partial pressure slightly increases with an increasing hydrogen mass flow. This is caused by a decrease of the oxygen fraction at the CGS.

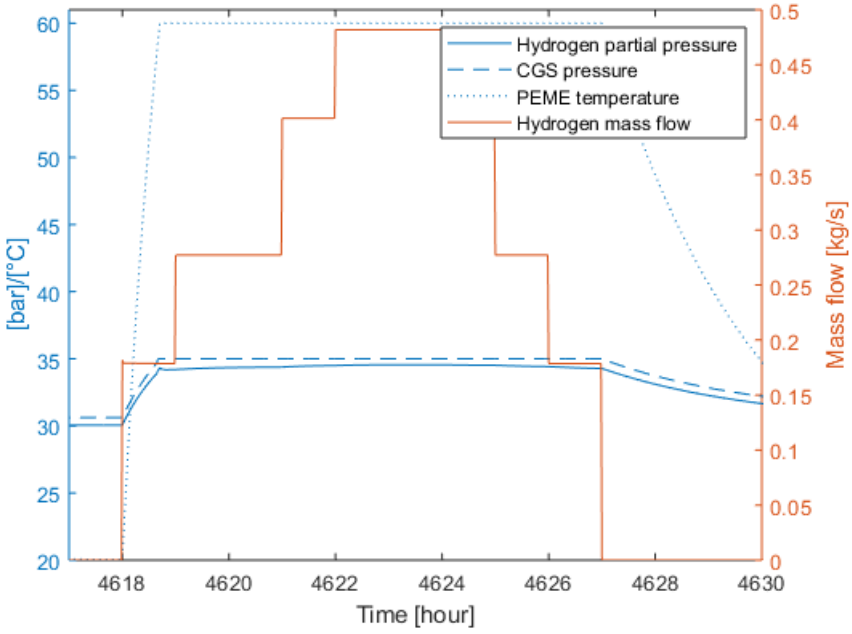

Figure 8.10: PEME operational condition at the CGS between 4617 and 4630 hours. (Case WT-CHEM)

Figure 8.11 illustrates that after an increases of the operation mode, the oxygen membrane and hydrogen back flows instantaneously jump to a much higher flow rate and then slowly drop to a steady-state value. These flows drop to a steady-state value as with each instant the concentration gradient between the electrodes decreases. When the hydrogen mass flow decreases, the exact opposite happens. Reason for the sudden jumps is the way the PEME is modeled. Here, the membrane, membrane electrode interfaces and the electrode channels are assumed to have no volume. So, a change in the hydrogen mass flow has an instantaneous effect on the molar fractions at these locations which, in turn, influence the flow rates again. The oxygen and hydrogen fraction at the CGS and AGS, however, react much less drastic as the CGS and AGS do have volumes.

The hydrogen back flow and the oxygen membrane flow rates from the previous instant are used in order to prevent a model loop resulting in model failure. When the PEME switches off, the membrane and back flows are also assumed to stop instantaneously.

In terms of operational safety, one must look at the hydrogen fraction at the AGS. A fraction higher than 4% can result in an explosive mixture which should be avoided. This fraction can increase as the catalyst at the anode side is not suited for water formation. Figure 8.11 shows a maximum hydrogen fraction of approximately 3.4% which is below the explosive limit. The oxygen fraction at the CGS does not pose a threat, but it will reduce the PEME efficiency as the oxygen can react with the

hydrogen, forming water, due to the used catalyst at the cathode. However, water formation is not accounted for in the used model.

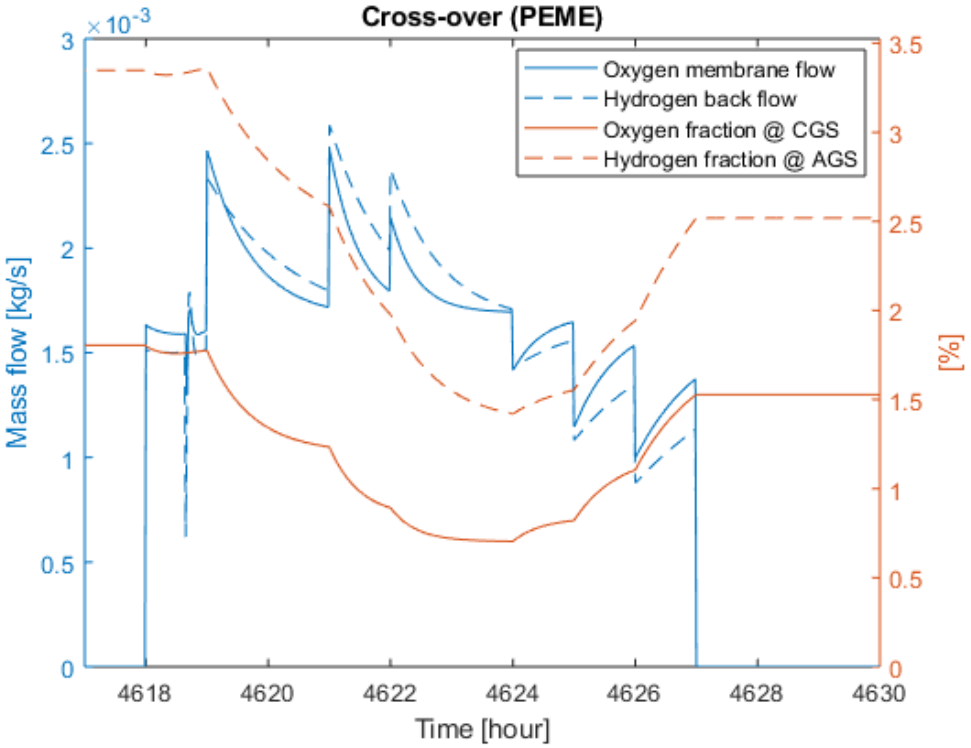

Figure 8.11: Membrane cross-over of hydrogen and oxygen between and the influence on the oxygen and hydrogen fraction at the AGS and CGS, respectively (Case WT-CHEM).

8.4.1 PEM electrolyzer power limits

The PEME power limits are the result of a mismatch between the wind rectifier power output and the PEME power input. This is caused by three factors. The first being the minimum power requirements for the PEME. As the PEME operates as one unit, all the stacks switch on or off depending on the power input. For Case WT-CHEM, the minimum power requirements are defined by the minimum current density, cell area, cell voltage, number of cells per stacks and the number of stacks, being 0.65 $A{\cdot}cm^{-2}$, 290 cm^2, 1.675 V, 60 cells and 1450 stacks, respectively. This results in a minimum power input of 27.5 MW. So, losses occur at low wind speeds when the rectifier power output is lower than 27.5 MW, as shown in Fig. 8.12.

The second factor is the small error between the rectifier output and PEME input as a result of the predefined polarization curve of the PEME for certain operating temperature and pressure conditions. These mismatches are insignificant during operation, as the losses are only around 0.02 MW. A temporarily shortage of power during the simulation occurs during start-up of the PEME, due to the transient temperature and pressure, which is clearly depicted in Fig. 8.12 at t = 300. The lower operating temperature, results in higher PEME voltage, which is not accounted for in the used polarization curve which is based on a constant operating temperature and pressure and only varies with the current density.

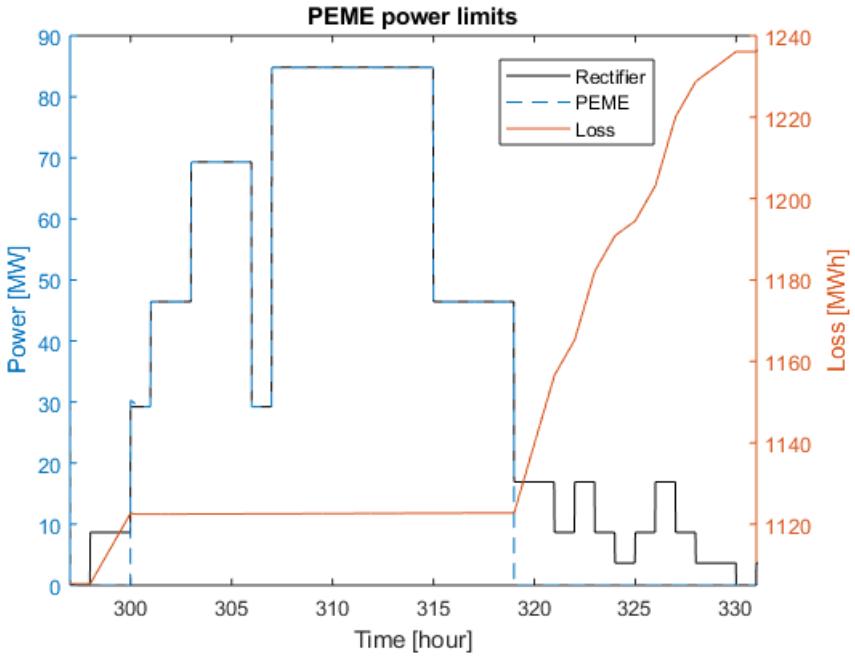

Figure 8.12: PEME power consumption and rectifier power output. The orange curve shows the power loss due to the power mismatch. (Case WT-CHEM)

The last factor is the error between the rectifier and PEME rated power. The rated power output of the rectifier is slightly higher than the rated power input of the PEME with the maximum error depending on the rated power output of a single turbine.

The influence of the different losses are represented by the orange curve where it is clear the power losses are greatest during low wind speeds when the rectifier output is lower than the minimum PEME power input. These losses can be minimized by operating the PEME as multiple independent units. That way the minimum power input per unit will be lower resulting in hydrogen production even at lower wind speeds. In Fig. 8.12, for example, the lower 4 rectifier outputs are approximately 3.7, 8.7, 16.9 and 29.2 MW. By operating the PEME as two units, the minimum power input per unit will be 27.5 MW/ 2 units = 13.75 MW. Meaning 50% of the PEME is operational during the third lowest wind speed. By using 4 independent units, the minimum power input is 6.9 MW, thus 25% is the PEME is operational during the second lowest wind speed. In order for an operational fraction of the PEME during the lowest wind speed, 8 units are needed as the minimum input will be 3.4 MW. In reality, a PEME is operated as multiple independent units, therefore, the power limit losses will not be as significant as in this study.

8.5 Case WT-CHEM: Transmission pipe flow

As explained in the modeling section, TP1 is modelled such that the outlet valve opens when the inlet flow is greater than zero. The outlet valve closes when the inlet flow is zero and the pipeline pressure has approximately returned to its initial value. Figure 8.13 shows the transient pressure and mass flow along the pipeline. The inlet mass flow is determined by the PEME outlet hydrogen flow. A constrained of the model is that the outlet pressure must always be approximately the initial pressure which is 90 bar in this case. It can be seen that the inlet pressure increases as the inlet valve opens and the mass flow enters the pipe. Due to the pressure difference, a mass flow along the pipe initiates resulting in a mass flow at the outlet.

At t = 8700, the inlet valve opens and a mass flow of around 0.18 kg·s^{-1} starts to flow. For this model, steady-state conditions (SSCs) are assumed when the inlet and outlet mass flow differ less than 0.001 g·s^{-1}. After about 2 hours at t = 8701.87, SSCs are reached. For the transition from the lowest to the second lowest mass flow at t = 8705, SSCs are reached after 2.5 hours at t = 8707.5. the other way around occurs at t = 8714, where SSCs are reached after 2 hours at t = 8716. This shows that for higher mass flows, it takes longer to reach SSCs. Also, SSCs are reached faster for a decrease in mass flow than for an equal increase in mass flow. Furthermore, when the inlet mass flow goes to zero again at t = 8719, the pressure curve shows a decreasing pressure drop whereas the outlet mass flow drops almost linearly.

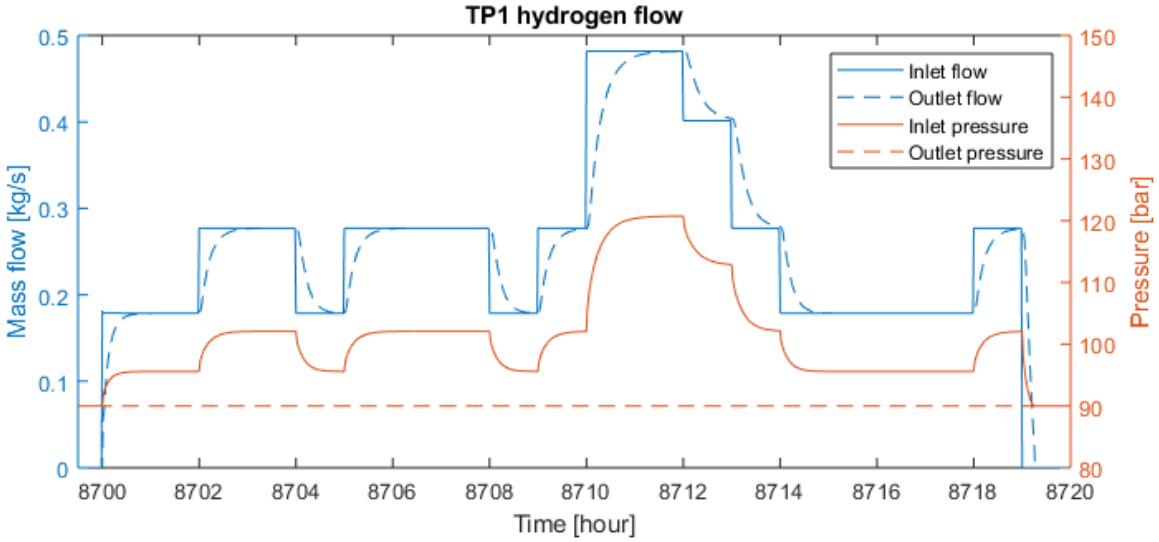

Figure 8.13: Thermodynamic properties of the hydrogen flow in TP1 between 8700 and 8720 hours. (Case WT-CHEM)

Figure 8.14 illustrates what the effect on the pipe flow is when the outlet valve closes. When this happens, the outlet mass flow drops to zero. At the same moment the outlet pressure increases, due to the momentum of the mass inside the pipe. The momentum direction is towards the pipe outlet, therefore, the inlet pressure drops under the outlet pressure as a sort of vacuum is created at the pipe inlet. This oscillation, can go on for a while depending on the amount of mass inside the pipe and the pipe pressure gradient. However, the temporal and spatial step also influence this oscillation in the mathematical domain. Here, these steps are quite large and the mass in the pipe is relatively low, thus the oscillation stops almost immediately. The average pipe pressure at rest is now slightly higher than the initial pressure. This is a result of the mass balance which accounts for the total mass that

entered and exited the pipe. The pipe pressure at rest is almost equal to the initial pressure, meaning that the algorithm controlling this pressure functions well.

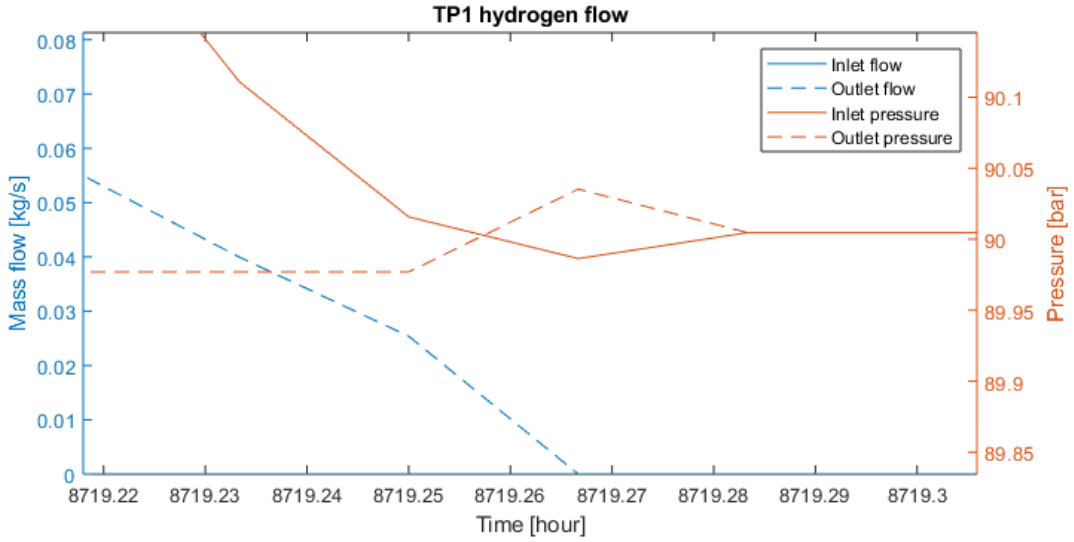

Figure 8.14: Close-up of Fig. 8.13 when the outlet valve closes at t = 8719.25. (Case WT-CHEM)

8.6 Case GD-PWR: Injection and discharge pipelines

The inlet of the discharge pipeline uses no valve in the model. When there is only injection into the cavern, the pressure inside the discharge pipe will increase resulting in a positive mass flow at the pipe inlet. Figure 8.15 depicts that before and after a discharge, the inlet and outlet pressures are not equal which is the result of the static pressure. The difference is only about 0.5 bar due to the low density of hydrogen. The difference between the inlet and outlet mass flows during discharge is relatively small due to the short length of the pipe. Furthermore, during steady outlet flow conditions, the inlet flow will always be slightly lower as the cavern pressure continuously decreases.

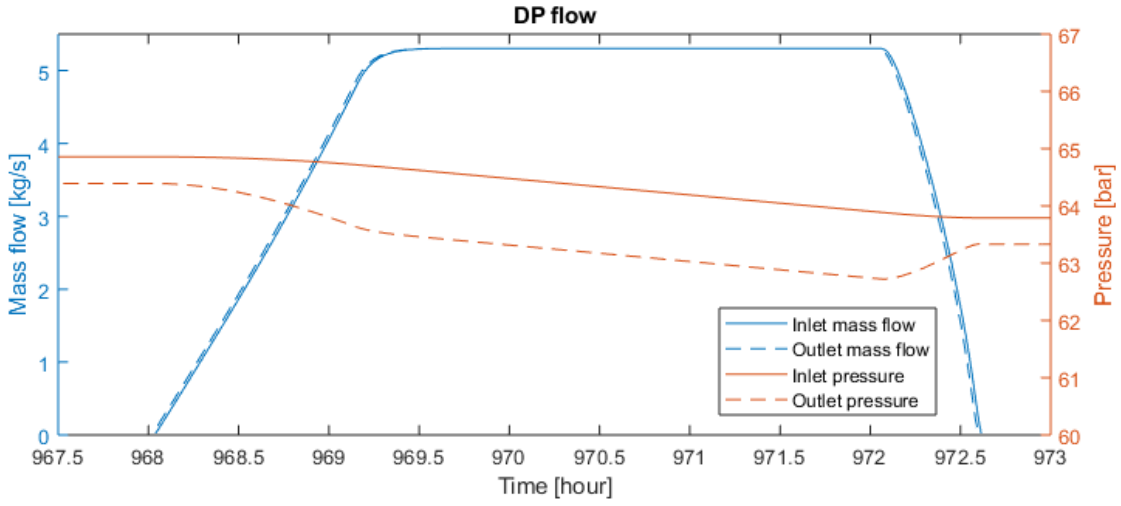

Figure 8.15: Flow properties for discharge pipeline (Case GD-PWR).

Figure 8.16 shows the flow properties along the injection pipeline. In the model, this pipe does not have an outlet valve. Here, also a pressure difference is present before and after the injection cycle. This pressure difference is larger than the one from the discharge pipe as the injection pipeline has a nozzle at the outlet. The nozzle is installed to ensure a sufficient flow into the cavern. The model uses a pressure reduction of 5 bar caused by the nozzle. The pressure difference, however, is 4.5 bar which is the result of the static pressure again.

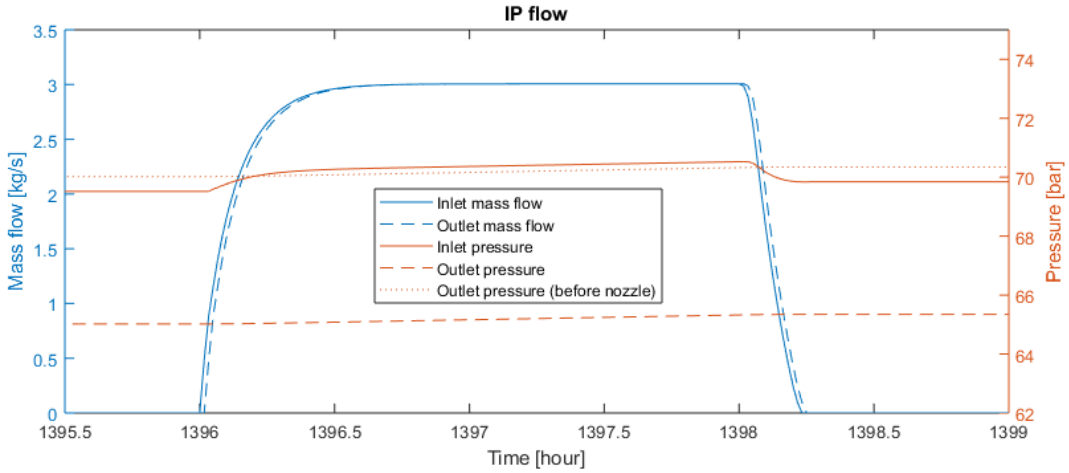

Figure 8.16: Flow properties for the injection pipeline (Case GD-PWR).

8.7 Case WT-PWR: PCSs

Figure 8.17 shows the pressure ratio and peak temperature of PCS 3 for 2017. Until around 5500 hours, the PCS will act as a pressure reduction station as the PR is below 1. During this period the temperature increases only slightly, with a maximum of 3.4°C at t = 1926 where the PR is lowest. This temperature increase is caused by the reverse Joule-Thompson effect. When the PR exceeds 1, the temperature increase due to compression via volume reduction is much more significant.

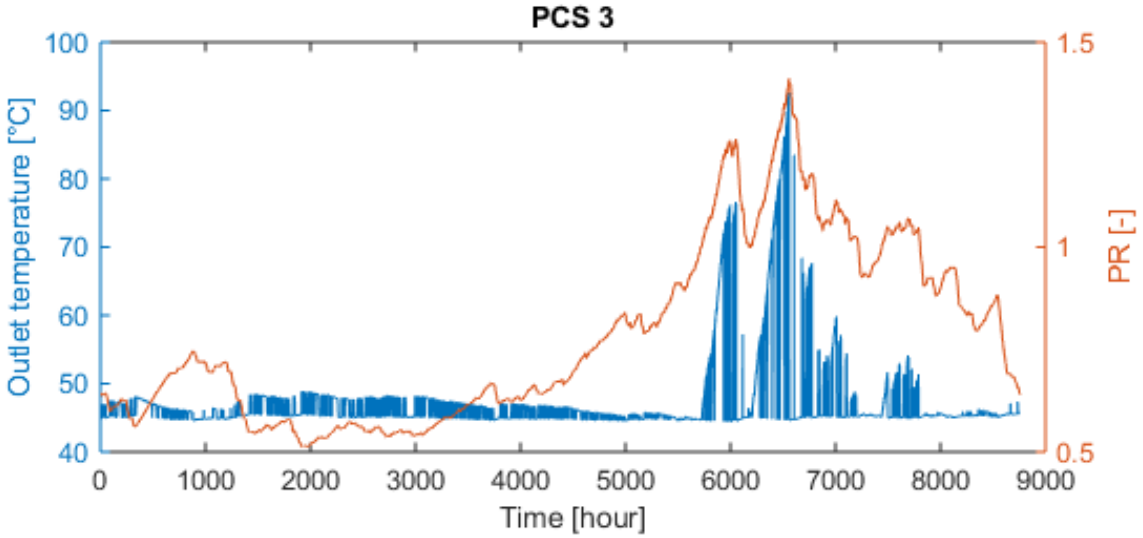

Figure 8.17: Pressure ratio and peak temperature of PCS 3 for 2017 (Case WT-PWR).

8.8 Case WT-PWR: Load control

Figure 8.18 show that the rated wind farm power output must be 11.5 times the base load power requirement of 100 MW. Even for such a large wind farm, the CCGT must still operate at two power output levels, namely 50.3 MW and the rated output of 100 MW. This is possible, as the CCGT is able to operate between 50 - 100% of its rated power output. However, at lower outputs the efficiency will decrease. Furthermore, the plot shows that the CCGT must also operate for shorter periods than 4 consecutive hours, which is not ideal as the CCGT experiences significant start-up and shut-down times. Also, during these start-up and shut down, the CCGT does not deliver the necessary power to meet the demand. In addition, the CCGT undergoes 433 on-off cycles which is much when compared to 51 of Case GD-PWR.

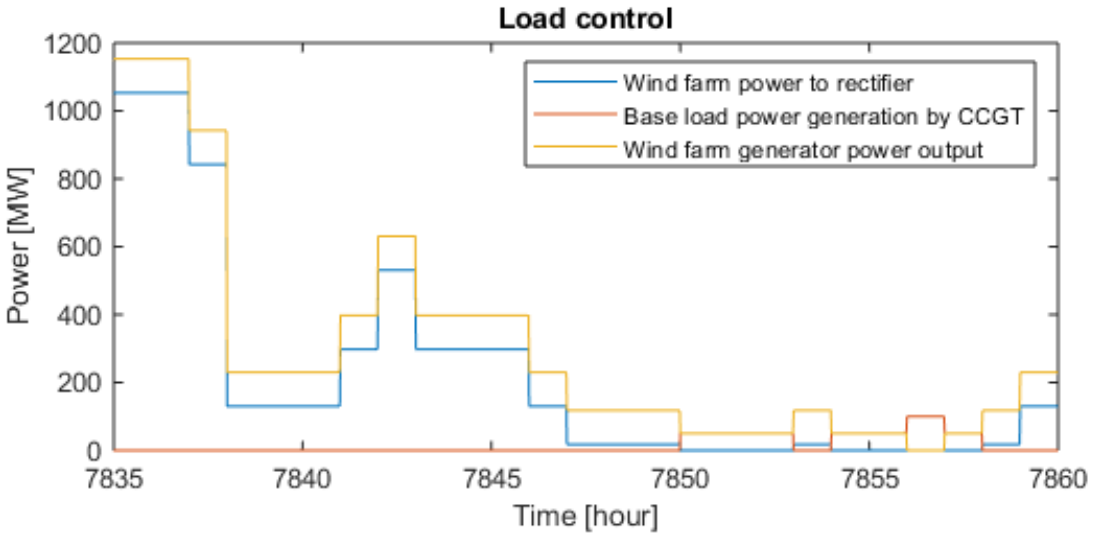

Figure 8.18: Load control (Case WT-PWR)

Besides the enormous wind farm, also a 1 GW PEME is needed in order to maintain a continuous output of 100 MW. Moreover, the wind farm, PEME and CCGT operate at relatively low CFs resulting in high operational costs. This case is more a hypothetical case to test the model as normally a power demand profile will not be constant, but highly fluctuating during the year.

However, this case can become more interesting when using fuel cells (FCs) instead of a CCGT. FCs are more efficient at power outputs below the rated power, whereas for CCGTs the opposite is true. Furthermore, the start-up and shut down time of FCs is negligible compared to CCGTs. Lastly, FCs operated at elevated pressure have higher efficiencies. Normally, pressurizing oxygen and hydrogen requires compression energy. However, in a system combined with a high pressure PEME, these are already produced at high pressure. This makes the overall system efficient in combination with a fuel cell.

8.9 Feasibility of Case GD-CHEM

8.9.1 Case GD-PWR

This case was meant to analyze the feasibility of a HES by looking at the power costs and revenue. Table 8.2 shows the costs and revenue of the HES based on electricity bought and sold for the time dependent spot price. All other costs like heat removal, maintenance, investment, salaries, feedstock, etc are not taken into account. Clearly, the PEME stacks have the highest power costs followed by the rectifier and then PCS1. For this case, the PEME operates when the spot price for power is equal or below 27.5 €·MWh^{-1} and the CCGT operates for prices equal or higher than 60 €·MWh^{-1}. The total profit amounts to €561,700. This shows that the system can be feasible. However, the profit margin, based on solely the power consumption, is only 5.6%. When considering all operational and investment costs, this margin will drop significantly. Furthermore, due to the spot price constraints on the PEME and the CCGT, the CFs are very low. Therefore, a large capacity must be installed in order to meet supply and demand.

Table 8.2: Costs and revenue (Case GD-PWR)

Parameter	Value	Unit
Rectifier	-1,004,600	€
PEME Stacks	-9,041,400	€
PEME BoP	-40,133	€
PC1	-121,910	€
PC2	-31,001	€
PC3	-12,111	€
PC4	-0	€
GT	+10,813,000	€
Profit	+561,700	€

Chapter 9

Comparison of the cases

This chapter gives a performance comparison of the 4 cases.

9.1 Power

Table 9.1 gives the performance results of 2017 of the 4 cases. The heat removal is a combination of the heat removed from the PEME and the 4 PCSs. Furthermore, the additional energy consumption for Case GD-CHEM and GD-PWR include the rectifier power consumption, whereas for Case WT-CHEM and WT-PWR this is not included as the rectifier is driven by the wind farm. The electrical power needed for the heat exchanger of the PCSs is not taken into account. Lastly, the HBS energy output gives the amount of chemical energy (LHV) that the outgoing hydrogen flow contains.

More power input is needed for Case WT-CHEM than for Case GD-CHEM even though the PEME is slightly more efficient. This is caused by the PEME power limits.

Table 9.1: Energy results.

Parameter	Case GD-CHEM	Case WT-CHEM	Case GD-PWR	Case WT-PWR	Unit
APX market	120.0	-	426.4	-	GWh
Wind farm power output	-	156.0	-	1,908	GWh
HBS energy input	120.0	156.0	426.4	1,355	GWh
PEME stacks (from primary source)	106.0	102.8	376.3	836.0	GWh
Additional energy consumption (grid)	14.0	2.0	50.1	18.9	GWh
Heat removal	2.0	2.0	7.5	16.7	GWh
HBS exergy destruction	41.8	79.9	149.1	739.3	GWh
HBS energy output	72.1	72.1	255.2	587.8	GWh

Table 9.2 shows the large differences between the rated power of the PEMEs. Case GD-CHEM and WT-CHEM have the same HBS energy output, but the PEME rated power for Case WT-CHEM must be three times larger due to the equally smaller CF. This multiplication factor also translates further to the first two PCSs as the rated mass flow is three times larger. Moreover, the difference between the CFs is a result of the different PEME operating modes and the low wind farm CF. As a result, the PEME must produce the same amount of hydrogen in less time. Furthermore, the peak PEME power for all cases is approximately 10% higher than the rated power, caused by the low start-up temperature.

Interesting to notice is the significant difference between the PEME CFs of Case GD-CHEM and GD-PWR caused by the spot prices of 35 and 27.5€·MWh^{-1}, respectively. This demonstrates that a

price increase of 35/27.5 = 27%, results is a CF increase of approximately 540%.

Table 9.2: Power values

Parameter	Case GD-CHEM	Case WT-CHEM	Case GD-PWR	Case WT-PWR	Unit
Wind farm power	-	117	-	1,428	MW
Wind farm CF	-	0.19	-	0.19	-
Rectifier power	34/31	-/85	650/588	-/947	MW (peak/rated)
PEME power	31/28	94/85	585/529	1,042/947	MW (peak/rated)
PEME CF	0.43	0.14	0.08	0.09	-
Compressor (PCS1)	0.35/0.34	1.24/1.24	7.18/ 7.18	13.75/13.74	MW (peak/rated)
Compressor (PCS2)	0.22/-	0.67/-	4.26/-	7.63/-	MW (peak/rated)
Compressor (PCS3)	0.05 /-	0.05 /-	3.95/-	1.08/-	MW (peak/rated)
Compressor (PCS4)	0/0	0/0	0/0	0/0	MW (peak/rated)
GT power	-	-	350	100	MW
GT CF	-	-	0.0458	0.3691	-

The low PEME and CCGT CFs of Case GD-PWR are the result of the APX spot price. The PEME operates solely at low spot prices and the CCGT at high spot prices, which only occur at limited times during the year, in order to make the system profitable. The profitability of this systems limits the output and increases the installed power.

The installed wind farm power for Case WT-PWR must be enormous in order to meet the 100 MW base load demand. The farm and the PEME must be more than 14 and 9 times larger than the base load, respectively. Furthermore, larger diameter pipelines and larger compressors are needed to transport the high flow rates which only occur for short time periods. Especially, the transport components between the PEME and the cavern must be large due to the low PEME CF. This makes Case WT-PWR in this configuration unrealistic as high investments are needed. To make this case more appealing, other turbines can be installed with a lower rated wind speed to reduce the rated power of the wind farm and the PEME. This also results in lower rated hydrogen flow rates, thus reducing the pipeline diameters and the rated power of the compressors.

The Swanky diagrams from Figs. 9.1 - 9.4 show that for the GD cases, the PEME consumes most power and for the WT cases, the PEME power limits consume most power. The PEME power limits consumption for Case WT-PWR is higher than for Case WT-CHEM, as Case WT-PWR only operates with 4 modes instead of five, so more power is lost in the low wind speed range. Furthermore, the before cavern (BC) and after cavern (AC) transport system only consumes 1.1 - 1.5% of the total power input.

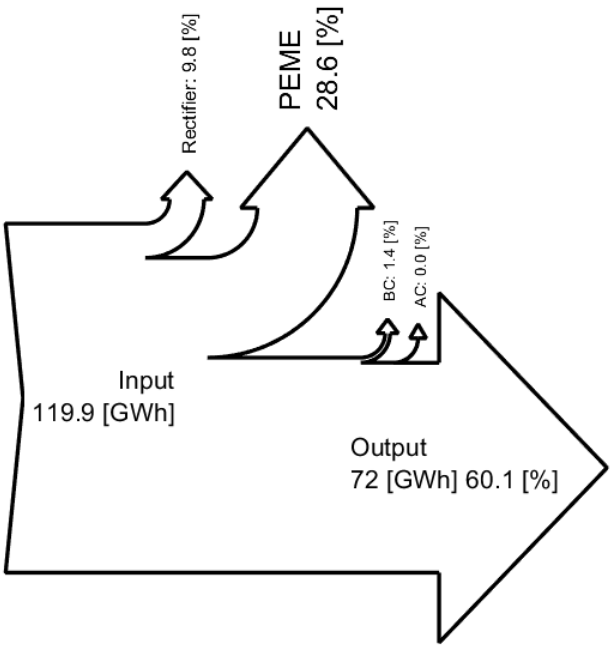

Figure 9.1: Power flow (Case GD-CHEM)

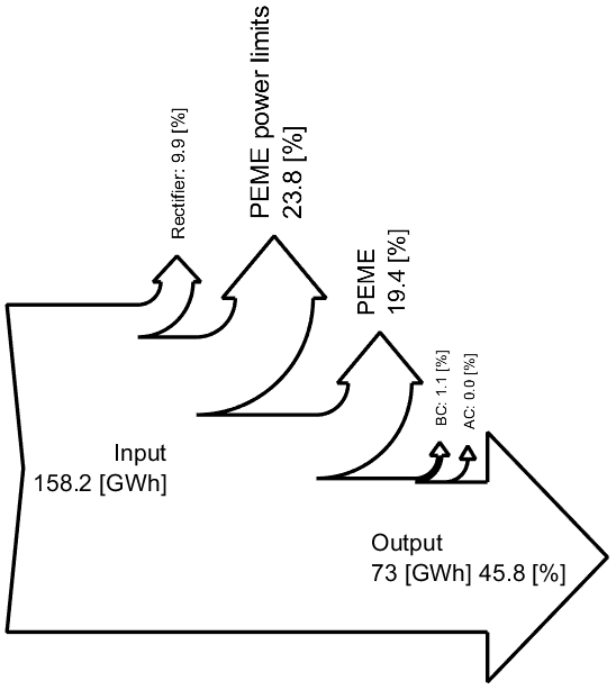

Figure 9.2: Power flow (Case WT-CHEM)

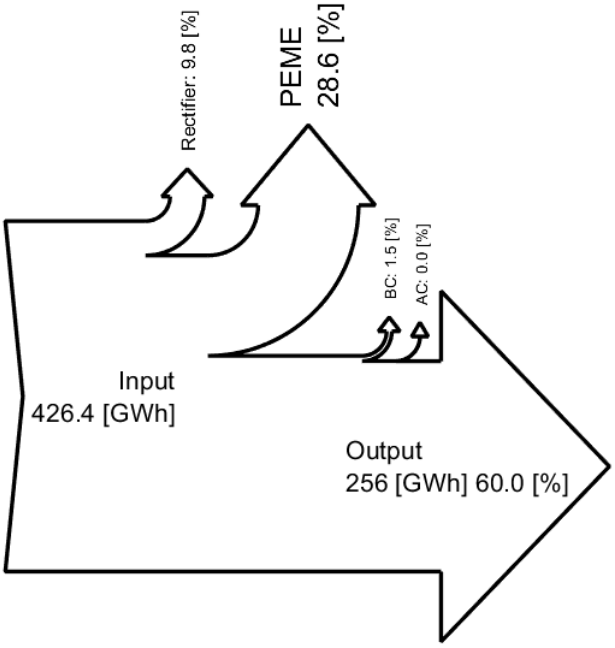

Figure 9.3: Power flow (Case GD-PWR)

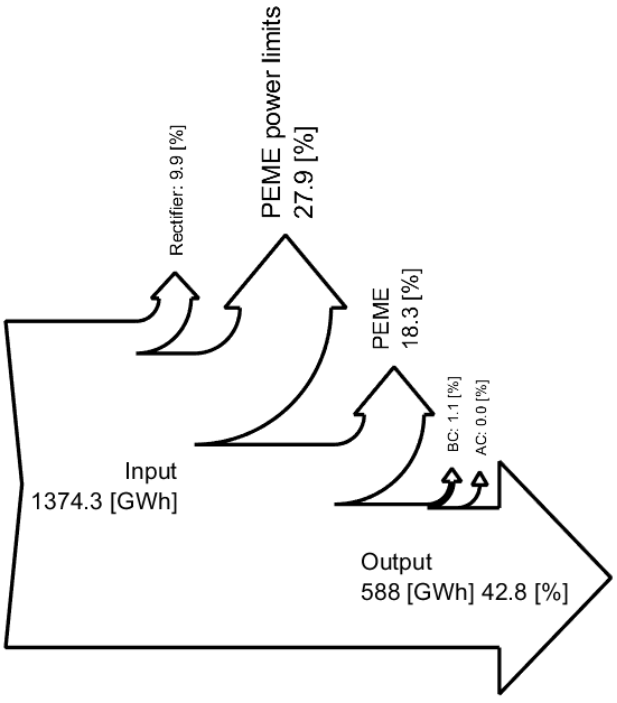

Figure 9.4: Power flow (Case WT-PWR)

9.2 Exergy

The results from Figs. 9.5 - 9.8 show that there are only slight differences in the exergy losses of the transport systems. For all cases, PCS 4 experiences the most significant exergy losses followed by PCS 1. The first are exergy losses due to throttling of the gas whereas the latter are due to the compression process. The exergy destruction in the pipelines is caused by friction with the pipe leading to a pressure drop along the pipe. The service transmission pipeline (TP2) shows a higher exergy destruction percentage than the transmission pipeline after the PEME (TP1), meaning that these pipelines experience more pressure losses along the pipe. Lastly, no significant differences between the cases are present.

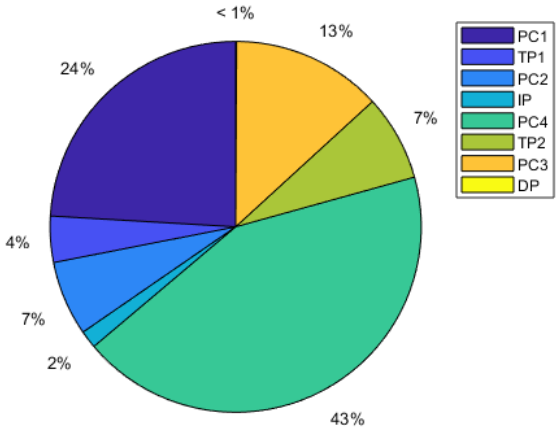

Figure 9.5: Exergy destruction (Case GD-CHEM)

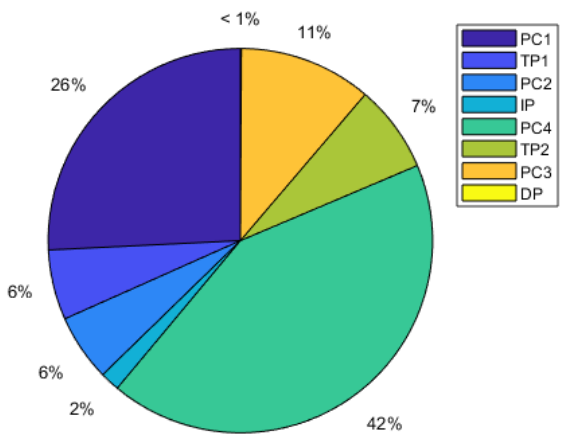

Figure 9.6: Exergy destruction (Case WT-CHEM)

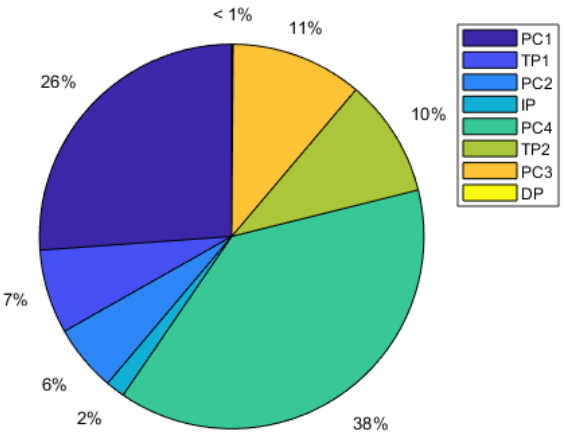

Figure 9.7: Exergy destruction (Case GD-PWR)

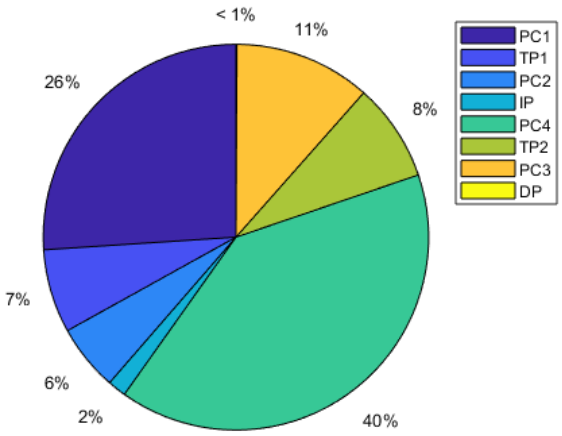

Figure 9.8: Exergy destruction (Case WT-PWR)

Figures 9.9 - 9.12 illustrate that exergy efficiency is higher than the power efficiency for all cases. The exergy efficiency considers the possible use of waste streams like heat and pressure flows. Especially, the BC exergy destruction percentage is significantly lower than its power consumption percentage as the energy of the waste heat flows can be used. The after cavern transportation system (AC), on the other hand, shows a higher percentage, because gas throttling has a significant impact on the exergy destruction as the energy is lost to entropy increase and only a small part is dissipated as heat. The PEME exergy efficiency considers the chemical and pressure energy than the oxygen flow at the

AGS contains and the waste heat. Around 5 % of the total input energy for the GD cases can be retrieved when effectively using waste streams. For the WT cases, 27.5-31.3% of the input energy can be retrieved when also including the PEME power limit losses.

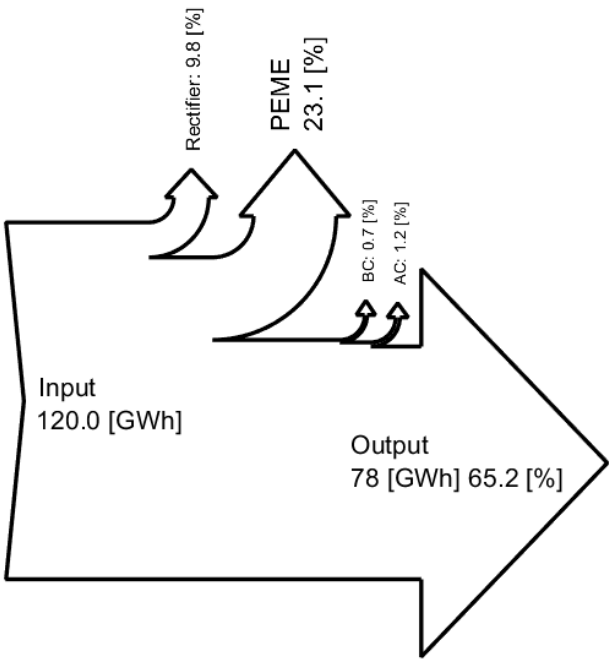

Figure 9.9: Exergy flow (Case GD-CHEM)

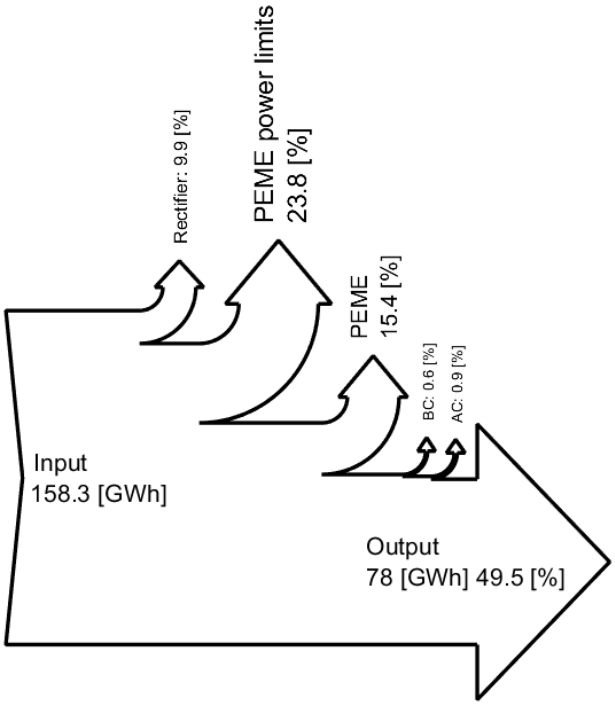

Figure 9.10: Exergy flow (Case WT-CHEM)

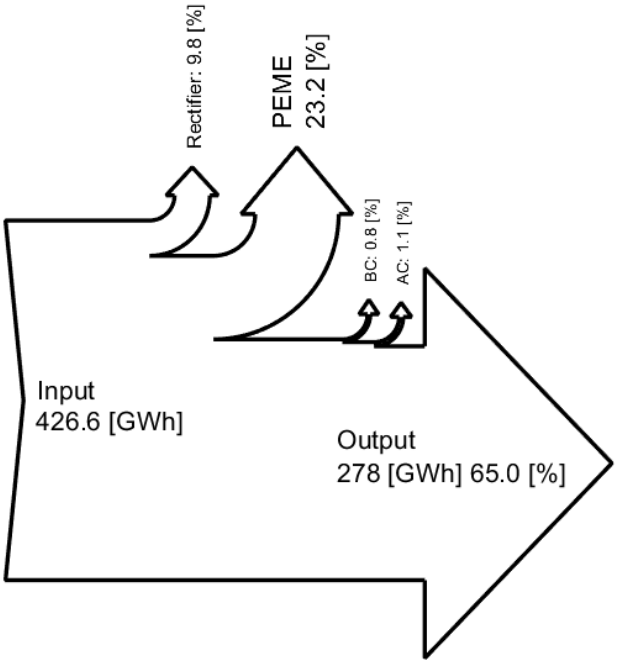

Figure 9.11: Exergy flow (Case GD-PWR)

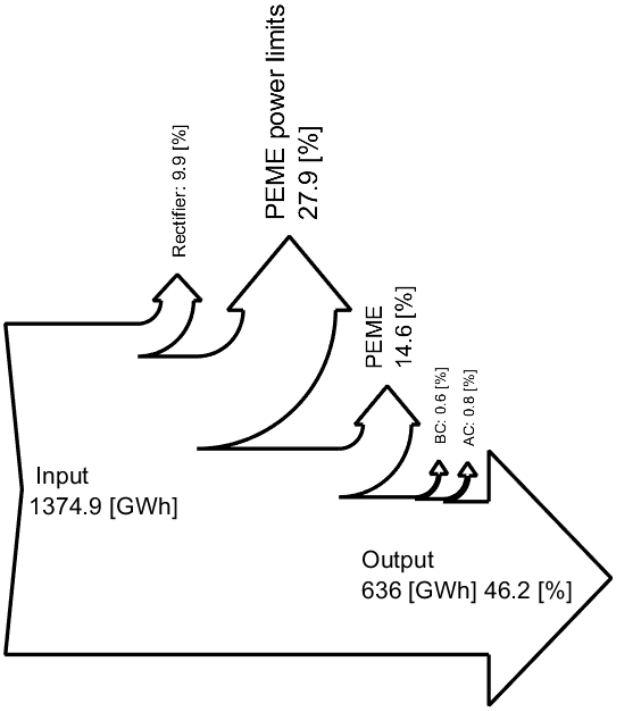

Figure 9.12: Exergy flow (Case WT-PWR)

9.3 Power-to-gas efficiency

The power-to-gas efficiencies of the HBSs are shown in Table 9.3. These values are lower than the power efficiencies from section 9.1 as these also take the necessary heat removal into account. These efficiencies, however, are only 1.8-2.1% lower, proving that the heat removal only has a small impact. The rectifier is assumed to have a constant efficiency resulting in identical results for all cases.

The PEME efficiency varies between 67.5-70.1% with an average value of 68.8%, making it the highest contributor to the HBS efficiency losses. The PEME operational limits only arise when wind is the energy source. So, for the WT cases, it is the second highest contributor to the efficiency losses with values between 68.5-73.2%.

PCS 1 and 2 are part of the before cavern transport system. The maximum efficiency differences of PCS 1 and 2 between the cases are only 0.37 and 0.1 percentage points, respectively. This proves that the PEME power source has a negligible effect on the before cavern transport system. The small differences are the result of the pipe diameter and the on-off switches of the PEME. The pipelines are sized for the system using the same constraints, however, small changes in the pipe diameter can have a significant impact on the pressure drop along the pipeline, as shown in section M. Smaller pipe diameters lead to larger pressure drops along the pipe. More on-off switches result in more transient periods with lower flow rates. Lower flow rates lead to less pressure drop along the pipeline resulting in relatively less compressor work.

For all cases, the efficiencies of PCS 3 and 4 show a maximum difference of 0.05 and 0.0 percentage points, respectively. So, the service of the HBS does not influence the system. Even though, Case GD-CHEM and WT-CHEM use a constant output flow rate and Case GD-PWR and WT-PWR use a highly fluctuating output flow rate. The negligible influence arises from the fact that the service pressure is always lower than TP2, so PCS 4 always functions as a throttling valve using no additional work. In addition, the DP pressure is for large part of the year lower than the cavern pressure. So, PCS 3 mostly functions as a throttling valve as well and only for a short period as a compressor with a low PR, resulting in minimum energy consumption.

Lastly, the two different maximum PEME operating spot prices of Case GD-CHEM and Case GD-PWR do not influence HBS power-to-gas efficiencies as these are equal. Reason for this, is that the PEME is scaled for the demand by adding or removing stacks and these all operate under the same conditions. The slightly lower PEME efficiency for Case GD-PWR is caused by the many on-off switches. Here, a lower temperature during start-up results in more voltage losses in the PEME.

Table 9.3: Power-to-gas efficiency of the HBS.

Parameter	Case GD-CHEM	Case WT-CHEM	Case GD-PWR	Case WT-PWR	Unit
Rectifier	0.90	0.90	0.90	0.90	-
PEME	0.6757	0.701	0.675	0.6985	-
PEME operational limits	-	0.732	-	0.6852	-
PCS 1	0.9663	0.9641	0.9627	0.9626	-
PCS 2	0.9927	0.9943	0.9941	0.9935	-
PCS 3	0.9945	0.9944	0.9943	0.9948	-
PCS 4	0.9998	0.9998	0.9998	0.9998	-
Total	0.58	0.44	0.58	0.41	-

Part IV

Chapter 10

Conclusion

Hydrogen-based energy systems (HESs) are seen as a promising replacement for fossil-based systems. These systems can make use of renewable energy sources resulting in less greenhouse gas emissions while delivering many different services like power, heating, cooling, transportation fuel and feedstock for the industry. The heart of a HES is the hydrogen back-up system (HBS) which is responsible for the production, transport and storage of hydrogen. This study is done to get a more thorough understanding in what way various sources and services influence the power-to-gas efficiency of a HBS. This efficiency considers all losses starting from the source power output until the service hydrogen input.

Two services are defined for the HES; Service 1: Constant hydrogen supply for the chemical industry and Service 2: Interruptible hydrogen supply as a fuel for power back-up. The chemical industry is a sector with a rapidly growing hydrogen demand and requires a constant hydrogen supply. Hydrogen as a fuel for power back-up using CCGTs is chosen as efforts are done to make power generation less polluting by using hydrogen instead of natural gas as a fuel for CCGTs. Furthermore, the power grid is more likely to get congested due to the rapidly increasing interruptible renewable power supply. A power back-up is able to balance the supply and demand of power. By using the second service, the HBS output will be intermittent. Both systems can either use a wind farm or the power grid as the source. The power input is determined by the wind speed or the spot price for power, respectively. The power output from a wind farm is highly fluctuating and more or less uncontrollable. For the grid cases, the instant of the power output depends on the spot price, but the magnitude is controllable. So, four cases are defined which all influence the HBS in various ways.

A literature survey determined that the large-scale, widespread HBS for this study will consist of a PEM electrolyzer (PEME), pipeline transport and salt cavern storage. This configuration results in scalable and highly pure hydrogen production with a quick response to the intermittent nature of the sources. Moreover, the hydrogen can be stored in sufficiently large quantities with an almost instantaneous delivery response to the demand of the services at distant locations.

A fully transient mathematical model of the system, built in Matlab® Simulink, was made for this study. This model uses a rectifier and a PEME to convert the source power into hydrogen. The PEME operates at 60°C and 35 bar and water is used as the only feedstock. A transport system consisting of a PCS and a 50 kilometre transmission pipeline, with an initial pressure of 90 bar, delivers the hydrogen to the cavern. The hydrogen is injected into a 1000 metre deep cavern by a PCS and an injection pipeline with nozzle. The cavern neglects mass losses and it is assumed that the cavern has an one metre thick shell after which the rock acts as a heat reservoir with a constant rock temperature of 45°C. A discharge pipeline is connected to a PCS which makes the hydrogen temperature and pressure

suitable for another 50 kilometre transmission pipeline with an initial pressure of 90 bar. A final PCS adjusts the flow properties to the desired service properties of 20 bar and 10°C for all cases. Isothermal flow is assumed in the pipelines using a constant temperature of 10°C. The PEME, pipelines and the salt cavern operate fully transient and are thus able to capture the intermittent nature of the cases.

Historical data of the spot prices for power and the wind speeds of 2017 are used for the sources and services. Simulations of the services determined the hydrogen demand per case for 2017. This was used to size the rest of the system components, ensuring full use of the cavern capacity without over- or underproduction and proper pipe flow. It demonstrated that all four systems were correctly sized and thus able to meet supply and demand at all times during the year with negligible over- or underproduction. The cavern sizes were calculated to be around 55,000 and 60,000 m^3 for the chemical industry (CHEM) cases and 942,000 and 792,000 m^3 for the power back-up (PWR) cases. However, Case GD-CHEM does not make full use of the cavern capacity and should have been slightly smaller. The cavern of Case WT-CHEM experiences a too high pressure gradient during some instances, therefore, the cavern should be larger or the rated power of the PEME should be lower. The significantly larger caverns for the PWR cases are a result of the much higher HBS output and the fact that no simultaneous injection and discharge takes place.

The full year simulations of the defined cases, using the same historical data, showed that the caverns only completed one full charge-discharge cycle, showing that all cases demand seasonal storage. For the GD cases, the caverns predominantly charge during the summer months, whereas for the WT cases, the caverns discharge during these months. This was a result of the capacity factors of the PEME and the service system during 2017. Stronger winds occur mostly in wintertime, resulting in a higher PEME capacity. Whereas, lower spot prices for power mostly occur in summertime leading to a higher PEME capacity factor during those months. Lastly, the cavern temperature fluctuation during the year is for all cases <1% which results in a negligible effect on the cavern pressure.

The power-to-gas efficiency of both the GD cases is 58%, whereas the WT cases have efficiencies of 44% and 41%. The main conclusions as to why these difference are present and how the efficiencies are governed by the sources and services are listed below.

- Wind-powered HBSs lead to roughly 24 - 28% more power losses due to a mismatch between the wind farm power output and the PEME operational power input limits. The most significant losses occur during low wind speeds when the wind farm output is between zero and the minimum PEME operating power. This loss is the main contributor to the differences in the power-to-gas efficiencies for all cases.
- The PEME efficiencies are in the range of 67.5 - 70.1%, making it the largest contributor to the total HBS losses.
- The transport and storage systems for all cases have an efficiency of roughly 95.0 - 95.5%.
- The efficiency of wind-powered PEMEs is 2.3 - 2.6 percentage points higher compared to grid-powered PEMEs as these have less voltage losses due to operation below the rated power.
- The service has no significant effect on the efficiency as the service pressure for all cases is for large part of the year lower than the transport and storage pressure, resulting in negligible power requirements for the transport system.

Furthermore, many start-up cycles, inherent to intermittent sources, only lead to an insignificant efficiency drop of around 0.1 percentage point as more losses occur at low operating temperatures. The

PCS directly after the PEME always operates as a compressor and consumes the most power of all the PCSs due to the relatively high pressure ratio (PR) throughout the year. Therefore, this PCS is mainly responsible for the transport and storage efficiency. All cases demand seasonal storage resulting long periods of high cavern pressure, increasing the transport power consumption thus lowering the total HBS efficiency.

The case where the source and service are both governed by the spot price (Case GD-PWR), simulated a non-renewable power back-up system. The results revealed that this system can be feasible when solely considering the buy and sell price of power. The feasibility, however, led to low capacity factors for the PEME and service. Furthermore, only a small profit margin of about 6% was realised which would drop significantly if all operational and capital costs were taken into account. Case WT-PWR simulated a dominantly renewable energy system supplying a constant base load of 100 MW. Around 63% of the base load is directly supplied by the wind farm. The rest is supplied via the indirect route which encounters the most significant losses. Due to the these losses and the low wind farm capacity factor, the wind farm and the PEME rated power must be more than 14 and 9 times the base load, respectively. Furthermore, a CCGT will not be suitable due to operating constraints on minimum operating time and ramp-up and ramp-down rates.

This study concluded that the power-to-gas efficiency of a wind-powered HBS is 14-17 percentage points lower compared to a grid-powered HBS due to the operational limits of a PEME despite the fact that the PEME efficiency itself is around 2.5 percentage points higher when using wind as the power source. In addition, the transport and storage system only accounts for 2-3% of the HBS power consumption of the HBS and the service does not have an influence at all.

Chapter 11

Recommendations

Improvements can be made in both the mathematical model and the operating conditions of the HBS. These findings are based the literature survey and model results.

11.1 Model improvements

Wind farm and rectifier For this study, not much attention was paid to the size and the power losses of the rectifier. However, the rectifier consumes almost 10% of the total power input of the HBS. The efficiency of the rectifier should depend on its input and output. The output is elaborately modeled, but the input, being the output of the wind farm or power grid, is very simplified.

For this study, the output of the wind farm is a simple AC power value and nothing is known about the characteristics of this signal. Therefore, also the wind farm model should be more complex. The performance coefficient and the gearbox efficiency should be variable values depending on the operating parameters. Also, a more realistic generator model should be incorporated to determine the generator efficiency and output power characteristics as a function of the operating parameters.

PEME The PEME should be operated in the model as multiple individual units in order to reduce the PEME power limit losses. This will also increase the PEME capacity factor. A battery can also be used to store the PEME power limit losses and use this during operation on top of the source input. This way, the PEME is able to produce hydrogen with power otherwise lost.

Transport of both oxygen and hydrogen through the PEME membrane is incorporated. This transport is influenced by the membrane permeability coefficients and the concentration gradient of the specific component. This study uses a constant value for the coefficients, but literature shows that these are influenced by the pressure, temperature and current density.

Lastly, the complexity of the BoP should be increased. For this study, some parts the BoP are kept relatively simple. However, this system is responsible for managing the pressure, temperature, water distribution and the hydrogen purity. Especially, the components responsible for purifying the hydrogen should be incorporated as these affect the PEME efficiency due to power consumption and hydrogen loss.

Compressors The compressors all make use of a constant isentropic efficiency. This assumption is not valid as the intermittent nature of the HES results in fluctuating mass flows and pressure ratios.

These affect the compressor efficiency.

Pipelines The pipeline model assumes isothermal flow. A more complete model should include the energy equation. This way the surrounding temperature and the pressure drop along the pipe can affect the flow temperature. However, it must be noted that the surrounding temperature fluctuations only have a small impact on the hydrogen temperature as the pipelines are buried underground. In addition, the Joule-Thompson coefficient for hydrogen is relatively small leading to a low temperature increase due to the pressure drop.

Salt cavern The salt cavern model should incorporate mass leakage. This leakage is a combination of leakage though the cavern walls, leakage from the compressor and the other above ground equipment and hydrogen loss due to reaction with other components inside the cavern. Moreover, contamination of hydrogen inside the cavern should incorporated as this means that additional equipment is needed to purify the hydrogen flow, resulting in more system losses.

For this study, the produced hydrogen is always injected into the cavern. This can lead to simultaneous injection and discharge of hydrogen. In reality, this is not possible as a single cavern only has one wellhead. Therefore, the model should make use of multiple connected or unconnected caverns. Another method is to let the produced hydrogen by-pass the cavern altogether and make direct injection into the service pipeline possible.

Adding a turbo-expander It can be interesting to investigate whether placing a turbo-expander after the salt cavern is feasible and able to increase the power-to-gas efficiency. In this case, it would be preferable that TP2 operates at an inlet pressure of 60 bar as this is equal to the minimum cavern pressure. Then, PCS 3 would only have to function as a pressure reduction station. This way, the maximum power can be recovered using a turbo-expander between the discharge pipeline and TP2. Apx. P substantiates that using a TP2 inlet pressure of 60 bar and a cavern pressure of 100 bar leads to a power recovery of around 0.5 MW while the flow temperature stays above the minimum of 10°C. Moreover, when recovering more power, the temperature will drop below the operating temperature of the pipelines. This can be prevented by using the waste heat from the before cavern PCS, wasting less energy.

Adding a fuel cell A power back-up system using a fuel cell should be investigated. Fuel cells are more efficient than CCGTs and are applicable in a broader operating range. Furthermore, the start-up and shut-down times are significantly less and the oxygen produced by the PEME can be used as a fuel reducing waste streams.

11.2 Operating conditions

PEME Section 4.3.10 showed that the PEME efficiency increases with increasing temperature. However, the implemented PEME model is not validated for temperatures above 60°C. Higher pressure leads to a lower PEME efficiency, but to a much lesser extent. Operating under high pressure, however, leads to a significant compressor work reduction of PCS 1. Therefore, more research should be done on the use of high temperature and pressure PEMEs.

Pipeline Additional research should be done on the operational pressure range and realistic lengths and diameters of hydrogen pipelines. Section 4.6.4 proved that the pressure drop is influenced by the

pipe length, diameter, operating pressure and flow temperature. Here, the trade-off between capital and operational costs is interesting, as these are influenced by the size and pressure drop.

Wind farm The chosen wind turbine type has a rated wind speed which is too high for this study. It is more beneficial to chose the turbine type by taking the average wind speed of the used location into account. This will both increase the wind farm and PEME capacity factor.

11.3 Costs

Case GD-PWR was meant to investigate the feasibility of a HES used for power back-up. Here, only the power consumption and production was taken into account. To make the feasibility study more realistic, all capital and operational costs should be considered. For this study, the sizes of the system components do not affect the hydrogen cost price. The components must increase in size when the capacity factor is low in order to ensure sufficient production, consumption, storage or transport. In reality, larger components result in higher installation costs which are the main contributor to the overall hydrogen costs (Olateju et al., 2016).

Furthermore, the waste streams should be used to boost the power-to-gas efficiency. Highly pure oxygen produced by a PEME with 99.99% purity is considered medical grade and could be sold for premium prices (Olateju et al., 2016). Lower purity could still be sold to retail vendors of industrial scale producers. When using fuel cells, the oxygen could be stored and delivered to the fuels cells to minimize feedstock costs. Waste heat could be used for heating surrounding industry or residential areas. Furthermore, the waste heat from PCS 3 could be used to heat up the flow after the turbo-expander if incorporated into the model.

References

Abanades, S., Charvin, P., Lemont, F., & Flamant, G. (2008). Novel two-step sno2/sno water-splitting cycle for solar thermochemical production of hydrogen. *International Journal of Hydrogen Energy*, *33*(21), 6021–6030.

Abdin, Z., Webb, C., & Gray, E. M. (2017). Modelling and simulation of an alkaline electrolyser cell. *Energy*, *138*, 316–331.

Abdullah, M. A., Yatim, A., Tan, C. W., & Saidur, R. (2012). A review of maximum power point tracking algorithms for wind energy systems. *Renewable and sustainable energy reviews*, *16*(5), 3220–3227.

Abe, J., Ajenifuja, E., & Popoola, O. (2019). Hydrogen energy, economy and storage: Review and recommendation. *International Journal of Hydrogen Energy*.

Acar, C., & Dincer, I. (2019). Review and evaluation of hydrogen production options for better environment. *Journal of Cleaner Production*.

Alavi, O., Mostafaeipour, A., & Qolipour, M. (2016). Analysis of hydrogen production from wind energy in the southeast of iran. *international journal of hydrogen energy*, *41*(34), 15158–15171.

Ali, D., Gazey, R., & Aklil, D. (2016). Developing a thermally compensated electrolyser model coupled with pressurised hydrogen storage for modelling the energy efficiency of hydrogen energy storage systems and identifying their operation performance issues. *Renewable and Sustainable Energy Reviews*, *66*, 27–37.

Andersson, J., & Grönkvist, S. (2019). Large-scale storage of hydrogen. *International Journal of Hydrogen Energy*.

Aouali, F. Z., Becherif, M., Ramadan, H. S., Emziane, M., Khellaf, A., & Mohammedi, K. (2017). Analytical modelling and experimental validation of proton exchange membrane electrolyser for hydrogen production. *International Journal of Hydrogen Energy*, *42*(2), 1366–1374.

Ayeng'o, S. P., Axelsen, H., Haberschusz, D., & Sauer, D. U. (2019). A model for direct-coupled pv systems with batteries depending on solar radiation, temperature and number of serial connected pv cells. *Solar Energy*, *183*, 120–131.

Ayodele, T., & Munda, J. (2019). Potential and economic viability of green hydrogen production by water electrolysis using wind energy resources in south africa. *International Journal of Hydrogen Energy*.

Bak, T., Nowotny, J., Rekas, M., & Sorrell, C. (2002). Photo-electrochemical properties of the tio2-pt system in aqueous solutions. *International journal of hydrogen energy*, *27*(1), 19–26.

Balat, M. (2008). Potential importance of hydrogen as a future solution to environmental and transportation problems. *International journal of hydrogen energy*, *33*(15), 4013–4029.

Bérest, P. (2019). Heat transfer in salt caverns. *International Journal of Rock Mechanics and Mining Sciences*, *120*, 82–95.

Bessarabov, D., & Millet, P. (2018). *Pem water electrolysis* (Vol. 1). Academic Press.

Betz, A. (1967). *Introduction to the theory of flow machines.(1966)(dg randall, trans.) oxford.* Pergamon Press.

Bünger, U., Michalski, J., Crotogino, F., & Kruck, O. (2016). Large-scale underground storage of

hydrogen for the grid integration of renewable energy and other applications. In *Compendium of hydrogen energy* (pp. 133–163). Elsevier.

Buttler, A., & Spliethoff, H. (2018). Current status of water electrolysis for energy storage, grid balancing and sector coupling via power-to-gas and power-to-liquids: A review. *Renewable and Sustainable Energy Reviews*, *82*, 2440–2454.

Carmo, M., & Stolten, D. (2019). Energy storage using hydrogen produced from excess renewable electricity: Power to hydrogen. In *Science and engineering of hydrogen-based energy technologies* (pp. 165–199). Elsevier.

Chen, H. L., Lee, H. M., Chen, S. H., Chao, Y., & Chang, M. B. (2008). Review of plasma catalysis on hydrocarbon reforming for hydrogen production—interaction, integration, and prospects. *Applied Catalysis B: Environmental*, *85*(1-2), 1–9.

Colebrook, C., & White, C. (1937). Experiments with fluid friction in roughened pipes. *Proceedings of the Royal Society of London. Series A-Mathematical and Physical Sciences*, *161*(906), 367–381.

Colombo, L., Corradini, M., Ippoliti, G., & Orlando, G. (2019). Pitch angle control of a wind turbine operating above the rated wind speed: A sliding mode control approach. *ISA transactions*.

David, M., Ocampo-Martínez, C., & Sánchez-Peña, R. (2019). Advances in alkaline water electrolyzers: A review. *Journal of Energy Storage*, *23*, 392–403.

Demirel, Y. (2013). *Nonequilibrium thermodynamics: transport and rate processes in physical, chemical and biological systems*. Newnes.

Devrim, Y., & Bilir, L. (2016). Performance investigation of a wind turbine–solar photovoltaic panels–fuel cell hybrid system installed at incek region–ankara, turkey. *Energy Conversion and Management*, *126*, 759–766.

Dincer, I., & Acar, C. (2017). Innovation in hydrogen production. *international journal of hydrogen energy*, *42*(22), 14843–14864.

Dixon, S. L., & Hall, C. (2013). *Fluid mechanics and thermodynamics of turbomachinery*. Butterworth-Heinemann.

Dooner, M., & Wang, J. (2019). Potential exergy storage capacity of salt caverns in the cheshire basin using adiabatic compressed air energy storage. *Entropy*, *21*(11), 1065.

Espinosa-López, M., Darras, C., Poggi, P., Glises, R., Baucour, P., Rakotondrainibe, A., ... Serre-Combe, P. (2018). Modelling and experimental validation of a 46 kw pem high pressure water electrolyzer. *Renewable Energy*, *119*, 160–173.

Falcão, D., & Pinto, A. (2020). A review on pem electrolyzer modelling: Guidelines for beginners. *Journal of Cleaner Production*, 121184.

Fang, R., & Liang, Y. (2019). Control strategy of electrolyzer in a wind-hydrogen system considering the constraints of switching times. *International Journal of Hydrogen Energy*, *44*(46), 25104–25111.

Fathabadi, H. (2016). Novel high efficient speed sensorless controller for maximum power extraction from wind energy conversion systems. *Energy Conversion and Management*, *123*, 392–401.

Gabrielli, P., Poluzzi, A., Kramer, G. J., Spiers, C., Mazzotti, M., & Gazzani, M. (2020). Seasonal energy storage for zero-emissions multi-energy systems via underground hydrogen storage. *Renewable and Sustainable Energy Reviews*, *121*, 109629.

García-Valverde, R., Espinosa, N., & Urbina, A. (2012). Simple pem water electrolyser model and experimental validation. *international journal of hydrogen energy*, *37*(2), 1927–1938.

Genç, M. S., Çelik, M., & Karasu, İ. (2012). A review on wind energy and wind–hydrogen production in turkey: A case study of hydrogen production via electrolysis system supplied by wind energy conversion system in central anatolian turkey. *Renewable and sustainable energy reviews*, *16*(9), 6631–6646.

Ghenai, C., & Bettayeb, M. (2019). Modelling and performance analysis of a stand-alone hybrid solar pv/fuel cell/diesel generator power system for university building. *Energy*, *171*, 180–189.

Gondal, I. (2016). Hydrogen transportation by pipelines. In *Compendium of hydrogen energy* (pp. 301–322). Elsevier.

González, A., Riba, J.-R., Rius, A., & Puig, R. (2015). Optimal sizing of a hybrid grid-connected photovoltaic and wind power system. *Applied Energy*, *154*, 752–762.

Guo, L., Zhao, L., Jing, D., Lu, Y., Yang, H., Bai, B., ... Wu, X. (2010). Reprint of: solar hydrogen production and its development in china. *Energy*, *35*(11), 4421–4438.

Haaland, S. E. (1983). Simple and explicit formulas for the friction factor in turbulent pipe flow.

Hangeragi, G. (2015). Modeling and control of a hybrid solar-wind power system with hydrogen storage. *International Journal on Emerging Technologies*, *6*(1), 98.

Helgaker, J. F. (2013). Modeling transient flow in long distance offshore natural gas pipelines.

Hwang, H. T., & Varma, A. (2014). Hydrogen storage for fuel cell vehicles. *Current Opinion in Chemical Engineering*, *5*, 42–48.

Ishaq, H., Dincer, I., & Naterer, G. F. (2018). Performance investigation of an integrated wind energy system for co-generation of power and hydrogen. *International Journal of Hydrogen Energy*, *43*(19), 9153–9164.

Ismail, T. M., Ramzy, K., Elnaghi, B. E., Abelwhab, M., & El-Salam, M. A. (2019). Using matlab to model and simulate a photovoltaic system to produce hydrogen. *Energy Conversion and Management*, *185*, 101–129.

Jafari, M., Armaghan, D., Mahmoudi, S. S., & Chitsaz, A. (2019). Thermoeconomic analysis of a standalone solar hydrogen system with hybrid energy storage. *International Journal of Hydrogen Energy*.

Kalinci, Y., Hepbasli, A., & Dincer, I. (2015). Techno-economic analysis of a stand-alone hybrid renewable energy system with hydrogen production and storage options. *international journal of hydrogen energy*, *40*(24), 7652–7664.

Khosravi, A., Koury, R., Machado, L., & Pabon, J. (2018). Energy, exergy and economic analysis of a hybrid renewable energy with hydrogen storage system. *Energy*, *148*, 1087–1102.

Kothari, R., Buddhi, D., & Sawhney, R. (2008). Comparison of environmental and economic aspects of various hydrogen production methods. *Renewable and Sustainable Energy Reviews*, *12*(2), 553–563.

Kumar, S. S., & Himabindu, V. (2019). Hydrogen production by pem water electrolysis–a review. *Materials Science for Energy Technologies*.

Li, C.-H., Zhu, X.-J., Cao, G.-Y., Sui, S., & Hu, M.-R. (2009). Dynamic modeling and sizing optimization of stand-alone photovoltaic power systems using hybrid energy storage technology. *Renewable energy*, *34*(3), 815–826.

Li, P., Hu, W., Hu, R., Huang, Q., Yao, J., & Chen, Z. (2019). Strategy for wind power plant contribution to frequency control under variable wind speed. *Renewable energy*, *130*, 1226–1236.

Liso, V., Savoia, G., Araya, S. S., Cinti, G., & Kær, S. K. (2018). Modelling and experimental analysis of a polymer electrolyte membrane water electrolysis cell at different operating temperatures. *Energies*, *11*(12), 3273.

Luskin, M. (1979). An approximation procedure for nonsymmetric, nonlinear hyperbolic systems with integral boundary conditions. *SIAM Journal on Numerical Analysis*, *16*(1), 145–164.

Makridis, S. (2017). Hydrogen storage and compression. *arXiv preprint arXiv:1702.06015*.

Maton, J.-P., Zhao, L., & Brouwer, J. (2013). Dynamic modeling of compressed gas energy storage to complement renewable wind power intermittency. *International Journal of Hydrogen Energy*, *38*(19), 7867–7880.

Mohammadi, A., & Mehrpooya, M. (2018). A comprehensive review on coupling different types of electrolyzer to renewable energy sources. *Energy*, *158*, 632–655.

Moradi, R., & Groth, K. M. (2019). Hydrogen storage and delivery: review of the state of the art technologies and risk and reliability analysis. *International Journal of Hydrogen Energy*.

Moran, M. J., Shapiro, H. N., Boettner, D. D., & Bailey, M. B. (2010). *Fundamentals of engineering thermodynamics*. John Wiley & Sons.

Moslehi, S., Reddy, T. A., & Katipamula, S. (2018). Evaluation of data-driven models for predicting solar photovoltaics power output. *Energy*, *142*, 1057–1065.

Muyeen, S., Takahashi, R., & Tamura, J. (2011). Electrolyzer switching strategy for hydrogen generation from variable speed wind generator. *Electric Power Systems Research*, *81*(5), 1171–1179.

Nematollahi, O., Alamdari, P., Jahangiri, M., Sedaghat, A., & Alemrajabi, A. A. (2019). A techno-economical assessment of solar/wind resources and hydrogen production: A case study with gis maps. *Energy*, *175*, 914–930.

Ni, M., Leung, D. Y., Leung, M. K., & Sumathy, K. (2006). An overview of hydrogen production from biomass. *Fuel processing technology*, *87*(5), 461–472.

Nicoletti, G., Arcuri, N., Nicoletti, G., & Bruno, R. (2015). A technical and environmental comparison between hydrogen and some fossil fuels. *Energy Conversion and Management*, *89*, 205–213.

Nikolaidis, P., & Poullikkas, A. (2017). A comparative overview of hydrogen production processes. *Renewable and sustainable energy reviews*, *67*, 597–611.

Ogunjuyigbe, A., Ayodele, T., & Adetokun, B. (2017). Steady state analysis of wind-driven self-excited reluctance generator for isolated applications. *Renewable energy*, *114*, 984–1004.

Olateju, B., Kumar, A., & Secanell, M. (2016). A techno-economic assessment of large scale wind-hydrogen production with energy storage in western canada. *International Journal of Hydrogen Energy*, *41*(21), 8755–8776.

Olivier, P., Bourasseau, C., & Bouamama, B. (2016). Modelling, simulation and analysis of a pem electrolysis system. *IFAC-PapersOnLine*, *49*(12), 1014–1019.

Olivier, P., Bourasseau, C., & Bouamama, P. B. (2017). Low-temperature electrolysis system modelling: A review. *Renewable and Sustainable Energy Reviews*, *78*, 280–300.

Orhan, M. F., Dincer, I., & Rosen, M. A. (2008). Energy and exergy assessments of the hydrogen production step of a copper–chlorine thermochemical water splitting cycle driven by nuclear-based heat. *International Journal of Hydrogen Energy*, *33*(22), 6456–6466.

Özgirgin, E., Devrim, Y., & Albostan, A. (2015). Modeling and simulation of a hybrid photovoltaic (pv) module-electrolyzer-pem fuel cell system for micro-cogeneration applications. *International journal of hydrogen energy*, *40*(44), 15336–15342.

Papadopoulos, V., Desmet, J., Knockaert, J., & Develder, C. (2018). Improving the utilization factor of a pem electrolyzer powered by a 15 mw pv park by combining wind power and battery storage–feasibility study. *International Journal of Hydrogen Energy*, *43*(34), 16468–16478.

Rekioua, D., Bensmail, S., & Bettar, N. (2014). Development of hybrid photovoltaic-fuel cell system for stand-alone application. *International Journal of Hydrogen Energy*, *39*(3), 1604–1611.

Ripepi, G. (2018). Hydrogen storage for variable renewable electricity integration: techno-economic analysis of a lined rock cavern system.

Saadat-Targhi, M., Khadem, J., & Farzaneh-Gord, M. (2016). Thermodynamic analysis of a cng refueling station considering the reciprocating compressor. *Journal of natural gas science and engineering*, *29*, 453–461.

Sangwine, S. (2018). *Electronic components and technology*. CRC press.

Sapountzi, F. M., Gracia, J. M., Fredriksson, H. O., Niemantsverdriet, J. H., et al. (2017). Electrocatalysts for the generation of hydrogen, oxygen and synthesis gas. *Progress in Energy and Combustion Science*, *58*, 1–35.

Saravanamuttoo, H. I., Rogers, G. F. C., & Cohen, H. (2001). *Gas turbine theory*. Pearson Education.

Sartory, M., Wallnöfer-Ogris, E., Salman, P., Fellinger, T., Justl, M., Trattner, A., & Klell, M. (2017).

Theoretical and experimental analysis of an asymmetric high pressure pem water electrolyser up to 155 bar. *International Journal of Hydrogen Energy*, *42*(52), 30493–30508.

Sdanghi, G., Maranzana, G., Celzard, A., & Fierro, V. (2019). Review of the current technologies and performances of hydrogen compression for stationary and automotive applications. *Renewable and Sustainable Energy Reviews*, *102*, 150–170.

Sharifian, S., Asasian Kolur, N., & Harasek, M. (2019). Transient simulation and modeling of photovoltaic-pem water electrolysis. *Energy Sources, Part A: Recovery, Utilization, and Environmental Effects*, 1–11.

Singh, S., Jain, S., Venkateswaran, P., Tiwari, A. K., Nouni, M. R., Pandey, J. K., & Goel, S. (2015). Hydrogen: A sustainable fuel for future of the transport sector. *Renewable and Sustainable Energy Reviews*, *51*, 623–633.

Smolinka, T., Ojong, E. T., & Garche, J. (2015). hydrogen production from renewable energies—electrolyzer technologies. In *Electrochemical energy storage for renewable sources and grid balancing* (pp. 103–128). Elsevier.

Tawfiq, K. B., Mansour, A. S., Ramadan, H. S., Becherif, M., & El-kholya, E. (2019). Wind energy conversion system topologies and converters: Comparative review. *Energy Procedia*, *162*, 38–47.

Tijani, A. S., Yusup, N. A. B., & Rahim, A. A. (2014). Mathematical modelling and simulation analysis of advanced alkaline electrolyzer system for hydrogen production. *Procedia Technology*, *15*, 798–806.

Toghyani, S., Fakhradini, S., Afshari, E., Baniasadi, E., Jamalabadi, M. Y. A., & Shadloo, M. S. (2019). Optimization of operating parameters of a polymer exchange membrane electrolyzer. *International Journal of Hydrogen Energy*, *44*(13), 6403–6414.

Torreglosa, J. P., García, P., Fernández, L. M., & Jurado, F. (2015). Energy dispatching based on predictive controller of an off-grid wind turbine/photovoltaic/hydrogen/battery hybrid system. *Renewable Energy*, *74*, 326–336.

Ulleberg, Ø. (2003). Modeling of advanced alkaline electrolyzers: a system simulation approach. *International journal of hydrogen energy*, *28*(1), 21–33.

Ursua, A., Gandia, L. M., & Sanchis, P. (2011). Hydrogen production from water electrolysis: current status and future trends. *Proceedings of the IEEE*, *100*(2), 410–426.

Valverde-Isorna, L., Ali, D., Hogg, D., & Abdel-Wahab, M. (2016). Modelling the performance of wind–hydrogen energy systems: Case study the hydrogen office in scotland/uk. *Renewable and Sustainable Energy Reviews*, *53*, 1313–1332.

van Wijk, A., & Chatzimarkakis, J. (2020). Green hydrogen for a european green deal a 2x40 gw initiative. , 8.

Veziroğlu, T. N., Şahi, S., et al. (2008). 21st century's energy: Hydrogen energy system. *Energy conversion and management*, *49*(7), 1820–1831.

Vivas, F., De las Heras, A., Segura, F., & Andújar, J. (2018). A review of energy management strategies for renewable hybrid energy systems with hydrogen backup. *Renewable and Sustainable Energy Reviews*, *82*, 126–155.

Wang, P., Yu, B., Deng, Y., & Zhao, Y. (2015). Comparison study on the accuracy and efficiency of the four forms of hydraulic equation of a natural gas pipeline based on linearized solution. *Journal of Natural Gas Science and Engineering*, *22*, 235–244.

White, F. M. (2003). Fluid mechanics, chapter 9. *McGraw-Hill, New York, NY*, *10020*, 630–721.

Winterbone, D., & Turan, A. (2015). *Advanced thermodynamics for engineers*. Butterworth-Heinemann.

Witkowski, A., Rusin, A., Majkut, M., & Stolecka, K. (2017). Comprehensive analysis of hydrogen compression and pipeline transportation from thermodynamics and safety aspects. *Energy*, *141*, 2508–2518.

Wolf, E. (2015). Large-scale hydrogen energy storage. In *Electrochemical energy storage for renewable sources and grid balancing* (pp. 129–142). Elsevier.

Yang, C., & Ogden, J. (2007). Determining the lowest-cost hydrogen delivery mode. *International Journal of Hydrogen Energy*, *32*(2), 268–286.

Yigit, T., & Selamet, O. F. (2016). Mathematical modeling and dynamic simulink simulation of high-pressure pem electrolyzer system. *International Journal of Hydrogen Energy*, *41*(32), 13901–13914.

Appendices

Appendix A

Current and future hydrogen projects in The Netherlands

Currently tremendous amounts of research is being done concerning the future of HRESs. When looking nationally at The Netherlands, some interesting projects are currently ongoing and planned. The energy and infrastructure company Gasunie plays a key role in some of the largest Dutch projects. For instance, the HyStock project[1], the first power-to-gas facility in The Netherlands from Gasunie, New Energy and EnergyStock, aims to convert renewable energy into hydrogen for transport and industry. The 1 MW facility is perfectly situated between a high-voltage electricity grid and the main gas transport grid. The power-to-gas installation consists of a power supply unit, an electrolyzer unit and buffer tank, a compressor that fills the mobile storage cylinders and a dispenser panel. The mobile cylinders are capable of being transported to end-users. This facility was ready for operation as of May 2019. In 2020 the first hydrogen filling station for individuals will be available in the northern part of The Netherlands. Moreover, this location has enormous salt caverns which are planned to be used in 2024 for large-scale hydrogen storage. The next step is building a 20-30 MW electrolyzer[2] for the Chemiepark Delftzijl together with Nouryon[3]. This location is ideal due to the large-scale production and import of renewable electricity. Furthermore, a collaboration of Gasunie with energy company ENGIE[4] are planning to build a 100 MW electrolyzer system[5] driven by wind energy in the northern part of The Netherlands by 2023.

The North Sea Wind Power Hub[6] will be an island in the North Sea where large-scale offshore wind power will be connected to a central hub where new energy highways and trade corridors can be created between countries. A centralized hub will greatly reduce the energy costs. The hubs will contain power-to-gas facilities where hydrogen will be produced and stored to balance and stabilize power transmission to onshore markets. This hydrogen can be converted back to power on-site or it can be transported via pipelines to the mainland.

[1] https://www.energystock.com/about-energystock/the-hydrogen-project-hystock
[2] https://www.gasunienewenergy.nl/projecten/20mw-elektrolyse-installatie-delfzijl
[3] https://www.nouryon.com/
[4] https://www.engie-energie.nl
[5] https://www.gasunie.nl/nieuws/gasunie-en-engie-gaan-samenwerken-om-groene-waterstof-op-grote-schaal-mogelijk-te-maken
[6] https://northseawindpowerhub.eu/

Appendix B

Hydrogen

Table B.1: LHV and HHV of hydrogen and some common fuels at NTP unless stated differently (Abe et al., 2019; Hwang & Varma, 2014).

Parameter	LHV [MJ·kg^{-1}]	HHV [MJ·kg^{-1}]	Density [kg·m^{-3}]
Gaseous hydrogen	119.96	141.88	0.0813
Liquid hydrogen	120.04	141.77	71.1033[1]
LNG	48.62	55.19	423.1120[2]
Natural gas	47.13	52.21	0.6483
Propane	46.28	50.22	1.8077
Conventional gasoline	43.44	46.52	720-780
Conventional diesel	42.78	45.56	-
Coal (wet basis)	22.73	23.96	-
Ethanol	26.95	29.84	785.4696
Methanol	20.09	22.88	786.3254
Forest residue	15.40	16.47	-

The energy storage capacity, meaning the heating value[3], of hydrogen is superb compared to most convectional fuels, as shown in Table B.1.

Figure B.1[4] shows that, at atmospheric pressure, hydrogen is a liquid below its boiling point of -253°C and a solid below its melting point of -259°C. The gas phase, however, covers a wide range of conditions making a storage system less prone to hydrogen condensation (Ripepi, 2018).

[3]https://h2tools.org/hyarc/calculator-tools/lower-and-higher-heating-values-fuels
[4]https://hydropole.ch/en/hydrogen/abouth2/

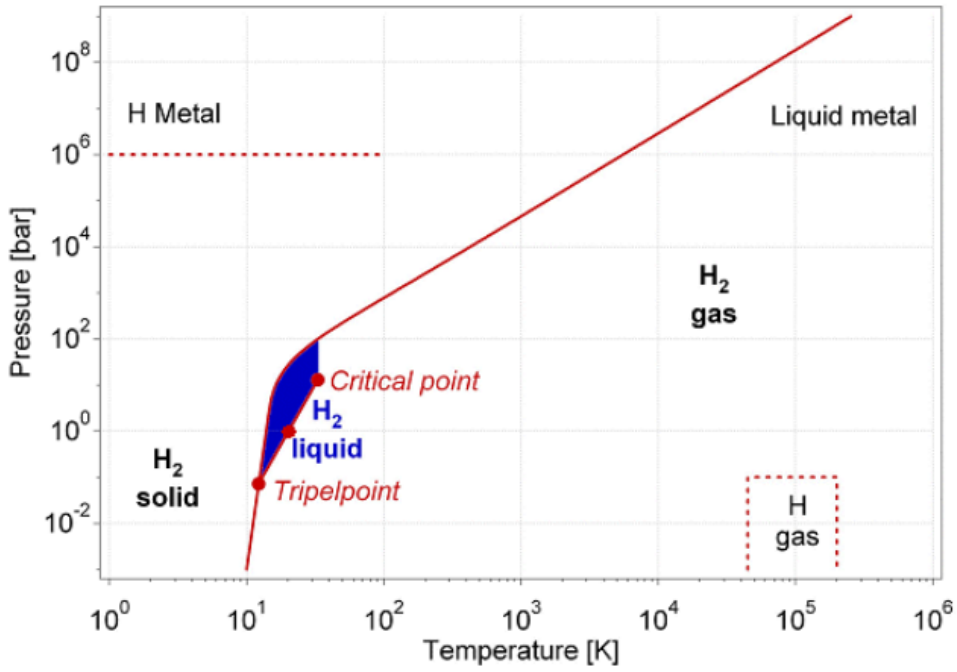

Figure B.1: Phase diagram of hydrogen.

B.1 Safety

Hydrogen is a promising candidate for replacing polluting fossil fuels with regards to fuel safety. Of course, hydrogen also poses risks if not properly handled. Table B.2 gives physio-chemical properties of hydrogen gas, gasoline and methane gas which are relevant when accessing the safety of a fuel.

Table B.2: Fire hazard related characteristics of fuels (Singh et al., 2015; Balat, 2008).

Parameter	Hydrogen	Methane	Gasoline	Unit
Mass density at STP	0.09	0.72	720-780 (liquid)	$kg^2 \cdot Nm^{-3}$
Diffusion coefficient in air at NTP	0.610	0.16	0.05	$cm^2 \cdot s^{-1}$
Specific heat at constant pressure at NTP	14.29	2.22	1.2	$cm^2 \cdot s^{-1}$
Ignition limits in air	4.0-75.0	5.3-15.0	1.0-7.6	vol%
Ignition energy (stoichiometric)	0.02	0.29	0.24	mJ
Ignition temperature	585	540	228-471	°C
Flame temperature in air	2045	1875	2197	°C
Explosion energy[5]	0.17	0.19	0.25	g TNT$\cdot$kJ^{-1}
Flame emissivity	17-25	25-33	34-43	%

The extremely small size of hydrogen, low molecular weight and low viscosity lead to much higher diffusion rates through solid materials compared to the other fuels. This results in decarburization and embrittlement of the material leading to potential failure of the components. This is a serious concern during the transportation and storage of hydrogen. The effects are enhanced under elevated temperatures and pressures, therefore, proper material selection is required to prevent component

[5]Theoretical maximum; actual 10% of theoretical.

failure.

The boiling points show that both hydrogen and methane are gasses under NTP whereas gasoline is a liquid.

The table also shows that hydrogen is highly diffusive in air compared to the other fuels and it is highly buoyant. These two effects result in rapid mixing with the surrounding air upon release or an accidental leak which will make it less concentrated in open spaces and thus less hazardous. However, in confined spaces a hydrogen leak can, for instance, result in accumulation of hydrogen gas under a roof leading to flammable mixtures.

Hydrogen has by far the the widest range of flammability. Meaning, that hydrogen will burn at both low and high concentrations. For using it as a fuel this is an advantage, because of the wide operating range. However, during leaks it is a potential hazard.

The detonation limit of hydrogen is wider than that of other fuels. Detonation is a type of combustion where the propagation of an exothermic front travels at supersonic speeds through a medium which will eventually accelerate to drive a shock front. However, in unconfined spaces it is very difficult to detonate hydrogen due to the high buoyancy and diffusion rate in air.

The minimum ignition energy that is needed to ignite the most easily ignitable concentration of hydrogen in air is a factor 10 lower than that of methane and gasoline. In practice, however, this would not make much of a difference with regards to fuel safely as a static spark of a person (10 mJ) is already enough to detonate any other flammable gas mixture. The auto-ignition temperature, which is the minimum temperature of a hot surface to ignite a flammable mixture, of hydrogen is around two times higher than that of gasoline, but does not differ significantly with methane.

The high burning speed increases the probability that a hydrogen flame evolves in deflagration or detonation. Deflagration is the propagation of a combustion front at subsonic speeds driven by heat transfer.

Furthermore, the explosion range is greatest of hydrogen, but it will become deflagrating for higher volumetric concentrations. Lastly, it burns with low submissiveness, therefore, hydrogen will be consumed rapidly with limited damage to its surroundings (Abe et al., 2019).

It can be concluded that hydrogen scores best on almost all fronts of the fire hazard related characteristics, except for the ignition limit and energy and the flame temperature (Veziroğlu, Şahi, et al., 2008). Lastly, the product of combustion of hydrogen is water which is not harmful to the environment.

Appendix C

Hydrogen production technology overview

Hydrogen production technologies can be classified into five fundamental processes which only use one conversion mechanism namely biological, electrical, thermal, chemical and photonic processes. However, combinations of two or more conversion mechanisms are also possible like electrochemical, electrothermal, thermochemical, photochemical and photoelectrochemical processes (Acar & Dincer, 2019). In literature, it is also common to classify the hydrogen production methods based on the used energy source, resulting in two main categories, namely hydrogen production based on fossil fuels or renewable energy (Nikolaidis & Poullikkas, 2017). All the different technologies are shown in Fig. C.1, giving a total of 14 hydrogen production methods.

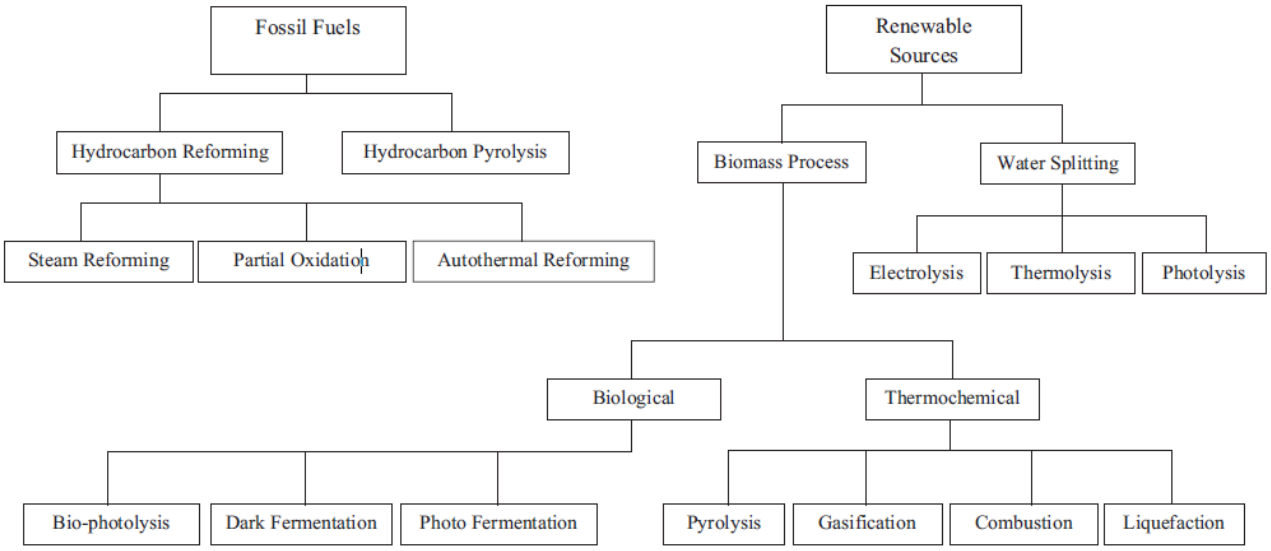

Figure C.1: Overview of hydrogen production technologies categorized on energy source.

Table C.1 gives a summary of the hydrogen production technologies. Steam reforming, partial oxidation and auto-thermal reforming are the most developed technologies with existing infrastructures and high efficiencies. However, all these technologies depend on the use of fossil fuels which results in unwanted greenhouse gas (GHG) emissions. Hydrocarbon pyrolysis is, in contrast to the former technologies, emission-free and needs less process steps, but it still depends on fossil fuels, resulting

in carbon as a by-product.

Pyrolysis and biomass gasification are both CO_2-neutral, because all CO_2 that is released during the process was captured by the organic material itself. Furthermore, the feedstock is cheap and abundantly available. However, the hydrogen production is highly dependent on the quality of the feedstock and tar is an unwanted by-product.

Bio-photolysis, dark fermentation and photo-fermentation are all biochemical processes with the first being CO_2 consuming and the other two CO_2 neutral. Bio-photolysis operates under mild conditions and it requires sunlight as opposed to dark fermentation. Both fermentation processes contribute to waste recycling. Drawbacks are the extremely low hydrogen yields and rates resulting in the necessity of larger reactor volumes. Combustion and liquefaction are even less preferable methods as they both result in low hydrogen yields. Moreover, combustion produces substantial quantities of pollutants like CO_2, SO_2 and NO_x causing global warming and acid rain. Liquefaction operates under difficult to reach process conditions, e.g. temperatures in the range of -250 to -275°C, pressures between 50 - 200 bar and in the absence of oxygen (Ni et al., 2006).

Electrolysis, thermolysis and photolysis are all water-splitting technologies and thus only require water as a feedstock with oxygen as the sole by-product. Electrolysis needs electricity which can be generated by both fossil fuels or renewables. When the latter is used, the process will be pollutant-free. In the special case of solid oxide electrolysis, also heat is needed as an energy source. Electrolysis is for a large part already commercialized and there is an existing infrastructure. Disadvantages are the relatively low overall efficiency compared to fossil-based technologies and the high capital costs. Thermolysis also offers a clean and sustainable method for hydrogen production. However, High temperatures are needed resulting in corrosive problems and high investment costs. Lastly, photolysis, which is also an emission-free hydrogen producer. This process needs sunlight and it suffers from a lack of effective photo-catalytic material, making this method the least effective of the investigated technologies.

Table C.1: Summary of hydrogen production technologies.

Technology	Energy type	Energy source	Feedstock	Maturity	Efficiency [%]
Steam reforming	Thermal	Fossil fuels	Natural gas	Commercial	74-85
Partial oxidation	Thermal	Fossil fuels	Natural gas	Commercial	60-75
Autothermal reforming	Thermal	Fossil fuels	Natural gas	Near term	60-75
Hydrocarbon pyrolysis	Thermal	Int. gen. steam	Natural gas		-
Bio-photolysis	Light	Solar	Microbes, CO_2, water		10
Dark fermentation	Biochemical	-	Microbes, Organic biomass	Long term	60-80
Photo fermentation	Light	Solar	Microbes, Organic biomass	Long term	0.1
Biomass pyrolysis	Thermal	Int. gen. steam	Woody biomass		35-50
Biomass gasification	Thermal	Int. gen. steam	Woody biomass	Commercial	-
Alkaline electrolysis	Electric	Renewables, Fossil fuels	Water	Commercial	40-60
PEM electrolysis	Electric	Renewables, Fossil fuels	Water	Commercial	40-60
Solid oxide electrolysis	Electric + Thermal	Renewables, Fossil fuels	Water	Mid term	40-60
Thermolysis	Thermal	Solar	Water	Long term	20-45
Photolysis	Light + Electric	Solar	Water	Long term	0.06

Appendix D

Property range for the model

Table D.1: Property ranges for REFPROP® .

Parameter		Value	Unit
Hydrogen	T_{range}	0 - 200	°C
	p_{range}	1 - 200	bar
	ρ_{range}	0.05 - 16	kg·m^3
	h_{range}	2.8 - 7	MJ·kg^3
	u_{range}	1.8 - 4.6	MJ·kg^3
Oxygen	T_{range}	0 - 200	°C
	p_{range}	1 - 200	bar
	ρ_{range}	1 - 310	kg·m^3
Water	T_{range}	1 - 99	°C
	p_{range}	1 - 30	bar
Air	T_{range}	1 - 99	°C
	p_{range}	1 - 30	bar

Appendix E

Matlab® Simulink input parameters

Tables E.1 - E.4 gives all the pre-determined input parameters for the Matlab® Simulink model. Many of the parameters are taken from literature and some are determined by this study. These values are kept constant for all cases.

Table E.1: Parameters for environment.

Parameter	Value	Unit	Reference
Wind sensor height	5.2	m	-
Wind turbine height	100	m	(Ayodele & Munda, 2019)
Site specific exponential shear factor	0.1	-	-

Table E.2: Parameters for the wind turbine, rectifier and APX market

Parameter	Value	Unit	Reference
Wind Turbine			
Turbine radius	54.9	m	(Ayodele & Munda, 2019)
Power coefficient, $C_{\text{tur,max}}$	0.45	-	(Abdullah et al., 2012)
Gearbox efficiency, η_{gb}	0.85		(Ayodele & Munda, 2019)
Generator efficiency, η_{gen}	0.95		(Ayodele & Munda, 2019)
Cut-in wind speed, v_{ci}	3	$\text{m}\cdot\text{s}^{-1}$	(Ayodele & Munda, 2019)
Rated wind speed, v_{rated}	11.5	$\text{m}\cdot\text{s}^{-1}$	(Ayodele & Munda, 2019)
Cut-out wind speed, v_{co}	25	$\text{m}\cdot\text{s}^{-1}$	(Ayodele & Munda, 2019)
Rectifier			
Efficiency	0.9	-	(Ayodele & Munda, 2019)
APX market			
Starting week of the year	0	weeks	-

Table E.3: Parameters for PEME.

Parameter	Value	Unit	Reference
Operating modes			
Pressure operation	1	-	-
Temperature operation	1	-	-
Membrane operation	1	-	-
PEM Stack			
Number of cells, N_c	60	-	(Espinosa-López et al., 2018)
Cells area, A_c	290	cm^2	(Espinosa-López et al., 2018)
Anode pressure	34	bar	(Espinosa-López et al., 2018)
Cathode pressure	35	bar	(Espinosa-López et al., 2018)
Operating stack temperature	60	°C	(Espinosa-López et al., 2018)
Initial stack temperature	20	°C	-
Maximum cell current density	1.85	$A \cdot cm^{-2}$	(Espinosa-López et al., 2018)
Minimum cell current density	0.65	$A \cdot cm^{-2}$	-
Water circulation pump			
Electrical pump efficiency	0.98	-	(Espinosa-López et al., 2018)
Mechanical pump efficiency	0.75	-	(Espinosa-López et al., 2018)
Pump head	20	m	(Espinosa-López et al., 2018)
Consumed fraction of circulation water flow	0.0035	-	(Espinosa-López et al., 2018)
HEX			
ΔT of HEX sink flow	20	K	-
Pinch temperature	10	K	-
Sink flow pressure	2	bar	-
Pump head	20	m	(Espinosa-López et al., 2018)
Mechanical HEX pump efficiency	0.75	-	(Espinosa-López et al., 2018)
Electrical HEX pump efficiency	0.98	-	(Espinosa-López et al., 2018)
Gas separators			
Anode gas separator volume	0.2	$m^3 \cdot stack^{-1}$	-
Cathode gas separator volume	0.2	$m^3 \cdot stack^{-1}$	-
Initial oxygen pressure	1	bar	-
Initial hydrogen pressure	1	bar	-
Condensate trap			
Condensate trap temperature	5	°C	-

Table E.4: Parameters for the hydrogen storage system.

Parameter	Value	Unit	Reference
Transmission pipeline 1			
Outlet pressure	90	bar	-
Initial pressure	90	bar	-
Injection pipeline			
Pressure difference over outlet nozzle	5	bar	-
Salt cavern			
Volume to surface ratio	3.6	-	-
Thermal conductivity of the cavern wall	6	$W \cdot (mK)^{-1}$	(Bérest, 2019)
Natural convection inside cavern	3	$W \cdot m^{-2}K^{-1}$	(Bérest, 2019)
Thickness of conductive cavern shell	1	m	(Bérest, 2019)
Minimum cavern pressure	60	bar	(Wolf, 2015)
Maximum cavern pressure	180	bar	(Wolf, 2015)
Average constant temperature at cavern depth	45	°C	(Bérest, 2019)
Initial temperature of stored gas	45	°C	-
Transmission pipeline 2			
Initial pressure	90	bar	-
Pressure control stations			
Isentropic compressor efficiency	0.7	-	-
ΔT of HEX sink flow	10	K	-
Cp of sink flow (water)	4180	$J \cdot kgK^{-1}$	-
Pinch temperature of HEX	5	K	-
Outlet temperature of PCS1	10	°C	-
Outlet temperature of PCS2	45	°C	-
Outlet temperature of PCS3	10	°C	-

Appendix F

Matlab®-script input parameters

Tables F.1-F.5 give the input parameters used for the Matlab®-script. This script must be run before the Matlab® Simulink model.

Table F.1: Values used for the PEME electro-chemical submodel.

Parameter	Value	Unit	Reference
δ_{mem}	0.0178	cm	(Espinosa-López et al., 2018)
α_{an}	0.7353	-	(Espinosa-López et al., 2018)
E_{exc}	52994	kJ·kmol^{-1}	(Espinosa-López et al., 2018)
$i_{0,\text{an,SATP}}$	1.08·10^{-8}	A·cm^{-2}	(Espinosa-López et al., 2018)
$\sigma_{\text{mem,SATP}}$	0.1031	S·cm^{-1}	(Espinosa-López et al., 2018)
E_{pro}	10536	kJ·kmol^{-1}	(Espinosa-López et al., 2018)

Table F.2: Values used for the PEME MEA submodel.

Parameter		Value	Unit	Reference
Model parameter	$\text{P}_{\text{mem,H}_2}$	3.5·10^{-19}	mol·(cm·Pa·s)$^{-1}$	(Sartory et al., 2017)
	$\text{P}_{\text{mem,H}_2}$	3.5·10^{-19}	mol·(cm·Pa·s)$^{-1}$	(Sartory et al., 2017)

Table F.3: Values used for the PEME thermal submodel.

Parameter		Value	Unit	Reference
Model parameters	$\text{C}_{p,\text{th}}$	162116	J·K^{-1}	(Espinosa-López et al., 2018)
	R_{th}	0.0668	K·W^{-1}	(Espinosa-López et al., 2018)

Table F.4: Values used for transmission and injection pipelines (Before salt cavern).

Parameter		TP1	IP	Unit	Reference
Geometry	L	50000	1000	m	-
	ϵ	$1.5e^{-6}$	$1.5e^{-6}$	m	(Helgaker, 2013)
Angle	θ	0	-90	$^\circ$	-
Operation	p_{out}	90	p_{cav}	bar	-
Initial	$m(0,n)$	0	0	$\text{kg}\cdot\text{s}^{-1}$	-
	$p(0,n)$	90	p_{cav}	bar	-

Table F.5: Values used for transmission and discharge pipelines (After salt cavern).

Parameter		TP2	DP	Unit	Reference
Geometry	L	50000	1000	m	-
	ϵ	$1.5e^{-6}$	$1.5e^{-6}$	m	(Helgaker, 2013)
Angle	θ	0	90	$^\circ$	-
Operation	p_{in}	90	p_{cav}	bar	-
Initial	$m(0,n)$	0	0	$\text{kg}\cdot\text{s}^{-1}$	-
	$p(0,n)$	90	p_{cav}	bar	-

Appendix G

Electrical system

This section describes the electrical system of a HRES.

G.1 Electrical system types

Energy systems can be either grid-connected or stand-alone systems. Whether a certain topology is used depends on the application and financial costs. Grid-connected systems are connected to the grid and are therefore not solely dependent on renewable energy sources. This ensures that the demand is constantly met either by the renewable energy source or by electricity from the grid, making the system reliable even without a back-up system. There are two operational modes for grid-connected systems; grid-assisted and peak shavings mode. In grid assisted systems, the lack of generated electricity is provided by the grid resulting in a constant power supply to the electrolyzer leading to optimal operation of the system, lowering the hydrogen costs. Drawback, this constant power supply needs to be carefully regulated by a regulator unit which comes at high costs. This system type is suitable for hydrogen production. A peak shaving system can be used whereby the actual purpose of the HRES is to supply electricity to the grid or loads. In these systems the electrolyzers only operate when the generated energy is higher than the grid can absorb. This way, the excess energy is stored in hydrogen which can be converted into electricity at a later instant. However, like the stand-alone system, this system will also operate with variable power supply to the electrolyzer resulting in a lower capacity factor. Also, a regulator unit is needed raising the overall capital costs. The hydrogen cost of these systems is high due to a low capacity factor, but can be lowered when the produced hydrogen from excess power can be converted into electrical power when needed (Vivas, De las Heras, Segura, & Andújar, 2018).

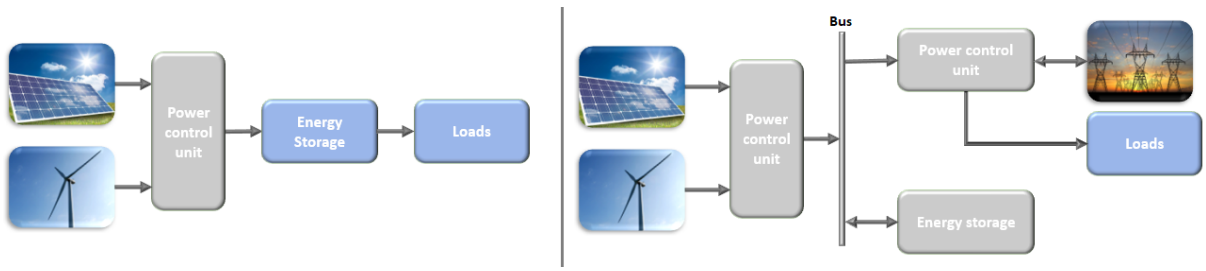

Figure G.1: Left: Stand-alone system. Right: Grid-connected system

Stand-alone systems, on the other hand, are responsible for meeting demand without grid-assistance.

Therefore, these systems are considered less reliable and are lacking performance. The lack of generated energy and storage results in unmet energy demand. Contrary, an excess of energy, meaning no energy demand and full storage, leads to energy losses.

G.2 Bus types

Often a bus must be used to interconnect the energy generation with the energy consumption. The three types are AC, DC and hybrid buses. DC buses are generally used for low power applications. Mainly due to the lower losses and simplicity. However, more conversion components are needed as most of the loads must be supplied with AC. AC buses are used in situations with medium to high energy production. Operating at high voltages is technically more simple with AC than using DC. However, often power quality elements are needed which greatly impact the overall system costs. The hybrid buses have an advantage of a reduced number of power converters, but the operational control is much more difficult (Vivas et al., 2018).

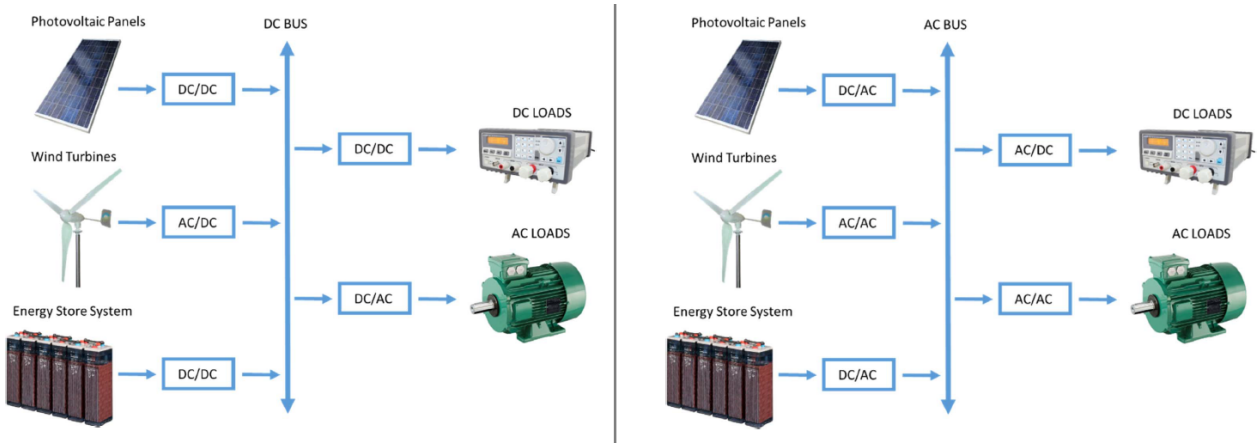

Figure G.2: Left: Renewable energy system (RES) with a DC bus. Right: RES with an AC bus (Vivas et al., 2018).

G.3 Electrical components

The type and voltage level of the bus and the size and type of the energy source and loads determine which additional components are needed for the power system. The electrical output of PV-panels are DC whereas for wind turbines it is AC. A voltage regulator is a device which is designed to maintain a constant voltage level. A DC/DC converter is a device that converts a direct current (DC) source from one voltage to another. In case of an increase in voltage, it is called a boost converter. When the voltage from input to output decreases, it is called a buck converter. Most of the time these converters can also regulate the voltage output. DC/AC converters, also called inverters, convert direct currents (DC) into a alternating currents (AC). AC/DC converter, also called a rectifier, does the opposite of an inverter. Lastly, a transformer is designed to increase or decrease the voltage input of a alternating current (AC) (Sangwine, 2018).

Appendix H

Alkaline electrolyzer system

The stack is the main component in the alkaline electrolyzer system. However, many other components are needed in order to achieve a functioning electrolyzer system. These components are described below and are depicted in Fig. H.1.

- **Power management unit**: This system often consists of a transformer and a rectifier to turn the high voltage AC to a specified DC voltage.
- **Gas separators**: The oxygen separator is installed to separate the water from the produced oxygen. The hydrogen separator separates the water from the hydrogen. A heat exchanger can be installed inside the separators to stimulate the separation process.
- **Demisters**: These devices, coalescent filters, separate the fine liquid KOH droplets from the gasses to maintain them in the electrolyte circulation.
- **Control valves**: Regulating the outlet pressures of oxygen and hydrogen.
- **Gas scrubber**: A gas scrubber is installed to wash out the remaining electrolyte solution from the hydrogen flow.
- **Filter**: A filter in placed between the separators and the lye tank to filter impurities from the electrolyte solution.
- **Electrolyte circulation pump**: An electrolyte pump can be installed to stimulate the convection inside the electrolyte tank.
- **Feed water pump**: A feed water pump supplies the gas scrubber with external water to maintain the concentration of the solution constant.
- **Water purification**: The water must be purified with filters and a ion exchanger to prevent fouling of the system.
- **Heat exchangers**: These exchangers can be added to control the electrolyte and gas temperatures.
- **Gas holder**: A gas holder at low pressure guarantees a constant hydrogen flow for downstream processes.
- **Lye tank**: The lye tank is used to make the electrolyte solution.

- **Two-stage hydrogen purification**: Deoxidizer reduces the oxygen content in the hydrogen stream with a catalytic reaction. A dryer is installed to dry the hydrogen to the required dew point by removing the water in absorption columns.

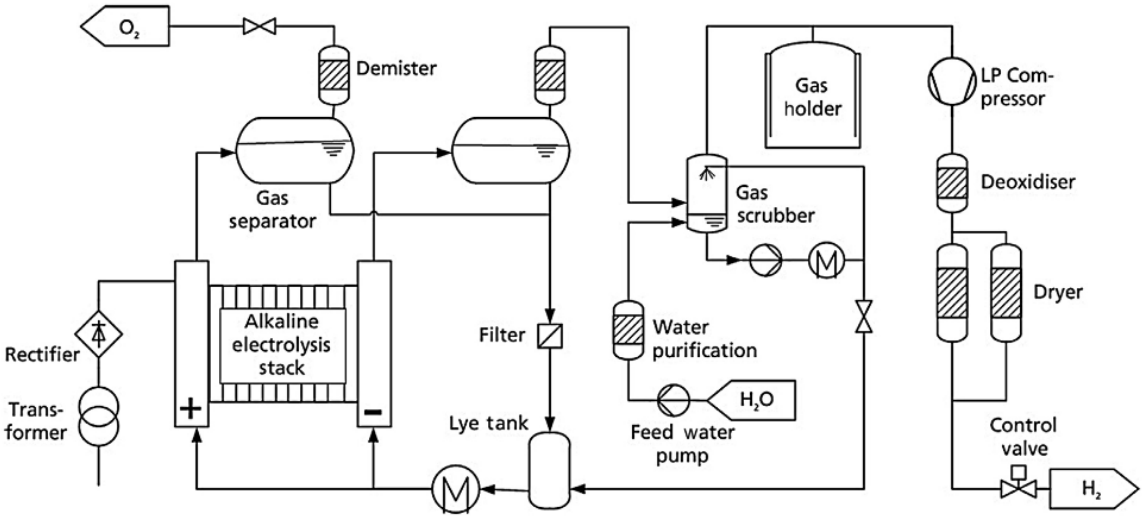

Figure H.1: Balance of plant of an alkaline water electrolyzer (Smolinka et al., 2015).

The alkaline electrolyzer is the most common and developed of all the electrolyzer types (Ursua et al., 2011; David et al., 2019). Moreover, the capital costs for this type are the lowest compared to the other types. It consists, besides the BoP, of a cell frame, an electrolyte, an anode, a cathode and a separating diaphragm.

The alkaline electrolyzer makes use of an aqueous electrolyte which comprises of water and 20-30 wt% of a strong base with sodium hydroxide (NaOH), potassium hydroxide (KOH) and sodium chloride (NaCl) being the most common. The main function of the electrolyte is conducting the ions between the electrodes (Tijani et al., 2014). Both the electrodes are immersed in the aqueous solution and are made of a catalytic material, where nickel (Ni), cobalt (Co) and Iron (Fe) are often used for the anode and a nickel alloy for the cathode (Sapountzi et al., 2017). Water is fed to the cathode where it is split into hydrogen (H_2) and hydroxide (OH^-) when interacting with the catalytic cathode. Subsequently, the electric field which is created by the potential difference (voltage) over the electrodes causes the hydroxide ions to move through the electrolyte and membrane towards the anode. Here, the hydroxide ions react with the catalyst to form oxygen and water vapour. The membrane acts as a gas separator with good ionic conductivity which prevents the hydrogen and oxygen from mixing, but allowing the ions to pass (Abdin et al., 2017).

$$\begin{aligned} 4OH^- &\rightarrow O_2 + 2H_2O + 4e^- \qquad \text{(Anode)} \\ 4H_2O + 4e^- &\rightarrow 2H_2 + 4OH^- \qquad \text{(Cathode)} \end{aligned} \tag{H.1}$$

These devices operate at an efficiency between 59 - 70%. The low capital cost, mature technology and stable operation are some of the main advantages. On the other hand, Gas permeation, slow dynamics and the corrosive electrolyte are unwanted side effects of these devices. Therefore, it is necessary to improve the durability and reliability as well as the anode reaction kinetics (Sapountzi et al., 2017).

Appendix I

Innovative hydrogen compressors

I.1 Mechanical compressors

Liquid compressors are positive displacement devices which make use of liquids to directly compress a gas without using mechanical sliding seals. Here, both the gas and liquid are compressed together. A quasi-isothermal process is possible as most of the dissipated heat is absorbed by the liquid and surrounding walls. Therefore, no additional heat exchanger is needed which greatly enhances the system efficiency. The liquid piston compressor (Fig. I.1) works identical to reciprocating compressors only with liquid instead of pistons. Here, a pump causes the movement of the liquid. As of now, these devices are predominantly used for compressed air energy storage at 200-300 bar (Sdanghi et al., 2019).

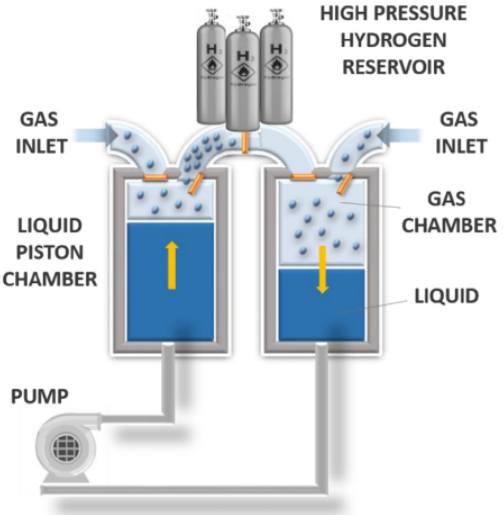

Figure I.1: Liquid compressor (Sdanghi et al., 2019).

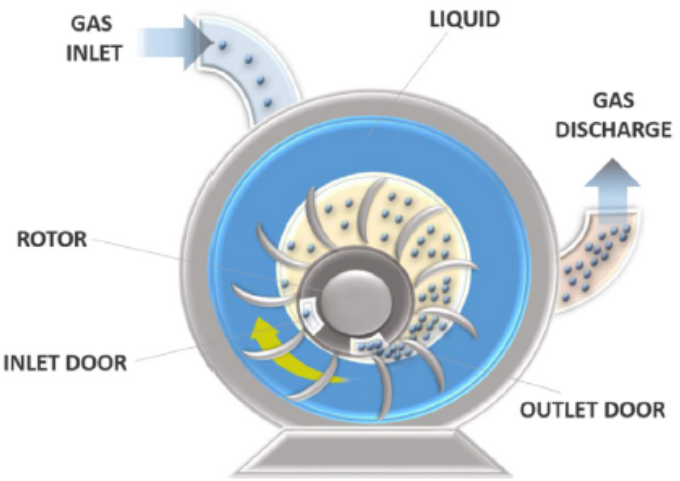

Figure I.2: Rotary liquid compressor (Sdanghi et al., 2019).

Liquid rotary compressors (Fig. I.2) are used to compress gasses with a high liquid content often in vacuum conditions. An impeller forces a liquid to form a ring which compresses the introduced gas. Ionic liquid compressors where developed to increase the efficiency of hydrogen compression. They make use of low-melting point salts. The properties of these salts offer low compressibility and

excellent lubricating abilities. Another great aspect, is the fact that these salts are almost insoluble to gasses especially to hydrogen. This results in high volumetric efficiency and compression ratios. Ionic liquid compressors are seen as a high performance device for improving the overall hydrogen system. Several advantages are, low energy consumption, durability, low capital costs and low noise production. However, they are prone to corrosion which may lead to contamination of the process gas and increase in maintenance costs. Furthermore, liquid discharge may occur making liquid traps necessary and liquid-gas mixing can lead to cavitation problems (Sdanghi et al., 2019).

I.2 Non-mechanical compressors

Non-mechanical compressors do not make use of positive displacement. These types are still in the research phase, so little is known about the efficiencies and applicability in large energy systems. However, they have the potential of becoming suitable compressor solutions for hydrogen. Therefore, a brief description will be presented in this section (Sdanghi et al., 2019).

Cryogenic compression (Fig. I.3) combines hydrogen liquefaction and compression. So, the hydrogen will be compressed in liquid phase resulting in high flow rates and discharge pressures. Liquid hydrogen is pumped via a vacuum insulated pipe to the desired pressure level by a cryogenic pump. Then, the liquid hydrogen is heated by a heat exchanger to ambient temperature where it is stored in a high pressure gas tank. The volumetric efficiency is twice as high as that of mechanical systems. However, a lot of energy is needed to reach the low temperatures and continuous monitoring of the system is necessary (Sdanghi et al., 2019).

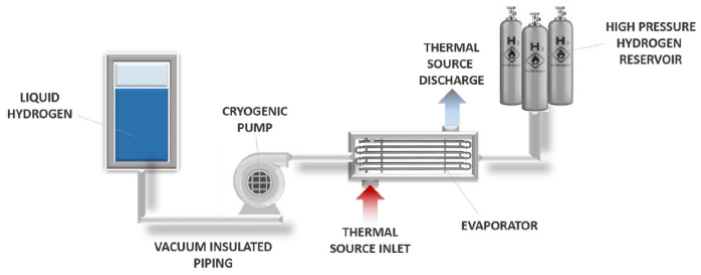

Figure I.3: Cryogenic liquid compressor (Sdanghi et al., 2019).

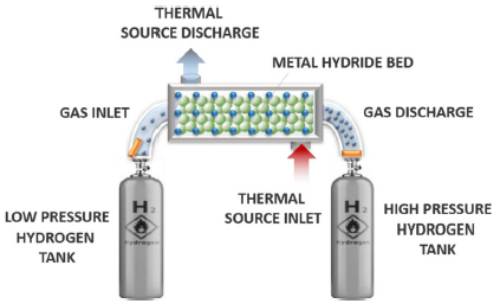

Figure I.4: Metal hydride compressor (Sdanghi et al., 2019).

Metal hydride compressors (Fig. I.4) function without moving parts and are thermally powered. These devices make use of absorption and desorption of hydrogen by a metal by means of heat and mass transfer mechanisms. Hydrogen absorption and desorption are exothermic and endothermic processes, respectively. Low pressure hydrogen is fed to a tank, filled with the metal hydride, where the exothermic absorption process initiates. This process continues until the equilibrium pressure is equal to the supply pressure. After equilibrium conditions, desorption can begin by heating the metal hydride which will increase the pressure inside the tank to discharge pressure levels. Heat transfer is accomplished by natural or forced convection with the wall surface of the tank, as this is commonly not thicker than 30 mm. High heat sources can result in discharges pressures of 3-10 times the supply pressure with volumetric efficiencies of 93%. The efficiency which is the compression work over the heat input does currently not exceed 10%. However, the main advantage of these systems is that

the compression process can be powered by industrial waste heat or solar energy (Sdanghi et al., 2019).

Electrochemical compression (Fig I.5) is based on the principles of a PEM electrolyzer. The process happens as long as the applied electrical energy exceed the internal energy. Very high compression efficiencies, no moving parts and low operation costs are some of the main advantages. Whereas, hydrogen back diffusion, high cell resistance and manufacturing of the cell assemblies pose disadvantages (Sdanghi et al., 2019).

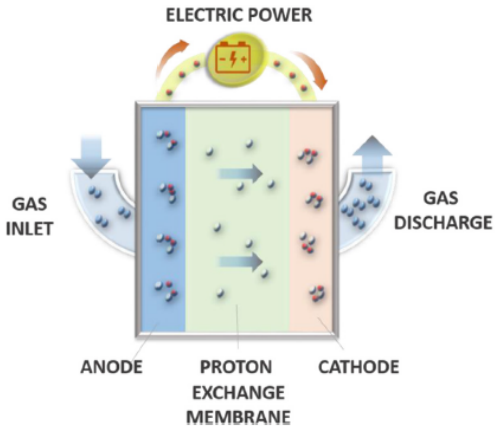

Figure I.5: Electrochemical compressor (Sdanghi et al., 2019).

Table I.1: Several reciprocating and non-mechanical compressors with operating data (Sdanghi et al., 2019).

Type [-]	Source [-]	Inlet pressure [bar]	Outlet pressure [bar]	Stages [-]	Flow rate [$Nm^3 \cdot h^{-1}$]	Applications [%]	Efficiency
Reciprocating	Leonard S. M.	4	25.5	x	no data	Hydrogen plants, catalytic reformers	no data
Reciprocating	Hydropac	350	859	x	4820	Filling vehicle tanks	no data
Reciprocating	Hitachi Infrastructure System	6	1000	x	300	Hydrogen stations	no data
Diaphragm	Hofer	5	151	x	5.5	no data	no data
Diaphragm	Hofer	18	281	x	581	no data	no data
Diaphragm	Hofer	26	180	x	450	no data	no data
Diaphragm	Weinert et al.	13	430	x	no data	no data	65
Diaphragm	Tzimas et al.	no data	1000	x	200-700	no data	80-85
Linear	Broerman et al.	20	860-950	3	>112	Research studies	>73
Ionic liquid	Van de Ven	no data	no data	-	no data	no data	83
Ionic liquid	The Linde Group	no data	450-900	-	90-340	Hydrogen refuelling station	>65
Ionic liquid	The Linde Group	5-200	1000	-	376-753	Hydrogen refuelling station	no data
Cryogenic	Linde	no data	350-900	-	>1000	Hydrogen refuelling sttion	no data
Metal hydride	Da Silva E.P.	10	100	-	0.42	Compression of high-purity hydrogen	4-7
Metal hydride	Lototskyy et al.	10	200	-	1	Industrial applications	1.65
Metal hydride	Yartys et al.	3	200	-	5	Industrial applications	no data
Electrochemical	Strobel et al.	1	43-54	-	1-6	Electrolyzers	80
Electrochemical	HyEt	1	700-1000	-	1	Energy storage	no data
Electrochemical	DON QUICHOTE project	no data	400	-	28	Energy storage with renewable energy	no data
Electrochemical	Lipp	1-140	830	-	0.06	no data	95

Appendix J

Lay-out of the Matlab® Simulink model

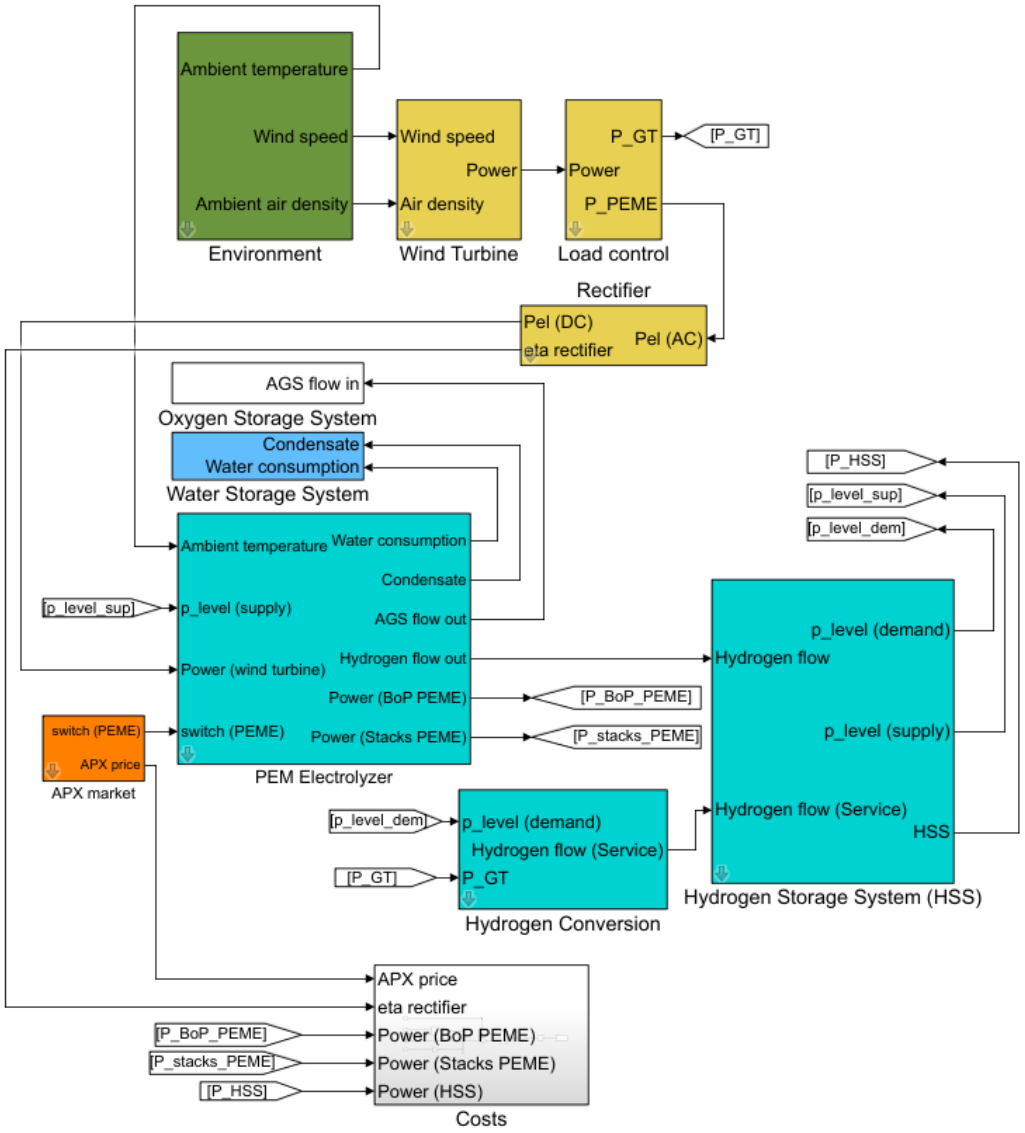

Figure J.1: Lay-out of the Matlab® Simulink model. The HSS contains the transport and storage systems.

Appendix K

Intermittent pipe flow simulations

A simulation is done to check the response of the pipeline model when the outlet flow suddenly goes to zero. A similar test case is performed in literature (Wang et al., 2015).

Figure K.1 shows the simulation results of the inlet mass flow when the outlet mass flow is instantly stopped. This simulation uses the values from Table 5.1. At the moment that the outlet valve instantly closes, the mass inside the pipe still has momentum towards to pipe end. As the gas can go nowhere, the outlet pressure rises due to compression of the gas at the pipe end. At this moment, there is no bulk flow which is driven by an external force, but a pressure wave propagating with the speed of sound along the pipeline. The period of the oscillations stay constant, but the amplitude decreases. This can also be seen in Fig. K.2, which plots the inlet and outlet pressures. When the friction factor only works in one direction, the amplitude of the oscillation is large and the mass flow oscillation takes much longer to dampen out and reach zero. For a friction factor with a varying sign, the amplitude of the mass flow is significantly smaller and reaches zero relatively quick, which is the desired result.

The period of the oscillation is determined by the speed of sound of the gas and the length of the pipe, as shown in Eq. (K.1). Here, t is the time of a single oscillation. It can be seen that changing the sign of the friction factor gives the better result, therefore, this will be used in the model.

$$\begin{aligned} t = \frac{4L}{c} \quad &\rightarrow \quad 4713 - 4206 = 507 \approx \frac{4 \cdot 48000}{380} = 505.26 \quad \text{(varying friction)} \\ t = \frac{4L}{c} \quad &\rightarrow \quad 4820 - 4187 = 633 \neq \frac{4 \cdot 48000}{380} = 505.26 \quad \text{(constant friction)} \end{aligned} \tag{K.1}$$

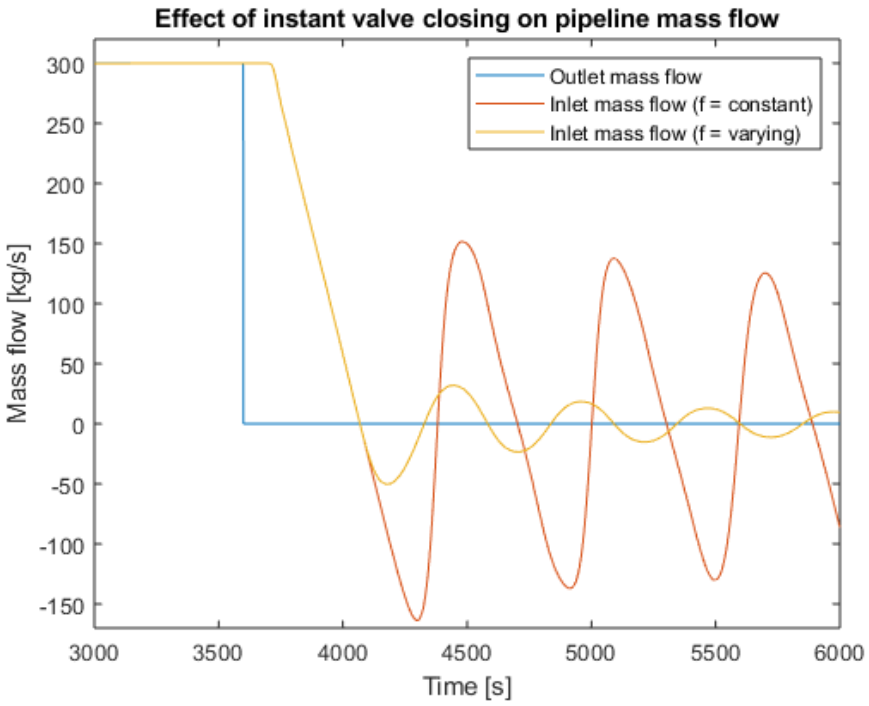

Figure K.1: Influence of the friction factor with varying and constant sign on the mass flow in a pipeline when the outlet valve instantly closes.

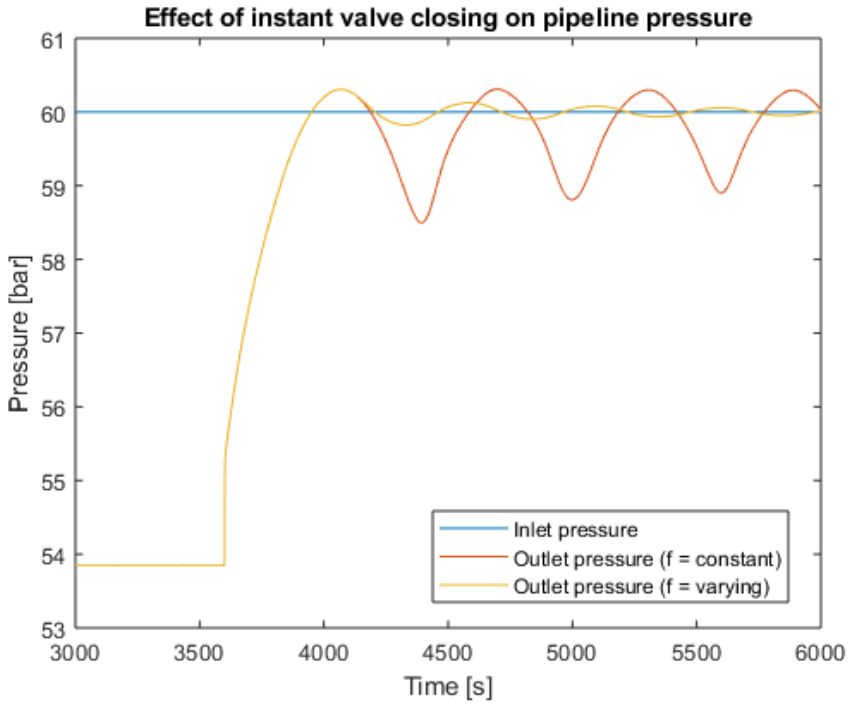

Figure K.2: Influence of a friction factor with a varying and a constant sign on the pressure wave when the outlet valve of a pipeline instantly closes.

Appendix L

PEME sensitivity

The PEME efficiency at rated power is calculated by running the PEME model with three different temperatures and a constant anode and cathode pressure of 35 bar. The results illustrate that higher temperatures result in higher efficiencies. A temperature increase of 24% going from 293.15 K to 363.15 K leads to and efficiency increase of 17%.

The pressure dependence is also analyzed. Five different pressure are used together with a constant temperature of 60°C. The results are plotted in Fig. L.1. The pressure influence on the efficiency is less significant as this only decreases with 3.4% when the pressure is increased with 7000% from 1 bar to 70 bar.

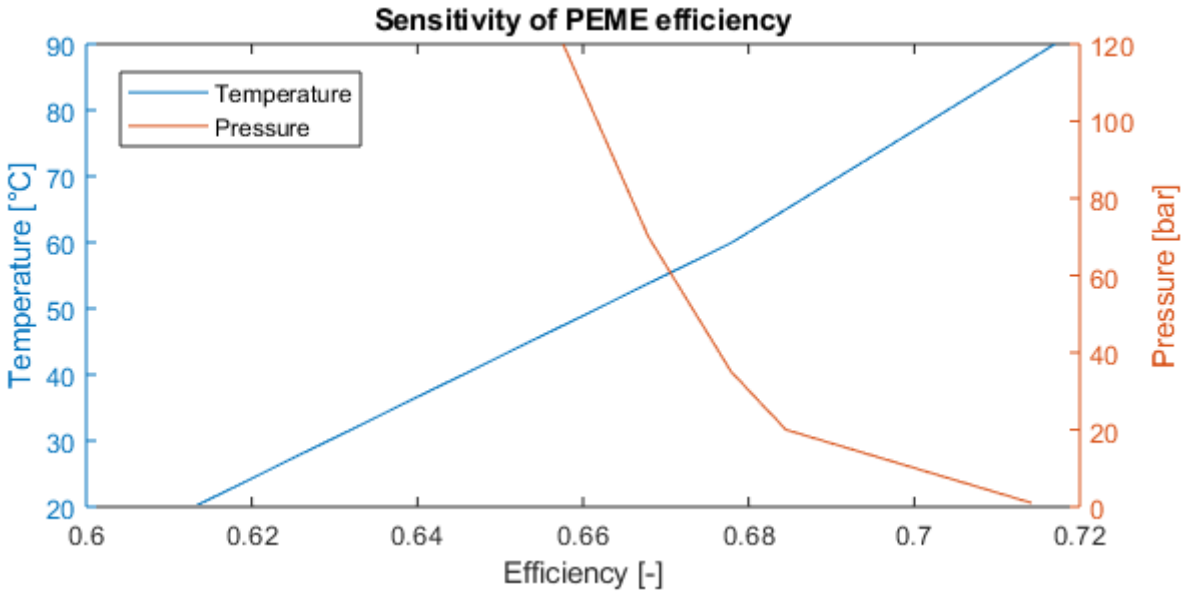

Figure L.1: Sensitivity of PEME efficiency to operating temperature and pressure.

Appendix M

Pipeline sensitivity

A sensitivity analysis was performed to determine the influence of the pipe length, diameter, outlet pressure and temperature on the pressure drop along a pipeline. The input parameters for the different runs are given in Tab. M.1. Run 2 gives the reference case.

Table M.1: Pipeline sensitivity analysis. The hydrogen mass flow was set to 0.16 kg·s^{-1}.

-	Length			Diameter					Pressure			Temperature		-
Parameter	Run 1	**Run 2**	Run 3	Run 4	Run 5	Run 6	Run 7	Run 8	Run 9	Run 10	Run 11	Run 12	Run 13	Unit
Length	25	**50**	100	50	50	50	50	50	50	50	50	50	50	km
Temperature	10	**10**	10	10	10	10	10	10	10	10	10	20	30	°C
Initial pressure	90	**90**	90	90	90	90	90	90	60	120	150	90	90	bar
Diameter	0.07	**0.07**	0.07	0.04	0.05	0.06	0.08	0.9	0.7	0.7	0.7	0.7	0.7	m

Figs. M.1 - M.4 plot the results of the various simulation runs. It was found that a longer pipe results in more pressure drop along the pipeline. A 100% increase in pipeline length from 50 km to 100 km, results in a pressure drop increase of 89.5%. Furthermore, the time it takes to reach steady-state flow increases with almost 50%.

Larger pipe diameters lead to less pressure drop along the pipe. This parameter has a more significant influence on the pressure drop. A 14.3% diameter decrease from 0.07 to 0.06 metre results in a pressure drop increase of 116.7%.

Higher initial pipe pressure which determines the outlet pressure results in less pressure drop. The pressure drop for a 60 bar pipeline is 15.8 bar, whereas for a 150 bar pipe, the pressure drop is 7.4 bar which is a decrease of more than 50%.

A higher isothermal flow temperature increases the pressure drop. An increase of 7.1% going from 283.15 K to 303.15 K, leads to a pressure drop increase of 7%. The pressure drop increases somewhat linearly with increasing temperature. The relative impact is significant, however, the temperature is controlled by the environment and can, therefore, not be adjusted.

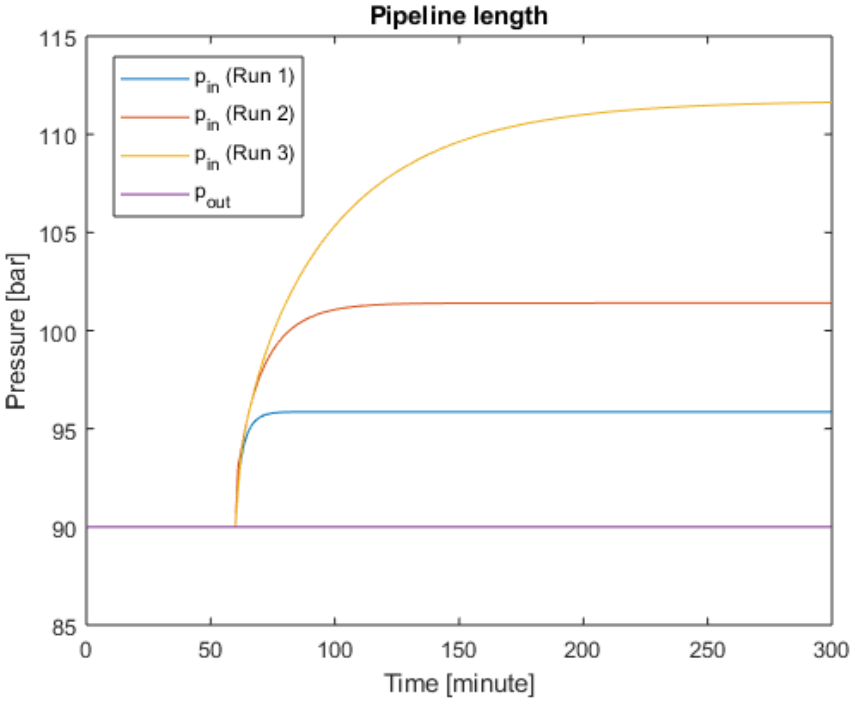

Figure M.1: Influence of the pipe length on inlet pressure.

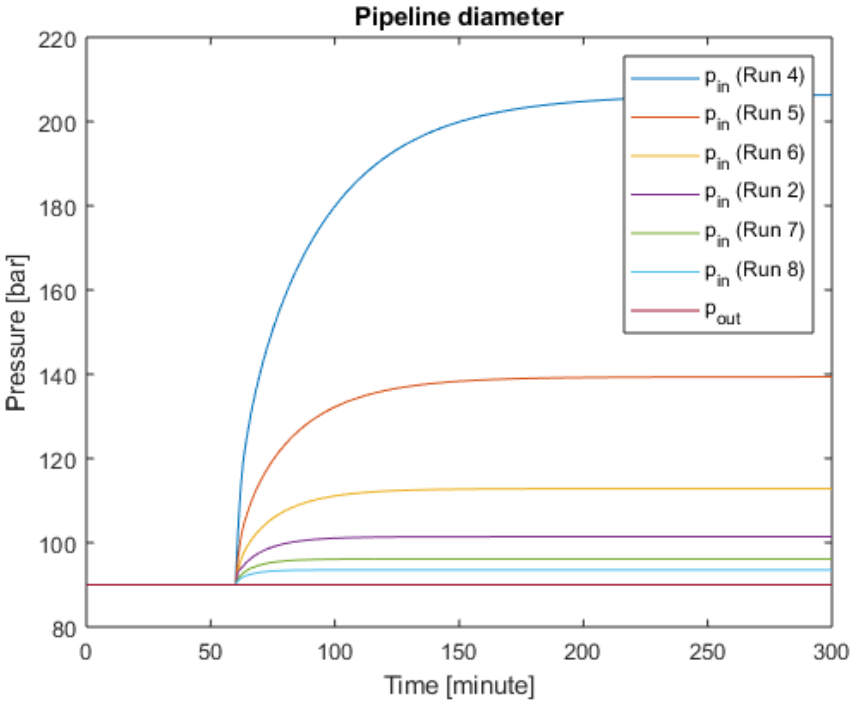

Figure M.2: Influence of the pipe diameter on inlet pressure.

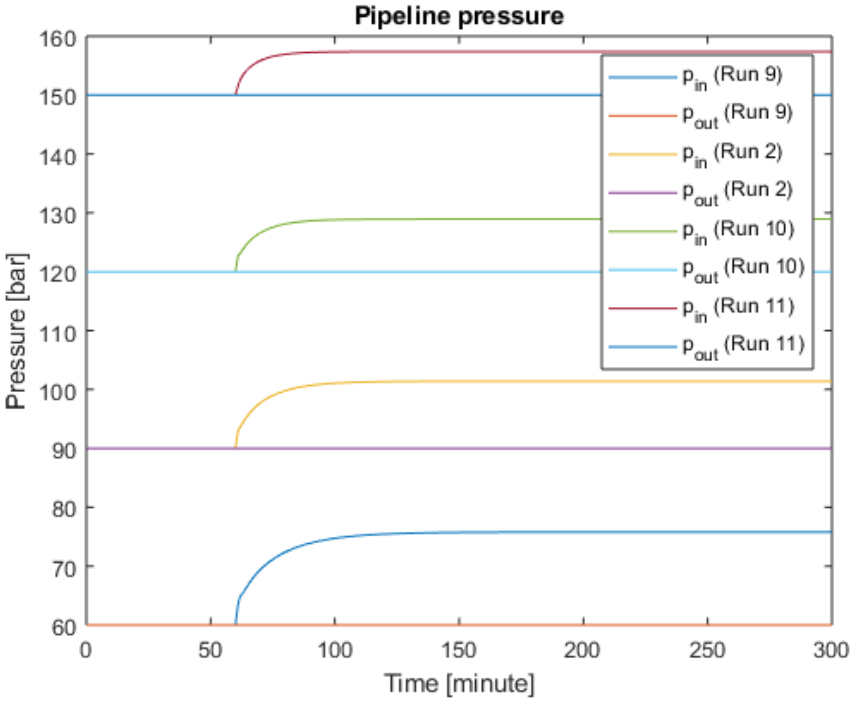

Figure M.3: Influence of the initial pressure on inlet pressure.

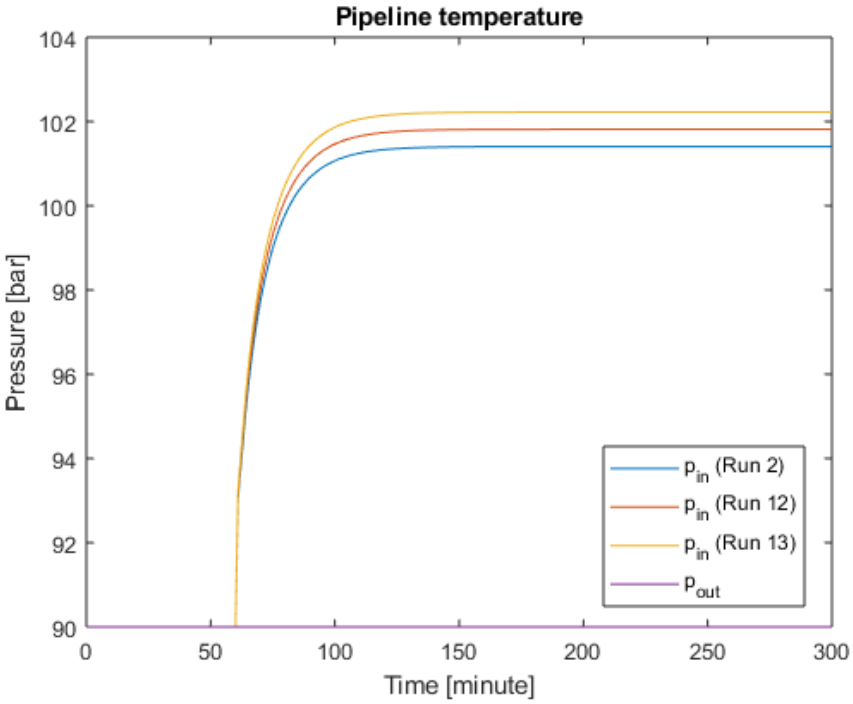

Figure M.4: Influence of the flow temperature on inlet pressure.

Appendix N

Flow property tables of cases

Table N.1: Operational results (Case GD-CHEM)

Component	CF	on-off	PR	p	T	mflow
[-]	[-]	[-]	[-]	min/max [bar]	min/max [°C]	min/max [kg·s^{-1}]
PEME	0.43	628	-	1.02/35.07	20/60	0/0.170
PC1	-	628	1/2.99	1.02/35	5/5	0/0.160
TP1	-	-	-	89.97/101.29	10/10	0/0.160
PC2	-	544	0.79/1.98	89.98/90.03	10/10	0/0.161
IP	-	-	-	70.93/177.89	45/45	0/0.161
SC	-	-	-	66.44/173.96	44.71/45.25	-
DP	-	-	-	66.44/173.96	44.71/45.25	-0.001/0.069
PC3	-	1	0.52/1.37	65.48/172.59	44.71/45.25	0/0.069
TP2	-	-	-	90/90	10/10	0/0.069
PC4	-	0	0.22/0.28	72.36/90	10/10	0/0.069

Table N.2: Operational results (Case WT-CHEM)

Component	CF	on-off	PR	p	T	mflow
[-]	[-]	[-]	[-]	min/max [bar]	min/max [°C]	min/max [kg·s^{-1}]
Wind farm	0.19	-	-	-	-	-
PEME	0.14	315	-	1.02/35.12	20/60	0/0.485
PC1	-	315	2.73/3.45	35/35	5/	0/0.485
TP1	-	-	-	89.96/120.78	10/10	0/0.485
PC2	-	250	0.74/2.00	89.97/90.04	/10	0/0.482
IP	-	-	-	66.97/179.84	45/45	0/0.482
SC	-	-	-	62/176	44.7/45.6	-
DP	-	-	-	62.45/175.81	44.72/45.56	-0.001/0.069
PC3	-	7	0.52/1.46	61.48/174.43	44.72/45.65	0/0.069
TP2	-	-	-	90/90	10/10	0/0.069
PC4	-	0	0.22/0.28	72.36/90	10/	0/0.069

Table N.3: Operational results (Case GD-PWR)

Component	CF	on-off	PR	p	T	mflow
[-]	[-]	[-]	[-]	min/max [bar]	min/max [°C]	min/max [kg·s^{-1}]
PEME	0.081	201	-	1.0/35.2	20/60	0/3.06
PC1	-	201	1/3.2	35/35	5/5	0/3.03
TP1	-	-	-	89.9/111.8	10/10	0/3.03
PC2	-	147	0.8/2.0	89.95/90.07	10/	0/3.01
IP	-	-	-	68.3/181.1	45/45	0/3.01
SC	-	-	-	63.8/177.1	44.3/45.6	-/-
DP	-	-	-	63.8/177.1	44.3/45.6	-0.02/5.30
PC3	-	1	0.5/1.4	62.7/175.9	44.3/45.6	0/5.30
TP2	-	-	-	89.85/90	10/10	0/5.30
PC4	-	0	0.2/0.3	65.3/90.02	10/10	0/5.30
GT	0.083	51	-	20/20	10/10	0/5.30

Table N.4: Operational results (Case WT-PWR)

Component	CF	on-off	PR	p	T	
[-]	[-]	[-]	[-]	min/max [bar]	min/max [°C]	min/max [kg·s^{-1}]
Wind farm	0.19	-	-	-	-	-
PEME	0.093	211	-	1.02/35.36	20/60	0/5.45
PC1	-	211	2.57/3.38	1.02/35	5/5	0/5.48
TP1	-	-	-	89.83/118.28	10/10	0/5.48
PC2	-	178	0.77/2.01	89.87/90.11	10/10	0/5.44
IP	-	-	-	69.23/180.76	45/45	0/5.44
SC	-	-	-	64.73/176.71	44.48/45.62	-/-
DP	-	-	-	64.73/176.71	44.48/45.62	-0.01/1.52
PC3	-	4	0.51/1.41	63.70/175.51	44.48/45.62	0/1.52
TP2	-	-	-	89.86/90	10/10	0/1.52
PC4	-	0	0.22/0.31	65.03/90.02	10/10	0/1.52
GT	0.192	433	-	20/20	10/10	0/1.52

Appendix O

Wind farm power limits

The operational range of the wind farm, used for Case WT-CHEM, leads to waste of wind power which is clearly depicted in Fig. O.1. after 307 hours the wind farm reaches its rated generator power output. Although the wind speed keeps picking up, the power output stays the same. After 330 hours, the power output drops to zero, although the wind speed is still over 2.5 $m \cdot s^{-1}$.

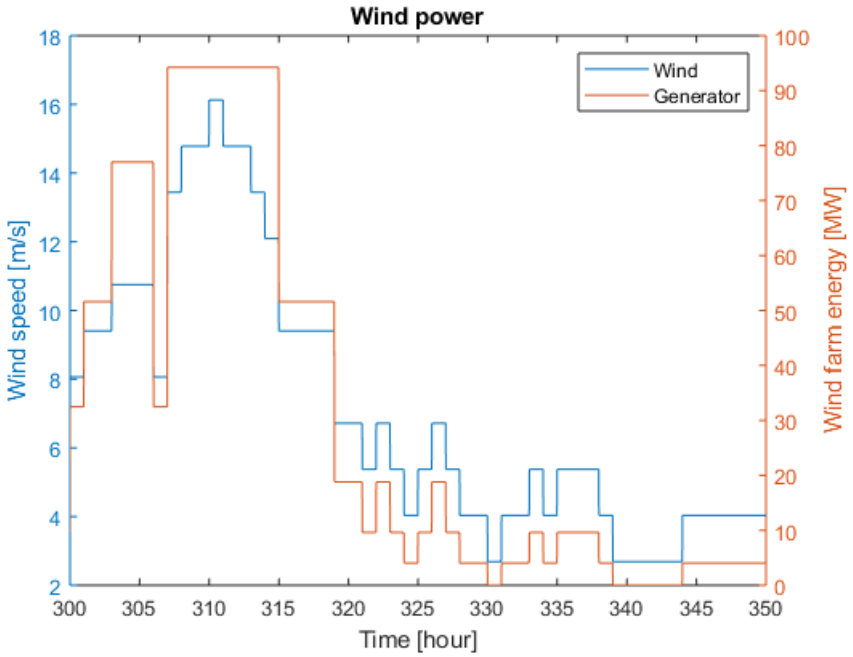

Figure O.1: Wind speed fluctuation and generator power output of the simulation run between 300 and 350 hours. (Case WT-CHEM)

Appendix P

Turbo-expander

A turbo-expander, in contrast to a throttling valve, will remove energy from the gas flow thus reducing its temperature. The cavern enthalpy and entropy are calculated using REFPROP® with the cavern pressure and temperature as inputs. REFPROP® is also used for isentalpic outlet enthalpy using the cavern entropy and outlet pressure. The power recovery is calculated using Eq. (P.1) (Ripepi, 2018). The outlet temperature is important as this may not drop below the pipeline operating temperature.

$$\begin{aligned} h_{\text{cav}} &= f(p_{\text{cav}}, T_{\text{cav}}), & h_{\text{out}} &= h_{\text{cav}} - \eta_{\text{exp,is}}(h_{\text{cav}} - h_{\text{out,is}}) \\ s_{\text{cav}} &= f(p_{\text{cav}}, T_{\text{cav}}), & P_{\text{exp}} &= \eta_{\text{exp,is}} \cdot \dot{m} \cdot (h_{\text{cav}} - h_{\text{out}}) \\ h_{\text{out,is}} &= f(s_{\text{cav}}, p_{\text{out}}), & T_{\text{out}} &= f(h_{\text{out}}, T_{\text{out}}) \end{aligned} \tag{P.1}$$

Figure P.1 indicates that the outlet temperature drops below the pipeline operating temperature when the cavern pressure surpasses 100 bar. At this point, around 0.5 MW of power can be recovered which is $\frac{0.6}{119.96} = 0.4\%$ of the chemical energy flow. At the maximum cavern pressure the flow temperature drops to -24°C which is well below the pipeline operating temperature. However, this temperature can be increased by using the waste heat flow from PCS 2 thus reducing the system losses.

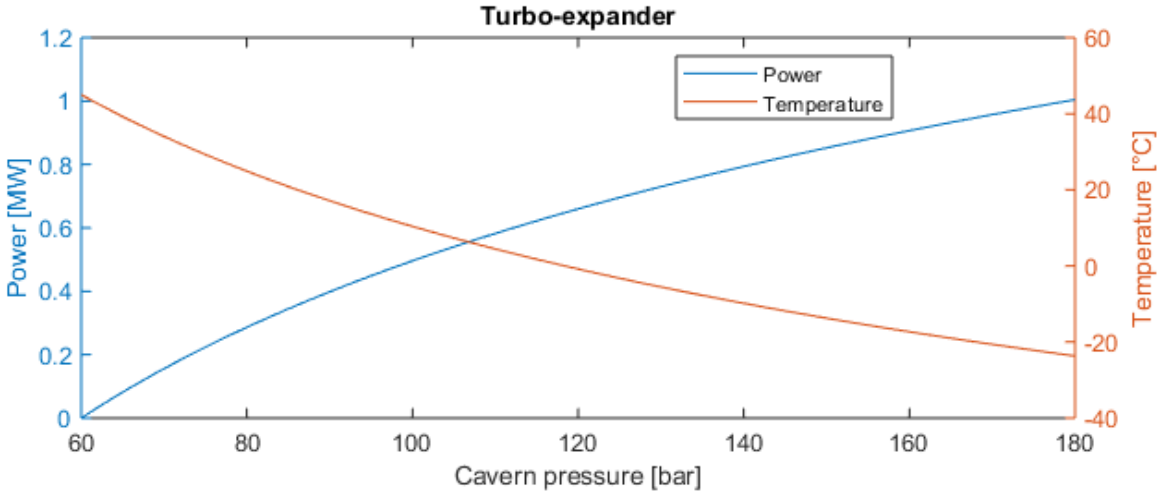

Figure P.1: Effect of cavern pressure on power recovery by a turbo-expander. The mass flow and expander outlet pressure are taken as 1 kg·s^{-1} and 60 bar, respectively. An electro-mechanical and isentropic efficiency of 0.95 and 0.8 are used, respectively (Ripepi, 2018).